

Scientific Report No. 53-2013

Added Value of Convection Permitting Climate Simulations

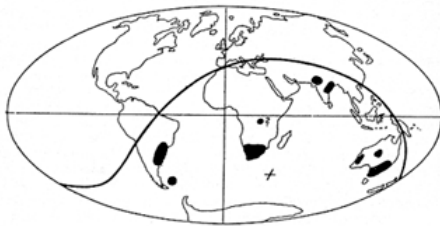
Andreas Prein

July 2013



The **Wegener Center for Climate and Global Change** combines as an interdisciplinary, internationally oriented research institute the competences of the University of Graz in the research area „Climate, Environmental and Global Change“. It brings together, in a dedicated building close to the University central campus, research teams and scientists from fields such as geo- and climate physics, meteorology, economics, geography, and regional sciences. At the same time close links exist and are further developed with many cooperation partners, both nationally and internationally. The research interests extend from monitoring, analysis, modeling and prediction of climate and environmental change via climate impact research to the analysis of the human dimensions of these changes, i.e., the role of humans in causing and being effected by climate and environmental change as well as in adaptation and mitigation. (more information at www.wegcenter.at)

The present report is the result of a Doctoral thesis work completed in July 2013.



Alfred Wegener (1880-1930), after whom the Wegener Center is named, was founding holder of the University of Graz Geophysics Chair (1924-1930). In his work in the fields of geophysics, meteorology, and climatology he was a brilliant scientist and scholar, thinking and acting in an interdisciplinary way, far ahead of his time with this style. The way of his ground-breaking research on continental drift is a shining role model—his sketch on the relationship of the continents based on traces of an ice age about 300 million years ago (left) as basis for the Wegener Center Logo is thus a continuous encouragement to explore equally innovative scientific ways:

paths emerge in that we walk them (Motto of the Wegener Center).

Wegener Center Verlag • Graz, Austria

© 2013 All Rights Reserved.

Selected use of individual figures, tables or parts of text is permitted for non-commercial purposes, provided this report is correctly and clearly cited as the source. Publisher contact for any interests beyond such use: wegcenter@uni-graz.at.

ISBN 978-3-9503608-0-6

July 2013

Contact: *Andreas F. Prein*
andreas.prein@uni-graz.at

Wegener Center for Climate and Global Change
University of Graz
Brandhofgasse 5
A-8010 Graz, Austria
www.wegcenter.at



Wegener Center for Climate and Global Change
Institute for Geophysics, Astrophysics,
and Meteorology/Institute of Physics
University of Graz

Dissertation
zur Erlangung des akademischen Grades eines Doktors der
Naturwissenschaften

Added Value of Convection Permitting Climate Simulations

ANDREAS PREIN

Graz, June 2013

Betreuer:
Univ.-Prof. Mag. Dr. Gottfried Kirchengast
Ass.-Prof. Mag. Dr. Andreas Gobiet

Wegener Center for Climate and Global Change, University of Graz, Brandhofgasse 5,
A-8010 Graz, Austria
Institute for Geophysics, Astrophysics, and Meteorology/Institute of Physics,
University of Graz, Universitätsplatz 5/II, A-8010 Graz, Austria

Abstract

CONVECTION permitting climate simulations (CPCSs) are able to omit error prone deep convection parameterizations by resolving deep convection explicitly. Furthermore, they are resolving orography and surface fields more accurately which is an advantage especially in mountainous or coastal regions compared to traditional climate simulation with parameterized deep convection. In this thesis it is investigated if these advantages lead to added value in CPCSs compared to coarser gridded simulations.

The main improvements of CPCSs are found in the representation of precipitation. Especially sub-daily scales and spatial patterns smaller than approximately 100 km are improved. At large (e.g., meso- α ; 200 km to 2000 km) scales, precipitation patterns of CPCSs tend to converge towards the patterns of coarser gridded simulations. However, two exceptions are found: (1) improved large-scale average heavy precipitation totals in June, July, and August in the Colorado Headwaters, and (2) more accurate spatial patterns of air temperature two meters above surface which is strongly related to the improved orography in mountainous regions.

The key added value which can be consistently found in an ensemble of CPCSs are: (1) improved timing of the summer convective precipitation diurnal cycle in mountainous regions, (2) more accurate intensities of most extreme precipitation, (3) more realistic size and shape of precipitation objects, and (4) better spatial distribution of precipitation patterns. These improvements are not caused by the higher resolved orography but by the explicit treatment of deep convection and the more realistic model dynamics. In contrast, improvements in summer temperature fields can be fully attributed to the higher resolved orography.

Generally, added value of CPCSs is predominantly found in summer, in complex terrain, on small spatial and temporal scales, and for high precipitation intensities.

Zusammenfassung

KONVEKTIONSAUFLÖSENDE Klimasimulationen (CPCSs) ermöglichen eine explizite Simulation der atmosphärischen Tiefenkonvektion wodurch fehleranfällige Parametrisierungen vermieden werden können. Desweiteren wird im Vergleich zu gewöhnlichen Klimasimulationen die Orographie und Landoberfläche detaillierter dargestellt was vor allem in Berg- und Küstenregionen vorteilhaft ist.

In dieser Arbeit wird der Mehrwert von CPCSs im Vergleich zu gröber aufgelösten Simulationen untersucht. Der größte Mehrwert findet sich in der Simulation des Niederschlages. Besonders Prozesse auf der Subtagesskala und räumliche Muster, die kleiner als ungefähr 100 km sind, werden verbessert. Auf größeren Skalen (z.B. der meso- α Skala) konvergieren Niederschlagsmuster von CPCSs mit jenen von grobskaligeren Simulationen. Allerdings werden zwei Ausnahmen gezeigt: (1) verbesserte sommerliche Starkniederschlagsmengen im Quellgebiet des Colorado Flusses und (2) realitätsnähere räumliche Muster der bodennahen Lufttemperatur, die stark mit der verbesserten Orographie zusammenhängen.

Ein Mehrwert, der konsistent in einem Ensemble von CPCSs auftritt, wurde in folgenden Bereichen gefunden: (1) verbesserte zeitliche Abläufe des Tagesgangs von konvektiven Niederschlägen im Sommer, (2) verbesserte Intensitäten von Extremniederschlägen, (3) realistischere Größen und Formen von Niederschlagsobjekten und (4) verbesserte räumliche Niederschlagsmuster. Diese Verbesserungen sind nicht durch die höher aufgelöste Orographie bedingt, sondern durch die explizite Auflösung der Tiefenkonvektion und der realistischeren Modelldynamik. Im Gegensatz dazu können Verbesserungen der bodennahen Temperatur im Sommer der höher aufgelösten Orographie zugeschrieben werden.

Zusammengefasst kann ein Mehrwert von CPCSs überwiegend im Sommer, im komplexen Gelände, auf kleinen räumlichen und zeitlichen Skalen und für hohe Niederschlagsintensitäten gefunden werden.

Acknowledgement

Gratitude is the memory of the heart.

(Jean-Baptiste Massieu)

PERSONALLY, this is the most important part of this thesis because this chapter tells about the human dimension, the passion, the love, the understanding, the compassion, and the help of people who wanted nothing in return which made this thesis possible. It is so important to me because you will not be able to read much about it in the upcoming chapters. However, this support is the elemental source of every word written here and cannot be appreciated enough.

At first place I want to express my gratitude to my supervisors Dr. Gottfried Kirchengast and Dr. Andreas Gobiet. First off all, because they gave me the opportunity to write my thesis in the Regional and Local Climate Modeling and Analysis Research Group (ReLoClim) at the Wegener Center (WEGC), University of Graz, which is one of the most encouraging working environments that I can imagine. Secondly, they supported me not only in a scientific way but also had an open ear and open heart for all kinds of concerns which arose during my journey leading to this thesis. Both of them are a great source of inspiration which taught me how passion and commitment can look like.

The WEGC is a great place to work and to study. But this is not because of the nice mansion in which it is located, the nice surrounding close to the University and city park, and also not because of the wide-screen LED monitor at my workplace. It is because of the people who are working there which have become much more than colleagues to me. During my five years at this institute I have got so much support, had so many inspiring discussions, and was able to learn so many things that I am afraid that I am not able give back only half as much as I have received. I especially want to thank the colleagues from my former office: Barbara Scherllin-Pirscher, Georg Heinrich, Matthias Themeßl, Renate Wilcke, and Andrea Damm with whom I shared all the ups and downs a Ph.D. study can provide. Furthermore, I am thankful to Martin Suklitsch who was a great support not only for learning to use the Wegener Center Integrated Climate Model Evaluation (WICE) toolkit but also for having so much patience with me asking

Acknowledgement

questions about dynamical downscaling in general and using the COSMO model in CLimate Mode (CCLM) in particular. Gratefulness belongs also to Heimo Truhetz for numerous inspiring discussions and to the much too oft forgotten administration staff. Their support is rarely visible but still essential for all who work at the WEGC.

Financial support was a key element which enabled me to study. Therefore, my thankfulness goes at the first place to my mother who is the most selfless person I have ever met. My gratefulness belongs also to the Austrian government which greatly supported me during my bachelor and master studies. Additional thanks should be given to the Austrian Science Fund (FWF) which funded the NHCM-1 and NHCM-2 projects and the European Union FP7 framework for funding the ACQWA project. Parts of this thesis were supported by the National Science Foundation (NSF) under the National Center for Atmospheric Research (NCAR) Water System Program, through the NSF EASM contract on Assessing High-Impact Weather Response to Climate Variability and Change Utilizing Extreme Value Theory, and by the Austrian Marshall Plan Foundation.

The studies presented relied heavily on computing resources. I am therefore grateful to the Jülich Supercomputing Centre (JSC), the German Climate Computing Center (DKRZ) in Hamburg, the European Centre for Medium-Range Weather Forecasts (ECMWF), and NCAR's Computational and Information Systems Laboratory (CISL), sponsored by the NSF for providing these resources.

As a member of the CCLM community I want to thank my colleagues therein for the open-hearted acceptance in their group, for providing guidance when help was needed, and the organization of great meetings. CCLM simulations are funded by the German Federal Ministry of Education and Research (BMBF).

During my studies I have got the great opportunity to visit Dr. Greg Hollands Regional Climate Group at NCAR in Boulder, Colorado, USA. Greg was a great host and supported me in every possible way. Also the members of his group, especially Dr. James Done, made my visit to one of the best experiences in my life. I am also thankful to Dr. Roy Rasmussen and his Colorado Headwaters group at NCAR who shared their valuable time, data, and knowledge with me.

Finally, my greatest gratitude belongs to my girlfriend Marina and my family. Marina was always there for me, in good times and in bad. She was the one with whom I celebrated my greatest successes and who helped me when I needed it the most. Furthermore I want to thank my mother for supporting me and believing in me ever since I can imagine. Another central person of my studenthood (and also of the rest of my life) is my twin brother Michael. We moved to Graz, started studying, and went through thick and thin together. Also my older brother Wolfgang was always there for me and was often the cause of pleasant distraction when I started pushing too hard.

To my father.

Preface

Parts of this Ph.D. thesis have already been published. The references are:

- Prein, A. F., A. Gobiet, M. Suklitsch, H. Truhetz, N. K. Awan, K. Keuler, and G. Georgievski (2013) *Added Value of Convection Permitting Seasonal Simulations*. *Clim. Dyn.*, DOI:10.1007/s00382-013-1744-6
- Prein, A. F., G. J. Holland, R. M. Rasmussen, J. Done, K. Ikeda, M. P. Clark, and C. H. Liu (2013) *Importance of Regional Climate Model Grid Spacing for the Simulation of Precipitation Extremes*. *J. Climate*, DOI:10.1175/JCLI-D-12-00727.1
- Prein, A. F. and A. Gobiet (2011) *Defining and Detecting Added Value in Cloud Resolving Climate Simulations*. Wegener Center Report Nr. 39, Wegener Center Verlag, Graz, Austria, <http://www.uni-graz.at/en/igam7www-wcv-scirep-no39-apreinagobiet-nhcm1-i-feb2011.pdf>

Contents

Abstract	i
Zusammenfassung	iii
Acknowledgement	v
Preface	vii
1 Introduction	13
2 Climate Change and Climate Modeling	17
2.1 A Changing Climate	17
2.1.1 Panta Rhei	17
2.1.2 The Human Factor	19
2.2 From Zero Dimensional Energy Balance to Earth System Modeling	23
2.2.1 The Physics of Atmospheric Flow	23
2.2.2 Computational Achievements	25
2.2.3 Weather and Climate Modeling	26
2.2.4 Increasing Diversity, Resolution, and Complexity	29
2.2.5 Parameterizations and Limited Knowledge	32
2.2.6 A Scale Problem	33
2.3 Regional Climate Modeling	35
2.3.1 Current Issues With RCMs	36
2.4 Skill of RCM Simulations	40
2.4.1 Downscaling Ability of RCMs	40
2.5 Convection Permitting Simulations	43
2.5.1 Important Components of Convection Permitting Models	46
2.5.2 Added Value in Convection Permitting Simulations	49
3 Dynamical Downscaling and Detecting Added Value	53
3.1 Dynamical Downscaling with RCMs on the Example of CCLM	53
3.1.1 Dynamics	53
3.1.2 Numerics	56

3.1.3	Physics	60
3.2	Searching and Detecting Added Value	72
3.2.1	Mean Climate	72
3.2.2	Spatiotemporal High Resolution	75
4	Added Value in Convection Permitting Simulations	90
4.1	Added Value of Convection Permitting Seasonal Simulations	90
4.1.1	Experimental Setup, Data, and Models	91
4.1.2	Results	96
4.1.3	Discussion	113
4.2	Importance of Grid-Spacing for Simulating Precipitation Extremes	121
4.2.1	Experimental Setup, Data, and Models	121
4.2.2	Results and Discussion	123
5	Summary and Conclusion	132
	List of Figures	136
	List of Tables	138
	Acronyms	139
	Bibliography	146

1

Introduction

Share your knowledge with others. It's a way to achieve immortality.

(Dalai Lama)

REGIONAL climate models (RCMs) (Dickenson et al. 1989; Giorgi and Bates 1989) are capable of providing additional regional details beyond the resolution of global climate simulations and re-analysis products. With RCMs only limited areas of the globe are simulated. The required information at the lateral boundaries is usually provided by either global models, reanalyses, or from larger scale regional models. Over the last decade RCMs have proven themselves as important tools in climate sciences (e.g., Wang et al. 2004; Rummukainen 2010) and climate change impact research (e.g., Finger et al. 2012; Heinrich and Gobiet 2011) and considerable efforts were made to further develop and improve RCMs by increasing their complexity and resolution. The horizontal grid spacing of state-of-the-art RCMs typically ranges from 50 km to approximately 25 km (e.g., 50 km in PRUDENCE (Christensen and Christensen 2007), 25 km in ENSEMBLES (Linden and Mitchell 2009), 50 km in NARCCAP (Mearns et al. 2009)). More recently, due to advancements in the field of computer sciences, it is now possible to have higher resolved climate simulations with approximately 10 km horizontal grid spacing (e.g., Loibl et al. 2011; Gobiet and Jacob 2012). Nevertheless, even with a mesh size of 10 km there are still numerous processes which cannot be resolved on the model grid and

therefore have to be parameterized. These parameterizations are important sources of model errors (Randall et al. 2007) and introduce large uncertainties in the projections of future climate (Déqué et al. 2007).

One challenging task for modelers is the parameterization of deep convection. Although much progress has been made in terms of improvement of old parameterization schemes as well as formulation of new ones, they are still the source of major errors and uncertainties. The most important benefit of convection permitting climate simulations (CPCSs) is that error-prone deep convection parameterization schemes can be omitted as deep convection can be (at least partly) resolved explicitly (Weisman et al. 1997). Furthermore, increasing resolution leads to a more realistic representation of the orography and land surface. However, CPCSs are far from being established because of their immense demand of computational resources and their still widely unknown quality.

In numerical weather prediction (NWP) convection resolving models are already widely used for operational forecasts and research purposes (e.g., Mass et al. 2002; Kain et al. 2006; Schwartz et al. 2009; Gebhardt et al. 2011). According to Weisman et al. (1997) the critical horizontal grid spacing for CPCSs is approximately 4 km. For grid spacings between 8 km and 12 km certain aspects of deep convection are still reasonably represented, but deep convection evolves too slowly and net heat transports, rainfall rates, and net strength of deep convection systems are overestimated. By using the fractions skill score (FSS) method Roberts and Lean (2008) showed that convection resolving forecasts are able to produce more realistic precipitation patterns due to a more accurate distribution of the rain and a better prediction of high accumulations. Weusthoff et al. (2010) investigated forecasts from three different NWP models over Switzerland with the FSS and the upscaling method from Zepeda-Arce et al. (2000) and found significantly improvements particularly for convective, more localized precipitation events. Langhans et al. (2012) found that in convection permitting simulations with different horizontal grid spacings (4.4 km, 2.2 km, 1.1 km, and 0.55 km) bulk flow properties, like heating or moisture tendencies (but also precipitation), converge towards the 0.55 km solution. They concluded that convection permitting grid-spacings seem to be sufficient for physical convergence of bulk properties in real case studies.

On longer time scales (14 months) Grell et al. (2000) found similar results and showed that spatial precipitation patterns are changing between CPCSs and coarser resolved simulations with parameterized convection in complex orography. Hohenegger et al. (2008) showed that in their CPCSs the precipitation maxima were better localized, a cold bias was reduced, and the timing of the summertime precipitation diurnal cycle was improved compared to a larger scale reference simulation.

Common limitations of the above mentioned studies are that they only investigate a single model, a relatively small domain, a small set of parameters (mostly precipitation and temperature), or analyze a relatively short simulation period.

In this thesis these shortcomings are addressed in different ways. First, in Chapter 3, dynamical downscaling is explained on the example of COSMO model in CLimate Mode (CCLM) and multiple statistical methods are introduced which enable to investigate the added value of CPCs from climate average to sub-daily fields and with respect to spatial and temporal properties. A special focus lies on scale dependent analyses and novel statistical methods which enable to evaluate spatiotemporal highly resolved precipitation fields.

The main part of this thesis is presented in Chapter 4 and consists of two studies. The first one, presented in Section 4.1, follows a holistic approach by investigating where added value of CPCs compared to coarser gridded simulations can be found in an ensemble of simulations performed with three non-hydrostatic RCMs. Five simulations with approximately 10 km and five CPCs with approximately 3 km horizontal grid-spacing are compared. Additionally to the simulated temperature and precipitation also relative humidity and global radiation fields are evaluated within two seasons (June, July, and August (JJA) 2007 and December, January, and February (DJF) 2007 to 2008) in the eastern part of the European Alps. Spatial variability, diurnal cycles, temporal correlations, and distributions with focus on extreme events are analyzed and specific methods (FSS and Structure-Amplitude-Location (SAL) method) are used for in-depth analysis of precipitation fields. The goal is to find added value of CPCs which are consistent in different RCMs. The text and figures of this study are based on a paper by Prein et al. (2013[a]).

The results show that added value of CPCs can especially be found for intense precipitation over complex orography in JJA where convective induced precipitation is predominant.

These results motivate to investigate the representation of heavy precipitation in RCMs in more detail. Heavy precipitation events have high impacts on society, economy, and ecology by causing floods, landslides, and avalanches. However, heavy precipitation is often not only a hazardous weather event but also an important part of the hydrological water balance of regions like the European Alps (Cebon et al. 1998) or the U.S. Rocky Mountains (e.g., Petersen et al. 1999; Serreze et al. 2001; Weaver et al. 2000).

One of the most important processes leading to heavy precipitation events is deep convection. As mentioned above especially processes related to deep convective have a high potential to be improved in CPCs while in traditional climate simulations deep convection parameterizations can introduce large errors in the simulation of precipitation (e.g., Molinari and Dudek 1992; Dai et al. 1999; Brockhaus et al. 2008).

In the second study (in Section 4.2) differences between simulated summer and winter heavy precipitation events of coarse-scale simulations and one CPC are analyzed in depth. Therefore, climate simulations with the Weather Research and Forecasting Model (WRF) with approximately 36 km, 12 km, and 4 km horizontal grid-spacing are evaluated

against measurements in the headwaters of the Colorado River for an eight year period. Scale separation methods are used to understand differences across horizontal scales and to evaluate the effects of upscaling fine-scale processes to coarser-scale features associated with precipitating systems.

Finally, Chapter 5 closes with summary and conclusions.

2

Climate Change and Climate Modeling

IN this chapter a brief introduction into the development of climate research is given. Therein, the difference between natural and anthropogenic climate change, the rise and evolution of weather and climate models, the need for and skill of regional climate models (RCMs), and finally the potentials and added value of convection permitting climate simulations (CPCSs) are discussed.

2.1 A Changing Climate

The knowledge that the earth's climate is changing can be drawn back to ancient times. Also the theory that mankind has an influence on these changes is rather old but was long disbelieved. Within this section the knowledge about climate change is summarized from ancient Greek philosophers to climate research today. Thereby, important stepping stones are mentioned and discussed. The intention is to give a briefer introduction into the knowledge on which modern climate science is built on. Readers who demand for a more detailed introduction are referred to textbooks like Weart (2003) or Edwards (2010).

2.1.1 *Panta Rhei*

Before the 18th century scientists did not suspect that prehistoric climate might have been different from the modern period. One of the first who had the idea that climate is

not stationary and can undergo dramatic changes was Jean-Pierre Perraudin (Bradley 1999). He developed a theory how glaciers might have transported giant boulders into alpine valleys which motivated Louis Agassiz to study that phenomenon in more detail. In 1837 he proposed a theory termed *Ice Age* which denotes times when large parts of Europe and North America were covered by glaciers (Evans 1887). After years of disbelief and resistance the ice age theory was widely accepted by the 1870s.

However, scientists still did not know why the earth's climate in the past was partly so different from the present conditions. James Croll was the first who was partly able to answer this question. He published calculations in which he investigated the effect of changes of the earth's orbit around the sun which last for ten thousands of years (Croll 1875). He wrote that small changes in the orbit can lead to slightly less sunlight on the northern hemisphere which leads to more snow accumulations which, as a result, reflect more sunlight. This is a positive feedback cooling down the earth's surface may lead into an ice age.

In 1920 Milutin Milankovitch, a Serbian engineer, built on the theory of James Croll and calculated tree cycles which are caused by the disturbance of the earth's orbit by the sun and the moon (Weart 2003). The individual cycles have a 21 000-year (precession), 41 000-year (axial tilt), and a 100 000-year period (eccentricity). However, each of these cycles is too short to explain the sequence four ice ages which was recognized at this time.

Later on, in the mid 1960s, Milankovitch's theory got supported based on analyses from Emiliani (1955) and investigations of coral reef and deep-sea sediments by Broecker et al. (1968). They found that in their records, instead of long ice ages, there were a large number of short ones fluctuating in a frequency suggested by Milankovitch. Actually, they have found the glacial-interglacial periods.

Another important puzzle stone, why past climate did fluctuate that much, was added by the German scientist Alfred Wegener who formulated the hypothesis of *continental drift* (Wegener 1929). His idea was that the earth's continents are drifting on magma like icebergs do on water. Thereby, the location of continents play an important role in the development of ice ages (e.g., Muller and MacDonald 2000) because they can reduce the transport of energy by warm water from the equator to the poles. This can be done in three different ways. First, a continent is located on top of a pole (like Antarctica today). Second, there is an ocean located at a pole which is nearly entirely surrounded by land masses (like in the Arctic Ocean today) or third, most of the equator is covered by land masses (like it was during the Cryogenian period).

However, there are also other important factors which influenced the past climate regimes like ocean current fluctuations, the uplift of large areas above the snow line, variations in the solar energy input, volcanism, and changes in the earth's atmosphere.

One additional factor is still missing which effects the earth's climate increasingly

strong throughout the past millennia: humans. We are responsible for increasing greenhouse gases in the atmosphere, emission of aerosols, land use changes, and the destruction of ecosystems. How mankind is affecting the climate system is discussed in the next Subsection 2.1.2.

2.1.2 The Human Factor

The ancient Greeks were among the first to document changing climate conditions and related them to human actions. For example, a pupil of Aristotle named Theophrastus noted that local freezing conditions did change after the draining of wetlands (Neumann 1985). This knowledge has been forgotten throughout the medieval times where the church tried to explain climate anomalies as response to human sin (Stehr et al. 1995).

An important step toward the understanding how humans are influencing earth's climate was made by Joseph Fourier in 1824. He discovered that the earth's atmosphere is warming up the planet (Weart 2003). He described that the visible light from the sun can transmit through the earth's atmosphere efficiently. It gets absorbed at the earth's surface and re-emitted as infrared radiation which is heavily absorbed by the atmosphere and therefore increases the temperature at the earth's surface. In his visionary publication Fourier (1827) wrote:

“The establishment and progress of human societies, the action of natural forces, cannot change, and in vast regions, the state of the surface, the distribution of water and the great movements of the air. Such effects are able to make to vary, in the course of many centuries, the average degree of heat; because the analytic expressions contain coefficients relating to the state of the surface and which greatly influence the temperature.”

Some thirty years later John Tyndall found out which gases are responsible for the absorption of infrared radiation in the earth's atmosphere. In Tyndall (1872) he wrote that water vapor, hydrocarbons like methane, and carbon dioxide (CO₂) strongly block the radiation.

Meanwhile, national weather agencies started to measure atmospheric parameters like precipitation, temperature, and pressure. By the end of the 19th century large efforts were made to collect those observations globally. Analyzing these datasets scientists did see many ups and downs in the time line but no continuous trend (e.g., Hann 1903). Observations like these led to the assumption that humans might influence local and regional climate but do not have influence on the climate of the planet (Weart 2003).

Studying measurements of angle dependent variations in the infrared radiation from the moon reaching the earth's surface (at low angles the infrared rays have a larger path length through the atmosphere and get stronger absorbed) the Swedish scientist Svante Arrhenius calculated the effect of changing CO₂ concentrations on the global sur-

face temperature of the earth. Halving the CO₂ concentrations, he concluded, would be sufficient to produce an ice age while doubling the concentration would lead to a temperature increase of 5 K to 6 K (Arrhenius 1896) (a nowadays often used value called climate sensitivity). This estimation is surprisingly accurate compared to today's best estimates for the climate sensitivity which is 3.2 K with a spread of 2.1 K to 4.4 K (Randall et al. 2007).

Some 30 years later in 1938 Guy Stewart Callendar reviewed Arrhenius theory and showed that temperature and CO₂ levels were rising in the atmosphere during the last 50 years (Callendar 1938). Furthermore, he argued that new spectroscopic measurements showed that CO₂ is absorbing infrared radiation in the atmosphere. However, the majority of scientists did not believe that humans can impact the climate globally (Fleming 2007).

Hans Suess performed a carbon-14 isotope analysis in 1955 which showed that CO₂ from fossil fuel combustion is accumulating in the atmosphere (Revelle and Suess 1957). This was supported by findings of Roger Revelle in 1955 who found out that the surface layer of the ocean has only limited ability to absorb CO₂ and Charles David Keeling who showed that CO₂ concentrations in the earth's atmosphere were rising constantly.

In the 50s and 60s digital computers enabled to simulate the earth's atmosphere for the very first time. Syukuro Manabe and Richard Wetherald used this new technology to make a detailed calculation of the earth's greenhouse effect and found out that a doubling of the CO₂ concentration leads to approximately 2 K warming (Manabe and Wetherald 1967). This rather low value is a result of missing feedback mechanisms (e.g., cloud feedbacks) which were unknown at this time. From thereon the number of climate models, their complexity, and their computational demands were constantly increasing. I will investigate the functionality and components of climate models in more detail in the upcoming sections.

Beside climate models also observations improved the understanding of human influence on earth's climate. Especially the reconstruction of near surface temperature and atmospheric CO₂ concentrations from ice core measurements like those of Dansgaard et al. (1982) gave valuable insights in climate history. As an example in Figure 2.1 shows Antarctic temperature and CO₂ concentration for the past 800 000-years. Striking is the temporal relationship between the temperature and the CO₂ concentration which indicates the high impact of this greenhouse gas on temperature. A second feature is the strong fluctuations in both parameters. Apparent to the eye is the dominant cycle of fluctuations which is approximately 100 000-years as postulated by Milankovitch (eccentricity cycle). In fact, a spectral analysis of this datasets reveals that all three Milankovitch cycles are included. One more notable information in Figure 2.1 is the concentration of CO₂ in 2012 (approximately 392 ppm). This value is clearly higher than the maximum in the last 800 000-years. These reconstructed data are extremely

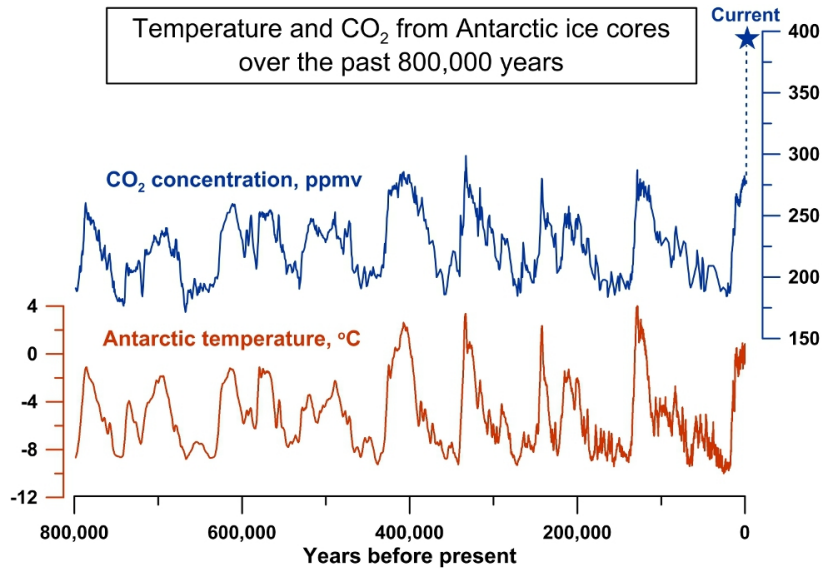


Fig. 2.1 Reconstructed CO₂ concentration and near surface temperature in Antarctica from Antarctic ice-cores over the past 800 000 years until 2012 (current) (Shakun 2013).

valuable to set the current atmospheric CO₂ concentrations and temperatures in context to past conditions. However, they are no prove that the global temperature increase during the past approximately 150 years is of anthropogenic origin.

Since in reality it is not possible to turn back time, remove all human traces from the earth, and let the climate system evolve under these new conditions to study the influence of mankind on climate warming, scientists used atmosphere-ocean general circulation models (AOGCMs) from the Coupled Model Intercomparison Project Phase 3 (CMIP3) to do exactly this experiment on the computer. The outcome is shown in Figure 2.2. In panel (a) the observed global temperature is compared to an ensemble of AOGCMs which are forced by natural and anthropogenic forcings. The ensemble mean temperature closely reproduces the observed temperatures including the cooling effects of large volcanic eruptions. In panel (b) the AOGCMs are only forced by natural forcings. The cooling effect from volcano eruptions is still present but the observed temperature increase cannot be reproduced by any of the simulations. This gives strong evidence that the recent increase in global temperature has an anthropogenic origin.

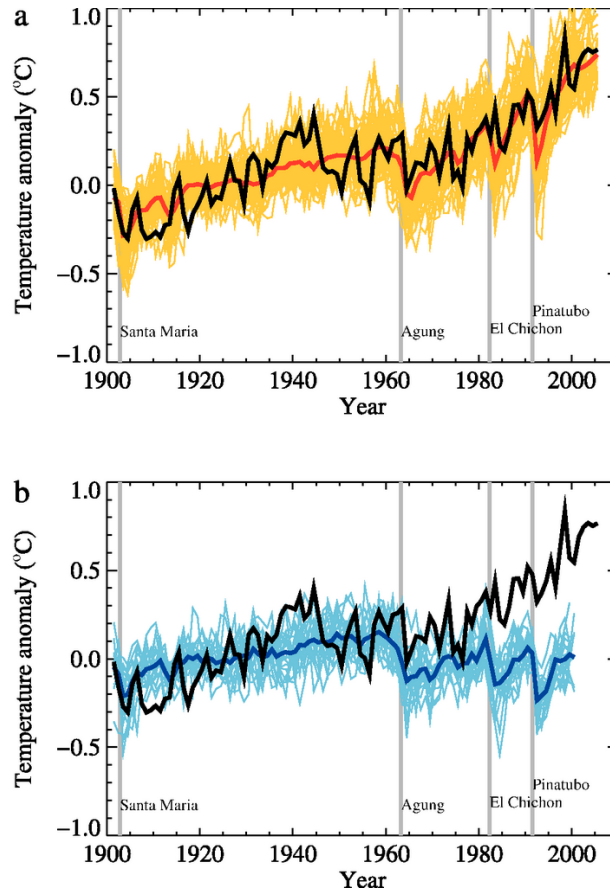


Fig. 2.2 Global mean temperature anomalies (relative to the period 1901 to 1950) for observations (black) and AOGCMs simulations. Panel (a) shows simulations forced with anthropogenic and natural forcings while panel (b) displays simulations with natural forcings only. Individual simulations are shown as thin lines and the model mean as thick red line in panel (a) and thick blue line in panel (b). Major volcanic eruptions are shown as gray vertical lines (Randall et al. 2007).

2.2 From Zero Dimensional Energy Balance to Earth System Modeling

In Section 2.1 we already got insights in the importance of physical based models for climate research. The modeling of the climate system has a long tradition. One of the first who used a so-called energy balance model to estimate climate sensitivity was Arrhenius (1896). No matter if energy balance model or modern AOGCMs are considered, all models follow the same three basic principals:

1. Models are *simplifications* of reality.
2. In models processes are *idealized*. They emphasize processes considered as important and neglect the others.
3. Models are subjects of *subjective* design. The application of the model determines which processes are important and which are negligible. A universal model for all ranges of applications does not exist.

Even though, these principals are still valid this does not mean that there has not been large progress in climate modeling since the end of the 19th century. One important step was done soon after 1900 by Vilhelm Bjerknes, a Norwegian scientist, who showed that the dynamics of large-scale flows can be described by a set of equations which are nowadays known as *primitive equations* (Bjerknes 1904).

2.2.1 The Physics of Atmospheric Flow

In his publication, Bjerknes (1904) combined thermodynamics and hydrodynamics to describe the interaction of energy, mass, momentum, and moisture of every single parcel of air with its surrounding parcels. This groundbreaking work was the first step towards numerical weather prediction (NWP) and still serves as the basis for most climate and NWP models. The primitive equations include the Newton's law of motion, the hydrodynamic state equation, the thermodynamic energy equation, and the mass conservation.

Starting with the Newton's second law of motion or momentum equation for a spherical earth, Equations 2.1 to 2.3 describe that the change of the momentum of a body is proportional to the resulting force acting on the body, and that it acts in the same direction of the force. The thermodynamic energy equation describes changes of temperature (T) in time (t) caused by adiabatic and diabatic effects (Equation 2.4). Equation 2.5 shows the continuity equation for mass and describes that mass is whether gained nor lost. Equation 2.6 is similar and describes the mass continuity of specific humidity (q_v). The last of the primitive equations is the equation of state or ideal gas law (Equation 2.7) which relates pressure (P), T , and density (ρ).

In Equations 2.1 to 2.7, u , v , and w are the Cartesian velocity components in the x , y , and z direction. Furthermore, rotational frequency of the earth (ω), latitude (ϕ), radius of the earth (a), temperature lapse rate (γ), dry adiabatic lapse rate (γ_d), specific heat of air at constant pressure (c_p), acceleration of gravity (g), evaporation/condensation heat release/loss (H), gain or loss of water vapor through phase changes (Q_v), and friction (Fr) are used.

$$\begin{aligned} \frac{\partial u}{\partial t} = & -u \frac{\partial u}{\partial x} - v \frac{\partial u}{\partial y} - w \frac{\partial u}{\partial z} + \underbrace{\frac{uv \tan \phi}{a}}_{\text{centripetal force}} - \\ & \underbrace{\frac{uw}{a}}_{\text{pressure gradient force}} - \underbrace{\frac{1}{\rho} \frac{\partial p}{\partial x}}_{\text{pressure gradient force}} - \underbrace{2\Omega (w \cos \phi - v \sin \phi)}_{\text{Coriolis force}} + Fr_x \end{aligned} \quad (2.1)$$

$$\begin{aligned} \frac{\partial v}{\partial t} = & -u \frac{\partial v}{\partial x} - v \frac{\partial v}{\partial y} - w \frac{\partial v}{\partial z} + \underbrace{\frac{u^2 \tan \phi}{a}}_{\text{centripetal force}} - \\ & \underbrace{\frac{uw}{a}}_{\text{pressure gradient force}} - \underbrace{\frac{1}{\rho} \frac{\partial p}{\partial y}}_{\text{pressure gradient force}} - \underbrace{2\Omega u \sin \phi}_{\text{Coriolis force}} + Fr_y \end{aligned} \quad (2.2)$$

$$\begin{aligned} \frac{\partial w}{\partial t} = & -u \frac{\partial w}{\partial x} - v \frac{\partial w}{\partial y} - w \frac{\partial w}{\partial z} + \frac{u^2 + v^2}{a} - \\ & \underbrace{\frac{1}{\rho} \frac{\partial p}{\partial z}}_{\text{pressure gradient force}} + \underbrace{2\Omega u \cos \phi}_{\text{Coriolis force}} - \underbrace{g}_{\text{gravity}} + Fr_z \end{aligned} \quad (2.3)$$

$$\frac{\partial T}{\partial t} = -u \frac{\partial T}{\partial x} - v \frac{\partial T}{\partial y} + (\gamma - \gamma_d) w + \frac{1}{c_p} \frac{dH}{dt} \quad (2.4)$$

$$\frac{\partial \rho}{\partial t} = -u \frac{\partial \rho}{\partial x} - v \frac{\partial \rho}{\partial y} - w \frac{\partial \rho}{\partial z} - \rho \left(\frac{\partial u}{\partial x} + \frac{\partial v}{\partial y} + \frac{\partial w}{\partial z} \right) \quad (2.5)$$

$$\frac{\partial q_v}{\partial t} = -u \frac{\partial q_v}{\partial x} - v \frac{\partial q_v}{\partial y} - w \frac{\partial q_v}{\partial z} - Q_v \quad (2.6)$$

$$P = \rho RT \quad (2.7)$$

Still missing in Equations 2.1 to 2.7 are the treatment of cloud particles, and the different types of precipitation. Readers who are interested in a mathematical derivation and deeper insight in these equations are revert to Dutton (1976) or Holton (2004). In the primitive equations above there are still parameters (H , Fr , and Q_v) which have

to be formulated within the model. P is used as vertical coordinate which can be problematic because pressure levels can intersect mountains. In Section 3.1 a solution to this problem will be shown which is used in the COnsortium for Small scale MOdeling (COSMO) model in CLimate Mode (COSMO model in CLimate Mode (CCLM)) RCM.

2.2.2 Computational Achievements

The primitive equations (Equation 2.1 to Equation 2.7) paved the way for “weather by the numbers” (Harper 2008). However, they are non-linear, non-homogeneous, prognostic¹, coupled, partial differential equations which cannot be solved analytically. Solving these equations during Bjerknes lifetime was prohibitively difficult (Edwards 2010).

In 1922 the English mathematician Lewis Fry Richardson attempted to perform the first forecast with Bjerknes equations by developing new mathematical methods involving finite difference equations for the seven basic variables: P , ρ , T , q_v , u , v , and w (Richardson 1922). With the help of finite difference equations the calculus to solve the primitive equations is reduced to arithmetic by transforming operations on variables to operations on numbers. Methods like this are generally called *numerical approaches* and are only approximations to the real solution because the time step and sizes of air parcels are finite instead of infinitesimal like in the original differential equations.

For his forecast Richardson (1922) divided Europe into 22 boxes with a square length of approximately 200 km (2° latitude by 3° longitude). Vertically he had one layer at the surface and four more above up to approximately 12 km which results in 110 three-dimensional grid-cells. Since computers were not invented at this time he calculated six weeks to finish a six-hour forecast. This huge effort brought him to the idea of a forecast-factory (see Figure 2.3) where groups of people, sitting in a large hall, solve the primitive equations for different parts of the world. In the middle of the dome a director is conducting the people like in an orchestra to ensure, for example, a uniform speed of progress in all parts of the world (Richardson 1922). However, even with this huge effort this method would have only permitted a global weather forecast in real-time which was one of the reasons why it was never implemented. Beside that, Richardsons test forecast was a complete disaster because an error in his equations lead to a surface pressure approximately 150 times larger than the observed value. These were the two major reasons why nobody used Richardson’s method for the next 25 years. Nevertheless, Richardson was a visionary and his forecast factory is still an accurate conceptual description of the practical reality of parallel computing today.

¹A prognostic equation means that the equation is predictive (has a time derivative), in contrast to a diagnostic equation which relates the state variables at the same time (e.g., like the ideal gas equation in Equation 2.7) (Warner 2011).



Fig. 2.3 Illustration of Richardson's forecast-factory by Schuiten (2013).

2.2.3 Weather and Climate Modeling

The history of NWP is closely related to the history of digital computing. NWP was applied on computers from the very beginning driven by the military need for more accurate weather forecasts within World War II. One of the most important persons in this development was Johan von Neumann who was part of the development of the Electronic Numerical Integrator And Computer (ENIAC), the principal US wartime computer project. He suggested the first two applications of ENIAC, the simulation of a hydrogen bomb explosion and weather forecasting (Aspray 1990).

In the postwar years von Neumann could only spend limited time to support the further development of weather forecasting and the progress in this field slowed down. This changed when Jule Charney took over the lead of the US Meteorological Project. Charney immediately started to work on "a step by step investigation of a series of models approximating more and more the real state of the atmosphere." (Charney et al. 1950).

Since the ENIAC computer had slow speed and very limited memory the group around Charney had to simplify the calculation. For this reason they made a couple of assumptions. One of the most important was the *quasi-geostrophic* assumption². It is a good assumption for large-scale flow in the free atmosphere because the Coriolis and

²In the geostrophic assumption a balance between the pressure gradient force which acts on a parcel horizontally in the direction of the low pressure minimum and the Coriolis force which is generated by the earth's rotation and deflects a parcel of air to the right on the northern hemisphere and to the left on the southern hemisphere is assumed. This produces so called geostrophic winds which move parallel to the isobars (lines of constant pressure).

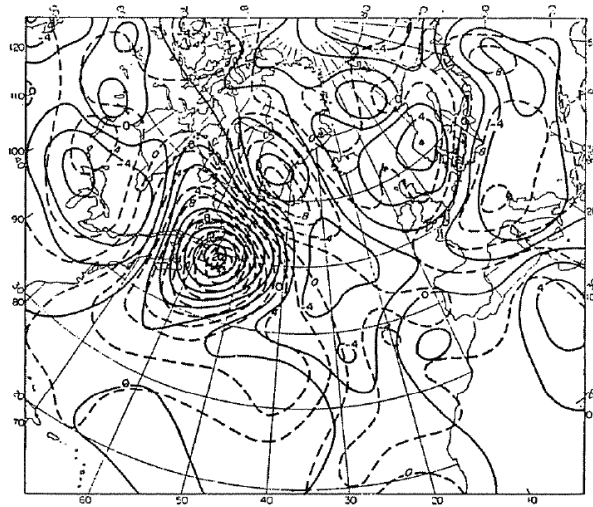


Fig. 2.4 ENIAC 24 hour forecast of height of the 500 hPa surface for January 31, 1941. Dashed lines display the computed forecast while solid lines show the observed values (Charney et al. 1950).

the pressure gradient force are the dominant terms in Equations 2.1 and 2.2 and have approximately the same order of magnitude.

With this assumption the equations of motion can be simplified to equations with P as the only depended variable.

$$u_g = -\frac{1}{\rho f} \frac{\partial P}{\partial y} \quad (2.8)$$

$$v_g = -\frac{1}{\rho f} \frac{\partial P}{\partial x} \quad (2.9)$$

The symbols in Equations 2.8 and 2.9 are: Coriolis parameter (f) ($f \approx 10^{-4} \text{ s}^{-1}$), u component of the geostrophic wind (u_g), and v component of the geostrophic wind (v_g). A positive side effect of this approximation is that high frequency atmospheric motions, like sound waves, are eliminated because motions like these can cause numerical instabilities in the model.

Charneys group in Aberdeen worked 33 days around the clock for two 12 hour and four 24 hour retrospective forecasts (Platzman 1979). In Figure 2.4 the forecasted and the observed heights of the 500 hPa surface for January 31, 1941 are compared. Even though there are some mismatches the computed result shows substantial similarities the observed outcome. Charney mailed copies of the forecast to Richardson in England and the success of this calculation encouraged the group for further research in this area

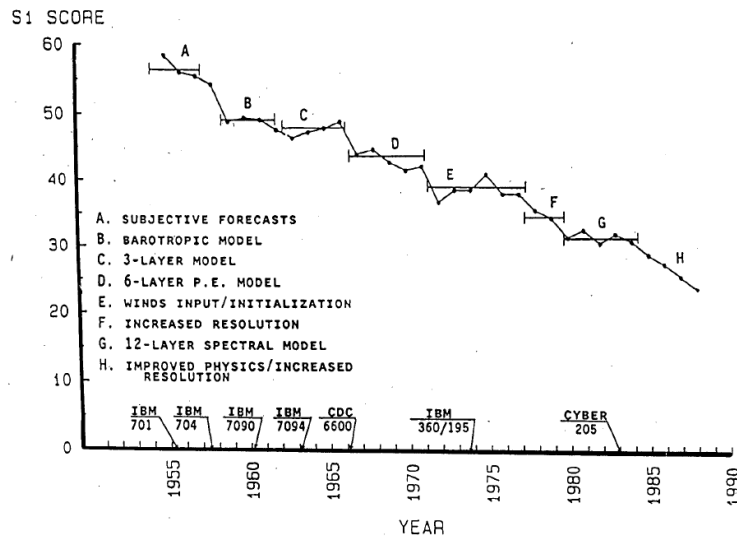


Fig. 2.5 S_1 skill scores for the 36 hour forecasts of 500 hPa geopotential height at the US National Meteorological Center from 1955 to 1988. 20 represents a perfect forecast in terms of the S_1 score while 70 represents a useless one (Shuman 1989).

and was an important argument for future funding (Wiin-Nielsen 1991).

Before people had the ability to use computationally supported NWP models, like those ran on ENIAC, there was nearly no improvement in the skill of weather forecasts since 40 years (Willet 1951). With the development of better and faster computers the weather prediction models got increasingly complex and the forecast quality did improve steadily as visible in Figure 2.5.

Charney's ultimate goal in climbing the hierarchy of models was a model which is able to simulate the global atmospheric motion (Edwards 2010). Later on such models were named general circulation models (GCMs) which represented the last step in von Neumann's research program. Using this models von Neumann's vision was the *infinite forecast*. With this term he did not mean to forecast weather conditions in the far future but to simulate atmospheric conditions on long time horizons which have become statistically independent from the initial conditions. And in fact that is the biggest difference between NWP and climate modeling.

The first person who performed a climate simulation with a GCM on a computer was Norman Phillips in 1956 (Phillips 1956). Thereby Phillips GCM was the cornerstone for all following GCMs as we will see in the upcoming Subsection 2.2.4.

2.2.4 Increasing Diversity, Resolution, and Complexity

Phillips groundbreaking simulation of the earth's general circulation caused a boom in GCM development from the 1960s onward. In Figure 2.6 the most important GCM modeling groups and their relationships are shown schematically. Some institutes copied the computer code from an existing GCM with only minor modifications, others adapted code to another computing system or just used parts of the code and rewrote the rest, while others started to develop their models independently.

Developing a GCM is a very costly and complex effort. This is the major reason why there is still only a quite limited number of groups doing this. In the currently running Coupled Model Intercomparison Project Phase 5 (CMIP5) 20 modeling groups majorly from North America, Europe, Japan, and Australia are involved. There are no contributions from Africa, Middle and South America, and the Middle East reflecting the immense costs of model development, human infrastructure, and supercomputing.

As already mentioned, the development of GCMs is closely related to the improvements in computations. From the very beginning, GCMs used the most advanced, fastest, and most expensive computers available. An empirical "law" named after the Intel co-founder Gordon E. Moore says that the number of transistors on integrated circuits doubles approximately every two years (Moore 1965). Moore's law is also valid for the increase of processing speed and memory capacity. Moore predicted that this trend will last for at least 10 years but until now, nearly 40 years later, it is still valid.

These computational developments were a major source for the improvements in climate modeling during the last half century. Thereby, the model development simultaneously went in two directions towards higher resolution and higher complexity.

In Figure 2.7 the minimum horizontal grid-spacing of GCMs during the four assessment reports of the Intergovernmental Panel on Climate Change (IPCC) is shown exemplary for the orography and surface fields of Europe. While in the first assessment report (FAR) in 1990 the highest resolved model had a grid-spacing of approximately 500 km, the highest resolution in the fourth assessment report (AR4) in 2007 was approximately 110 km. This results in a highly improved representation of orography, coastlines, and surface fields and furthermore allows the simulation of smaller processes in the atmosphere. For example, while Continental Europe consisted of approximately 40 grid-points in the 1990 GCMs, there were approximately 640 grid-points in 2007. It is important to note that the quadrupling of the horizontal resolution needs 64 times more computational steps for the same simulation because there are 16 times more grid-points and the time step has to be quartered at the same time to keep the simulation stable. In the newest GCM simulations performed for the IPCC fifth assessment report (AR5) and coordinated in the CMIP5 framework, the highest model resolution has again improved to approximately 60 km.

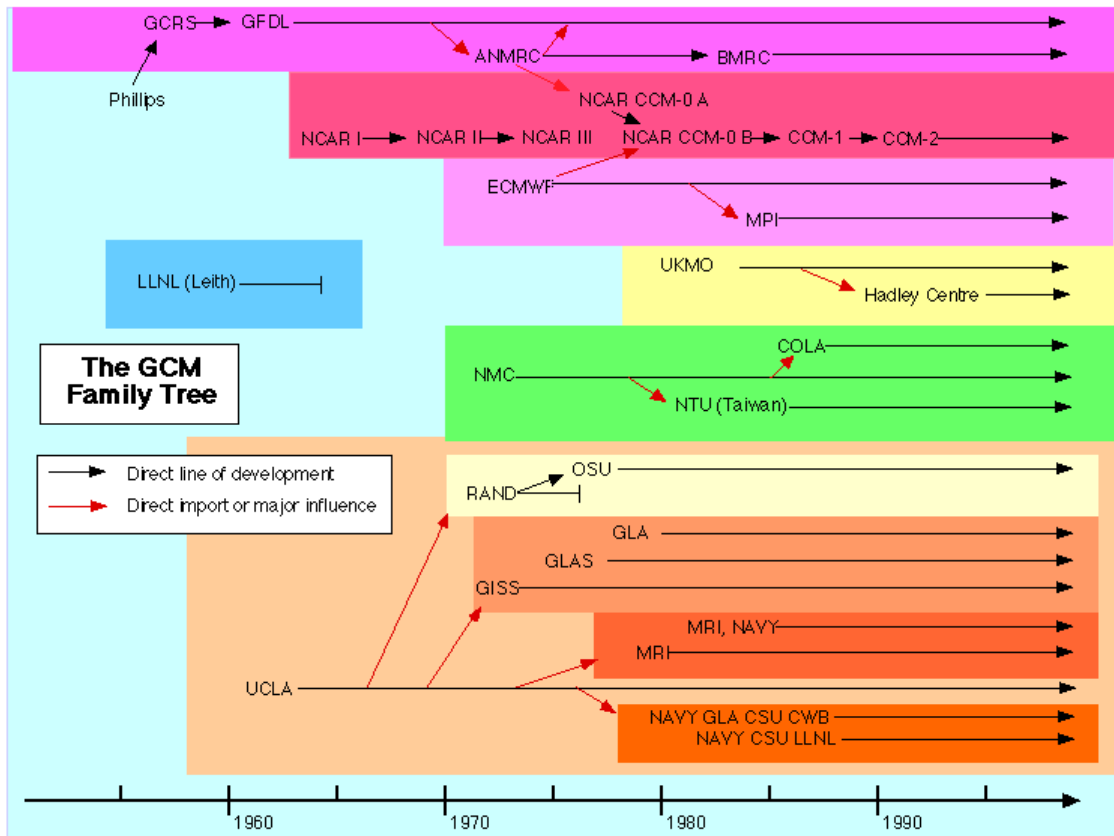


Fig. 2.6 The GCM family tree showing important relationships among the major modeling groups. The following abbreviations are used: BMRC: Bureau of Meteorology Research Centre (Australia), COLA: Center for Ocean-Land Atmosphere Studies (USA), ECMWF: European Centre for Medium-Range Weather Forecasts (UK), GFDL: Geophysical Fluid Dynamics Laboratory (USA), GISS: Goddard Institute for Space Studies (USA), GLA: Goddard Laboratory for Atmospheres (USA), LLNL: Lawrence Livermore National Laboratories (USA), MPI: Max Planck Institute (Germany), MRI: Meteorological Research Institute (Japan), NCAR: National Center for Atmospheric Research (USA), NMC: National Meteorological Center (USA), NTU: National Taiwan University (Taiwan), UKMO: United Kingdom Meteorological Office now the “Met Office” (UK), and UCLA: University of California Los Angeles (USA) (Edwards 2010).

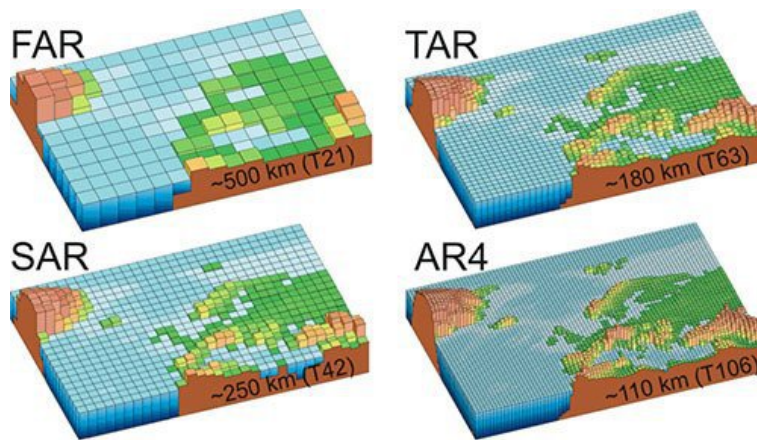


Fig. 2.7 GCM minimum horizontal grid-spacing during the first (FAR, 1990), second (SAR, 1995), third (TAR, 2001), and fourth (AR4, 2007) assessment reports of the IPCC. Source: IPCC 2007.

The second major GCM development, beside the higher resolution, was the increasing number of simulated processes as displayed in Figure 2.8. During the mid 1970s GCMs consisted purely of an atmospheric model and were able to simulate rain and the effects of greenhouse gas emissions. Ten years later land surface, clouds, and ice were introduced. Since the ocean is an important component in the climate system a swamp ocean was introduced in the GCM used in the FAR. In the second assessment report (SAR) volcanic activity, sulphates, and more realistic ocean models were included. Further improvements were the representation of the deep sea overturning circulations in the third assessment report (TAR) GCMs. GCMs which have a coupled atmosphere and ocean module are usually called AOGCMs. The GCMs used in the TAR also included rivers, the carbon cycle, and aerosol modules. Interactive vegetation and chemistry modules were added in GCMs used in the AR4. In parallel also older GCM modules were further developed and became more realistic. This trend of adding more and more modules to the GCMs lead to a new model generation which are called earth system models (ESMs). Their developers goal is to integrate all important processes which influence the future of earth's climate to provide answers on questions concerning societal dimensions. Thereby, GCMs are used as model components and are coupled to e.g., ice-sheet, river, or chemistry transport models. The great benefit of ESMs is that inter-module feedbacks like interactions between atmospheric chemistry and ocean acidification can be studied.

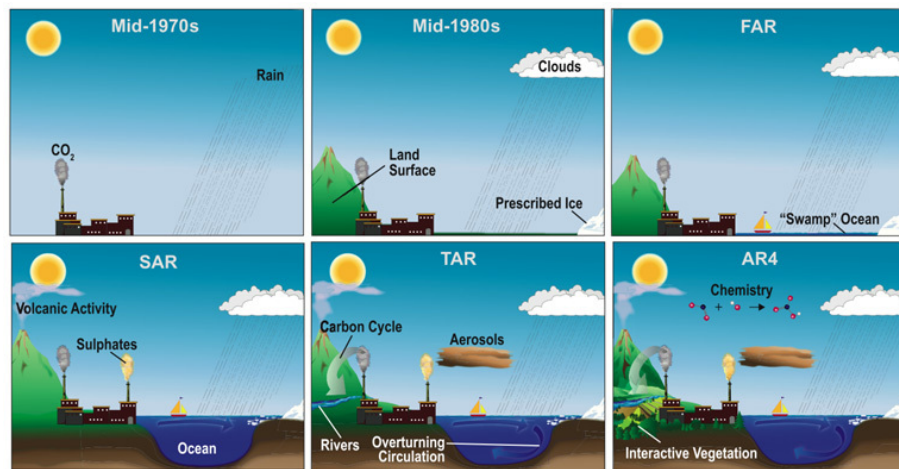


Fig. 2.8 Model components of GCMs during the last 40 years. Source: IPCC 2007.

2.2.5 Parameterizations and Limited Knowledge

Even though, modern GCMs are the most complete and complex models to simulate the earth's climate and contain numerous physical laws like energy and mass conservation, they are not fully physical but *physically based* models. Especially processes which are poorly understood, too complex, or too small to be directly modeled are often empirically approximated with parameters. According to the glossary of the American Meteorological Society a parameter is: "...any quantity of a problem that is not an independent variable. More specifically, the term is often used to distinguish, from dependent variables, quantities that may be more or less arbitrarily assigned values for purposes of the problem at hand.". This means a parameter stands for something that cannot be explicitly modeled but at least can be estimated or guessed (Edwards 2010).

In climate modeling most simulated processes need some degree of parameterization. The parameterized processes are usually called *model physics* (cf., Subsection 3.1.3). There is a huge number of parameters in every GCM whereby the simplest are just constants which are derived from observations. Examples for them are the solar constant, the size and location of landmasses, greenhouse gas concentrations, or the earth's gravitational force. However, parameterizations are mostly representing a physical process rather than a constant. Those parameterizations are for example used to simulate radiative transfer, precipitation, convection, turbulent fluxes, or cloud microphysics.

One strongly discussed topic is the tuning of parameters within climate models. In every GCM there are parameters which got re-adjusted and equations which were reformulated to more accurately resemble observations or to be physically more plausible. One constrain is that parameters should not be adjusted to values which are outside the

observed range. This means, some parameters are relatively fixed (the solar constant or earth's gravity are two examples) whereas other parameters allow a large range of possible values. Examples for them can be especially found in the cloud and aerosol parameterizations which are said to be “highly tunable” (Randall et al. 2007).

Less parameterizations and less tuning of the parameters therein (especially those contained in cloud and aerosol effects) are likely to be those model parts which have the highest potential to improve current climate model simulations in the near future (e.g., Kiehl 2007; Schwartz et al. 2007). A general problem is that often the same data are used to develop a parameterization, tune the model, and at the end evaluate the output of the model. This model-data symbiosis is a critical point and a further motivation to reduce the amount of parameterization schemes and tuning of parameters in climate models.

2.2.6 A Scale Problem

In Subsection 2.2.4 the trend towards higher horizontal resolution in GCM simulations was discussed. As we have seen, the highest horizontal grid-spacing within the CMIP5 dataset is approximately 60 km. This does not mean that there is meaningful information on the grid-point scale. In fact it can be shown that the real resolution or *effective resolution* of grid-box models is approximately 6 to 8 times larger than their grid-spacing (e.g., Grotch and MacCracken 1991; Skamarock 2004; Prein et al. 2013[b]). This means that we can assume that the highest resolved GCM in the CMIP5 dataset has an effective resolution of approximately 360 km.

Atmospheric processes and variations can be displayed in spectra of atmospheric space- and timescales like shown in Figure 2.9. With state of the art GCMs scales larger than several minutes (the model time step) and $\sim 10^5$ m can be resolved. This scale is called synoptic- or macro- β scale and includes e.g., cyclones and anticyclones, planetary waves, and oscillations like the El Niño–Southern Oscillation (ENSO) or Madden–Julian oscillation (MJO) (cf. Table 2.1). All processes which have smaller spatial scales than those resolved in the GCMs cannot be represented explicitly and therefore have to be neglected or parameterized (cf. Subsection 2.2.5).

Impacts of climate change on society can typically be found on the micro- and meso-scale. For example, water supply managements demand for reliable climate projections on the scale of single river catchments which are in most cases much smaller than the resolution of modern GCMs. Another example is the insurance industry which is interested in the future development of extreme weather events. However, extremes often have features which are smaller than the meso- α -scale and can be therefore not directly modeled with GCMs.

During the last centuries different methods have been developed to bridge the scale

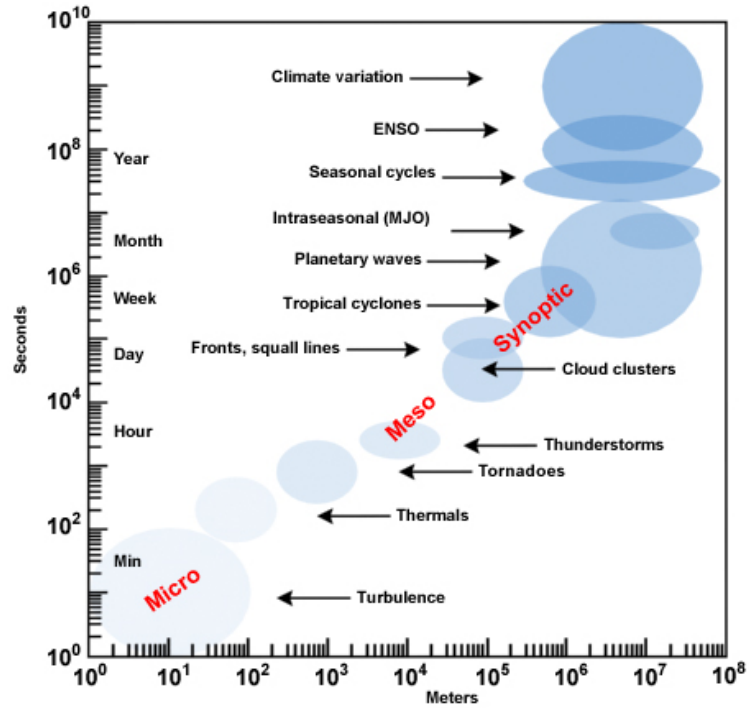


Fig. 2.9 Temporal and spatial of atmospheric processes and variations (COMET 2013).

Tab. 2.1 Classification of atmospheric scales after Orlandi (1975)

Scale	Macro-		Meso-			Micro-		
	α	β	α	β	γ	α	β	γ
from	Earth's circumf.	10 000 km	2000 km	200 km	20 km	2 km	200 m	20 m
to	10 000 km	2000 km	200 km	20 km	2 km	200 m	20 m	↓
e.g.,	Long waves, cyclones, anticyclones		Fronts, tropical cyclones, thunderstorms			Cumulus clouds, tornados		

difference between GCM output and the data demanded by impact researchers, stakeholders, and policy makers. These methods can be summarized to three basic categories:

1. dynamical downscaling using regional climate models (RCMs) (Dickinson et al. 1989; Giorgi and Bates 1989),
2. statistical downscaling (e.g., Hewitson and Crane 1996), and
3. stretched grid models (Schmidt 1977; Staniforth and Mitchell 1978).

Each of these approaches has its own advantages and disadvantages. A more detailed description and comparison is beyond the scope of this thesis. Interested readers are therefore referred to the references given above. Here I only want to concentrate on the first downscaling technique: dynamical downscaling with RCMs.

2.3 Regional Climate Modeling

The primary difference between GCMs and RCMs is that with the first the entire globe is simulated while the second is used for simulations on limited areas. Thereby, the model code (numerics, physics, . . . ; see Section 3.1) is very similar in GCMs and RCMs. In fact, simulating only a limited area is not a new idea since the first numerical weather forecast performed by the group of Jule Charney on ENIAC in 1950 (see Subsection 2.2.3) also only covered the continental United States.

The advantage of using RCMs compared to GCMs is that with RCM simulations with higher resolutions can be performed if the same computational resources are used. The concept of RCM downscaling is displayed in Figure 2.10. The basic idea is that the larger-scale atmospheric conditions from a driving model are used to force/drive an RCM at the lateral and surface boundaries. These so called boundary conditions are typically provided by GCMs, reanalyses³, or by another RCM with a coarser resolution. Usually, RCMs are *one-way coupled* with their driving model meaning that there is a flow of information from the lateral boundaries into the regional domain but no information is feedback to the driving model. In contrast, *two-way coupling* enables a feedback of information within the regional domain to the driving model. Therefore, the RCM and its driving model have to be simulated simultaneously on the same computer. The biggest advantage of this approach is the smoother transition between the driving model and the RCM at the lateral boundaries.

³In reanalyses historical states of the atmosphere are re-modeled by using an unchanged model and data assimilation scheme which includes all available observations over the period being analyzed. Therefore, reanalyse datasets are dynamically consistent estimate of atmospheric states of the past.

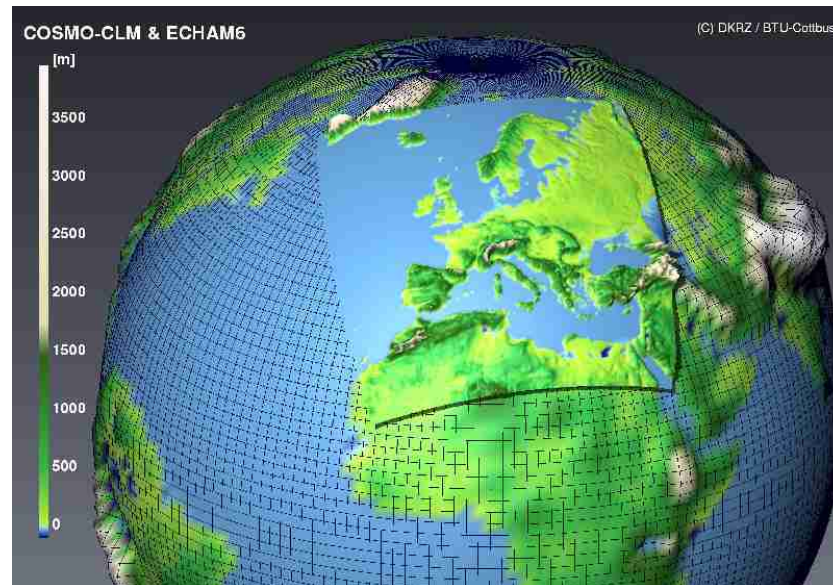


Fig. 2.10 Illustration of the concept of dynamical downscaling with an RCM (DKRZ and BTU Cottbus 2013).

2.3.1 Current Issues With RCMs

Simulating skillfully climate information on regional scales is not a trivial task. There are multiple issues occurring when RCMs are nested in larger scale models which are discussed in the upcoming paragraphs. For a high quality RCM simulation many aspects like the size and location of the domain, the application of nudging, the scale jump, the spin-up time/space, or the coupling strategy have to be considered. For finding the best suited setup, it is often necessary to test out multiple options before running an RCM.

2.3.1.1 Degrees of Freedom

How much freedom RCM simulations should have to be able to deviate from their lateral boundary conditions (LBCs) is a heavily discussed topic because RCMs should be able to produce more than just an expensive interpolating of its driving data. In this context also the error propagation from the driving data into the regional simulation is an important topic. If an RCM has only few degrees of freedom it has virtually no chance to correct errors which exist in its driving data.

Two aspects of RCM simulations are particularly important for its degree of freedom: the application of nudging and the size of the simulated area.

Nudging Nudging is a method to include large-scale information from the driving model (e.g., a GCMs) not only via the lateral boundaries of an RCM but also in the interior of its domain. It prevents the solution of a RCM from deviating too much from the large-scale solution of the driving data. Spectral nudging is the most common used technique (e.g., Kida et al. 1991; Sasaki et al. 1995; Waldron et al. 1996; Von Storch et al. 2000) even though there are also other approaches.

Von Storch et al. (2000) argues that with the application of spectral nudging RCM simulations are more related to downscaling compared to the traditional approach of dynamical downscaling which represents more or less a boundary value problem.

There have been both, studies showing advantages and disadvantages of nudging. For example, Winterfeldt and Weisse (2009) showed improvements in the wind speed distribution of nudged RCM simulations compared to the driving reanalysis data. However, studies by e.g., Radu et al. (2008) and Alexandru et al. (2009) showed disadvantages of nudging in the simulation of precipitation extremes and small-scale dynamic phenomena.

If nudging is applied in RCM simulations it is crucial to carefully consider which atmospheric fields should be nudged and how strong the nudging of these fields should be. Critics of nudging argue that it destroys the model's consistency and prohibits the influence of small-scale processes, which get resolved in the RCM, on the large scales.

Applying nudging in RCMs also implicates that the modeler trusts the correctness of the large-scale atmospheric patterns and dynamics in the driving data. This might be a reasonable assumption if reanalysis or short term weather forecast datasets are used as LBCs but is questionable when the data come from GCMs. This is because GCMs can have errors in the synoptic-scale dynamics which then are propagated even stronger into the RCM simulation.

Domain Size Beside nudging also the size of the regional domain is important and influences the dependence of an RCM simulation on its driving data. Small domain sizes generally limit the possibility of RCMs to develop atmospheric situations that deviate from those in the driving model.

A very powerful experiment to investigate the dependence of domain size on the solution of an RCM simulation is the *Big Brother/Little Brother* experimentation (e.g., Denis et al. 2002[b]; Denis et al. 2003; Antic et al. 2004; Dimitrijevic and Laprise 2005). Its setup is described in detail in Subsection 2.4.1.

The outcomes of the Big Brother/Little Brother experiments suggest that RCM domains have to have a delicate balance. They should be large enough to be able to simulate regional phenomena which might be related to e.g., orography or coastlines but also small enough so the solution cannot drift away from the large-scale forcing (Jones et al. 1995; Leduc and Laprise 2009). Drifting away from the forcing model solution

can result in problems at the boundaries where the large-scale field of the forcing data and those of the RCM do not match anymore. Additionally, the RCM would no longer downscale the solution of its driving data. However, this can also be intended if the large-scale patterns of the driving model are not fully trusted because regional effects (e.g., orography), which influence the large-scale flow, are missing.

Vannitsem and Chomé (2005) performed one-way nested RCM simulations above western Europe on different domains to investigate the impact of domain size on the quality of the simulation. They found a high sensitivity of the model quality on the domain size due to the different dynamics which can be realized dependent on the regional domain. In small domains the atmospheric flow showed only small deviations from the forcing data which was far from the real chaotic flow. The worst performance was found for intermediate domains while the best skill was found for their largest domain which covered almost a quarter of the Northern Hemisphere.

As a general guideline, supported by the findings of Rojas and Seth (2003), the selection of domain size should be motivated by the quality of the LBCs of the forcing model. If high quality forcing data are available smaller domains might be chosen to be more economic. However, if the driving data have deficiencies, large domains can at least partly compensate some of them.

2.3.1.2 Domain Location

Not only the domain size but also its location has impacts on the quality of RCM output (Rummukainen 2010). In general, the orientation of a regional domain should be chosen so that the impending large-scale flow from the driving model enters the domain as uniformly as possible. Furthermore, lateral boundaries should not cut through mountain ranges which generate dynamic phenomena or strong precipitation gradients. If features generated e.g., by orography are of interest, the source region of those features should be entirely captured within the domain or left outside if it is highly enough resolved in the driving model (Marbaix et al. 2003).

2.3.1.3 Resolution Difference

Another setup parameter which has to be chosen is the resolution difference between the driving model and the RCM. Rojas (2006) found that resolution difference up to 6 to 8 times of the resolution of the LBCs or somewhat larger can be chosen. For example, a GCM with 200 km horizontal grid-spacing allows for RCM gridspacings of approximately 25 km. To large resolution jumps can lead to strong disturbances at the boundaries of the RCM domain. However, successful RCM simulations have already been performed with larger resolution differences than 10 (Laprise 2008). The most important feature seems to be that the RCM domain spans several grid-meshes of the driving model.

If it is necessary to simulate on grid-spacings which are approximately 10 times smaller than those of the driving model, typically a multiple nesting approach is applied. Thereby, the downscaling is made in several steps. First, an RCM simulation is performed on a larger domain than the area of interest. Then a second simulation is made by using the output of the first one as LBCs and so on.

2.3.1.4 Spin-up

The generation of fine-scale features in RCMs from coarse-scale driving data needs some time and space which is usually called *spin-up* time/distance. Typically, most atmospheric fields have a rather short spin-up time of 1 to 2 days (Elía et al. 2002). However, some land-surface-fields have a much longer spin-up time of up to several years (e.g., soil water content in deep soil layers; Seneviratne et al. (2006)). For climate studies it is important to exclude this spin-up time in any statistical calculation.

In climate applications the spatial spin-up is as important as the temporal spin-up. It is the distance from the lateral boundaries to the point where the fine-scale structures reach their equilibrium amplitudes. It is not well defined how large the width of this spin-up region is but it is definitively larger than the buffer zone (for an explanation of the buffer zone see Subsection 2.3.1.5) (Laprise 2008). The spin-up width tends to depend on the flow speed and is therefore larger in the upper troposphere and on the side where the flow impinges on the domain. It also depends on the resolution difference between the LBCs and the RCM and increases for larger resolution jumps. Finally, the spin-up width is also a function of the strength of the acting free (hydrodynamic instabilities and non-linear processes) and forced (by surface processes) downscaling processes.

It is hard to say how far away from the boundaries the fine-scale features have reached their equilibrium. However, care has to be taken if small, computationally cheap, domains are used (approximately 50 by 50 grid-points) because they might be too small to allow the RCM to spin-up. This should be taken into account in the decision of the domain size (see Subsection 2.3.1.1).

2.3.1.5 Nesting and Lateral Boundary Conditions

The nesting of RCMs in coarser resolved forcing data is not an unproblematic task. Warner et al. (1997) discussed impacts of the lateral boundary problem on regional numerical weather simulations. As already discussed in Subsection 2.3.1.4 the influence of the LBCs on the RCM fields in the interior of the regional domain is dependent on the domain size. Déqué et al. (2007) noted that the influence of the LBCs on an RCM simulation varies with season, and is strongest in winter and in mid-latitude domains.

If very large regional domains are used (especially in summer) the solution of RCMs

is often only weakly controlled by the LBCs in the interior of their domains. This phenomenon is known as *intermittent divergence in phase space (IDPS)* (e.g., Von Storch 2005). If IDPS does occur large gradients develop especially downstream (at the exit region of the domain). In very severe cases un-meteorological features can develop within the domain so that the RCM can satisfy the LBCs. To prevent the occurrence of IDPS large-scale nudging can be applied with all the pros and cons discussed in Subsection 2.3.1.1.

2.3.1.6 One-way vs. Two-way Coupling

Many problems discussed in the previous subsections (e.g., IDPS and spatial spin-up) are enhanced, or even caused by, the one-way coupling of RCMs with their driving model. Two-way coupling allows for a feedback of the RCM to the driving model in the interior or downstream the computational domain and therefore reduces disturbances in the boundaries of the RCM. If two way coupling is applied both models have to be run simultaneously on the same computer. There are only a few studies which investigated the effect of two-way coupling between a GCM and an RCM. Results suggest a benefit of this approach in the global simulation, partly far away from the regional domain (Lorenz and Jacob 2005; Inatsu and Kimoto 2009).

2.4 Skill of RCM Simulations

Whether RCMs do increase the quality of their forcing model is an often asked question in climate science. Critics state that this is not the case and that RCMs even enlarge errors which exist in their driving data (e.g., Oreskes et al. 2010; Pielke and Wilby 2012; Kerr 2011).

Obviously the core potential of RCMs is their higher resolution which improves the representation of orographic features, surface fields (e.g., land cover, soil types), and makes the simulation of regional-scale dynamics possible. The finer grid-spacing also has the potential to improve synoptic-scale features like fronts and precipitation. Often these simulated fine-scale structures look very realistic like cloud filaments (similar to those on satellite pictures) or precipitation patterns (Laprise 2008). However, to quantify if these high resolution features are also meaningful and more correct is usually a challenging task.

2.4.1 Downscaling Ability of RCMs

One intuitive way to analyze the downscaling ability of RCMs is to compare their output with observations. If the skill to resemble the observations is higher in the RCM than

in its driving model one can assume that this RCM is able to downscale coarse scaled atmospheric information. However, this approach includes two major problems. First, it is hard to find high quality regional datasets that cover a climatological period. And second, errors which already exist in the driving model are propagating into the RCM via the LBCs. This means, it is close to impossible to distinguish if differences between a RCM simulation and observations are caused by errors in the LBCs, by the applied nesting technique, or by the RCM formulation.

René Laprise and his group at the Université du Québec Montréal proposed an elegant solution to overcome these problems. Laprise (2008) stated that: “The key issue relating to regional climate modelling is whether the climate of a high-resolution RCM simulation driven by low-resolution GCM, is equivalent to the climate of a reference simulation with a GCM with equivalent high resolution.” But also this approach faces some problems because running the same GCM in two resolutions will lead to two different atmospheric fields. Therefore, comparing the high-resolution GCM fields with those of the RCM will not only show effects from the nesting approach but also contain differences arising from the different resolutions in the GCM. To overcome this issue and to isolate the effects of the nesting approach itself the *Big-Brother Experiment* was designed (e.g., Denis et al. 2002[b]; Denis et al. 2002[a]; Denis et al. 2003; Antic et al. 2004; Dimitrijevic and Laprise 2005). As already discussed in Subsection 2.3.1.1, the Big-Brother Experiment consists of a high-resolution GCM simulation, which produces the reference against the RCM simulation is compared to and furthermore provides the LBCs for the RCM simulation. The RCM simulation itself is called the *Little-Brother*. The only thing that is still missing are the coarse-scale LBCs for the RCM. They are derived from the fine-scale GCM run by low-pass filtering the atmospheric fields to emulate a coarse-scale GCM simulation which is consistent with the large-scales in the high-resolution GCM run. The differences between the atmospheric fields of the Little-Brother run (the RCM simulation) to those of the Big-Brother (the high-resolution GCM simulation) can be now fully attributed to the nesting method of the RCM.

Unfortunately, due to the large computational costs of a high-resolution GCM simulation on climate time scale nobody has done this experiment so far. To make the experiment computationally more efficient, the high-resolution GCM simulation was replaced with a high-resolution RCM simulation with a large domain.

With the above described setup several downscaling experiments were performed by the Université du Québec Montréal (e.g., Denis et al. 2002[b]; Denis et al. 2002[a]; Denis et al. 2003; Antic et al. 2004; Dimitrijevic and Laprise 2005) which showed that the Little-Brother is able to “rather well” (Laprise 2008) reproduce the climate statistics of the small- and large-scale features of the Big-Brother for all simulated fields. These results indicate that RCMs are able to dynamically downscale low-resolution fields if the corresponding large scales are perfect. This assumption of perfect large-scale LBCs is a crucial point because generally GCM simulations have errors and are not perfect. As

discussed in Subsection 2.3.1.1 it is imaginable that the RCM can correct some of the large-scale errors in the GCM but errors might also be amplified when the large-scale flow interacts with small-scale forcing.

To investigate the effect of non-perfect large-scale forcing on an RCM the *Imperfect Big-Brother Experiment* has been supposed (Diaconescu et al. 2007). Beside the usage of perfect LBCs, additional LBCs are derived from simulations with a large-scale RCM which are performed with different resolutions and above different (large) domains. The variation of resolution and domain size produces controllable levels of errors and should mimic typical errors occurring in GCM simulations. Diaconescu et al. (2007) showed that their RCM does not increase nor amplifies the errors in the LBCs for the summer season over an Eastern North American domain. If large-scale errors are present in the LBCs the representation of small-scale features in the RCM is rather poor. Exceptions can be found at locations where strong small-scale surface forcing is present.

However, the above shown ability of RCMs to downscale large-scale LBCs correctly seems not to be a universal feature. By downscaling European Centre for Medium-Range Weather Forecasts 40 Year Re-analysis (ERA-40) with two different RCMs Castro et al. (2005) and Rockel et al. (2008a) showed that "... the utility of all regional climate models in downscaling global reanalysis primarily is not to add increased skill to the large-scale in the upper atmosphere, rather the value added is to resolve the smaller-scale features which have a greater dependence on the surface boundary." Furthermore, Castro et al. (2005) say that dynamical downscaling "... does not retain value of the large-scale over and above that which exists in the larger global reanalysis. If the variability of synoptic features is underestimated or there is a consistent bias in the larger model, no increased skill would be gained by dynamical downscaling."

More user oriented studies showed no improvements of large-scale features in RCMs but found added value compared to their forcing data at finer scales like in meso-scale structures and extremes (Christensen and Christensen 2001). In fact there are many studies which confirm this. For example, Feser (2006) showed improvements in precipitation patterns and Winterfeldt and Weisse (2009) found improvements in coastal winds compared to coarser models.

Facing these very controversy results there is a clear need to further investigate the downscaling ability of RCMs for different regions and different RCMs. Therefore the Big-Brother Experiment framework seems to be a well suited protocol.

2.4.1.1 Added Value in RCM Simulations

The ultimate goal of RCMs is to add information to larger-scale atmospheric fields which is beyond the resolvable scale of their LBCs. This directly indicates where someone should start searching for added value in RCMs; at the scales which are not resolved in

the LBCs hereafter called fine-scales (Laprise 2003; Feser 2006; Feser and Von Storch 2005).

The two major advantages in RCMs are the improved representation of meso-scale atmospheric dynamics and the better resolved small-scale surface forcings. In areas where surface forcing is strong, like in mountains or along coastlines, RCMs have the potential that also time-averaged and larger-scale fields are improved (Laprise 2008). Especially near the surface the RCM outputs can get substantially different from features in the low-resolution driving data.

The drawback, however, is that most of the time-stationary components of the variance are captured in the very large spatial scales away from the surface in the free atmosphere (Laprise 2008). At small-scales the variance of transient-eddy component generally dominates over the stationary components (Bielli and Laprise 2006). This means, averaging over climatic time scales tend to remove added value except in areas with small-scale surface forcing. Laprise (2008) stated therefore: "... the added value of RCMs is likely to lie mostly in frequency distributions and high-order statistics, reflecting more intense or localised weather events such as intense precipitation events."

2.5 Convection Permitting Simulations

Like in the development of GCMs (see Subsection 2.2.4) also RCMs got more and more complex and the grid-spacing of their simulations constantly decreased since their rise in the late 1980s.

The horizontal grid-spacing of state-of-the-art RCMs typically ranges from 50 km to approximately 25 km; PRUDENCE: 50 km (e.g., Christensen and Christensen 2007), ENSEMBLES: 25 km (Linden and Mitchell 2009), NARCCAP: 50 km (Mearns et al. 2009).

More recently, due to advancements in the field of computer sciences, it is possible to have higher-resolved climate simulations with approximately 10 km horizontal grid spacing (e.g., Loibl et al. 2011; Gobiet and Jacob 2012). Nevertheless, even with a mesh size of 10 km there are still numerous processes which cannot be resolved on the model grid and therefore have to be parameterized. These parameterizations are important sources of model errors (e.g., Randall et al. 2007) and introduce large uncertainties in the projection of future climate (e.g., Déqué et al. 2007).

Especially cloud processes (e.g., cloud albedo effects) belong to the least understood processes in the atmosphere and contribute the largest amount of uncertainty to changes in the radiative forcing⁴ of past climate change (Solomon et al. 2007).

⁴Radiative forcing is defined as: "a systematic perturbation to the climatological value of the net radiant flux density at some point in the earth's climate system." Source: AMS glossary 2013.

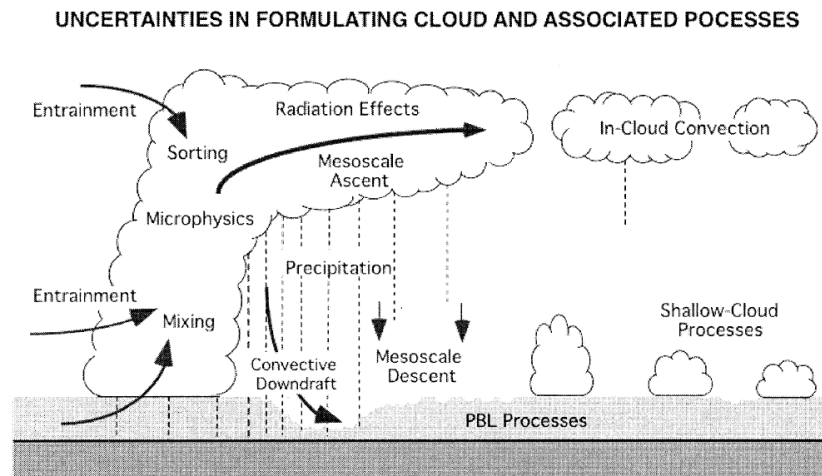


Fig. 2.11 Processes in the modeling of clouds with major uncertainties in the mathematical formulations (Arakawa 2004).

As depicted in Figure 2.12 clouds and their physical effects influence the climate system in the following ways (Arakawa 1975):

- by coupling dynamical and hydrological processes in the atmosphere through the heat of condensation and evaporation and through redistributions of sensible and latent heat and momentum;
- by coupling radiative and dynamical-hydrological processes in the atmosphere through the reflection, absorption, and emission of radiation;
- by influencing the hydrological processes in the ground through precipitation; and
- by influencing the coupling between the atmosphere and oceans (or ground) through modifications of radiation and planetary boundary layer (PBL) processes.

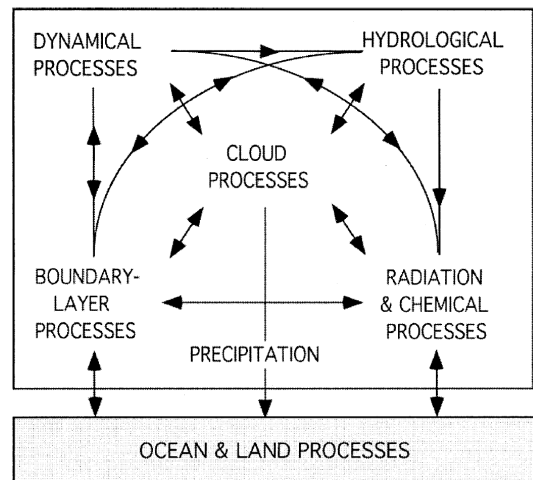


Fig. 2.12 Interaction of various processes in the climate system (Arakawa 2004).

As visible in Figure 2.12 most of these interactions have a feedback and contain non-linear processes. Cumulus convection is probably the most important process in those interactions and modeling cumulus convection (which is done with cumulus parameterizations) was almost always a central part in the history of modeling the atmosphere (Arakawa 2004). Over the past decades numerous cumulus parameterization schemes were developed which did not essentially decrease the uncertainties in how to model clouds and associated processes like those depicted in Figure 2.11.

Convection parameterizations are a known source of errors in simulations of present climate and NWP and cause large uncertainties in future climate projections (e.g., Molinari and Dudek 1992; Dai et al. 1999; Brockhaus et al. 2008). For example, a well known problem of many convection parameterization schemes which are used in climate and NWP models is a too early onset and maximum peak of convective processes during the day. In different GCMs shifts of several hours have been found in the mid-latitudes (Dai and Trenberth 2004; Lee et al. 2007) and also in the tropics (Yang and Slingo 2001; Bechtold et al. 2004). The same problem has been found in RCM simulations of summertime precipitation over the eastern European Alps (Prein et al. 2013[a]) and over the mainland of the USA (Dai et al. 1999).

Another problem of convection parameterizations in meso-scale climate simulations is the coexistence of explicit convective clouds, with parameterized clouds, and only rudimentarily simulated real clouds (Molinari and Dudek 1992). One solution to this problem is to either increase the grid-spacing and avoid grid-scale cumulus clouds or drop the grid-spacing to a scale where cumulus parameterizations can be avoided. Weisman et al. (1997) explored how small the horizontal grid-spacing has to be chosen to explicitly resolve deep convection. They found that most features of deep convection are reasonably well represented on grids smaller than 4 km.

Nevertheless, there were several studies that reported convection permitting simulation (CPS) deficiencies due to insufficiently small grids. For example, Petch et al. (2002) showed that deep and shallow convection are delayed in a simulation with 800 m horizontal grid-spacing compared to a 125 m simulation. Langhans et al. (2012) investigated this topic by performing convection permitting simulations with different horizontal grid spacings (4.4 km, 2.2 km, 1.1 km, and 0.55 km). They concentrated on regional scale properties of deep convection by analyzing bulk heat and moisture budgets (but also precipitation). They found that the investigated bulk properties are converging numerically and physically towards the 0.55 km solution. Thereby, the bulk property differences are small between the simulations. They conclude that: “Despite some sensitivities related to the applied turbulence closure, the results support the feasibility of kilometer-scale models to appropriately represent the bulk feedbacks between moist convection and the larger-scale flow” (Langhans et al. 2012).

2.5.1 Important Components of Convection Permitting Models

Many parameterization schemes which are used in RCMs were developed for GCMs. However, assumptions and parameters which are appropriate in GCM or standard RCM simulations (on the β -meso-scale) might be no longer valid on convection-permitting scales (γ -meso-scale to α -micro-scale; cf. Table 2.1).

A prominent example for this is the hydrostatic approximation (e.g., Warner 2011). It is widely used in many forecast and climate models to simplify the primitive equations and make the model more computational efficient. Efficiency is gained because a hydrostatic version of the primitive equations does not admit sound waves which demand for a small model time step because of their fast propagation speed. Using a form of the equations which does not include sound waves is desirable because they generally have no meteorological importance.

The hydrostatic approximation assumes that the pressure gradient force in the third equation of motion (see Equation 2.3) is equal to the gravity force. Therefore, Equation 2.3 is replaced with:

$$\frac{\partial p}{\partial z} = -\rho g. \quad (2.10)$$

In this equation the density is proportional to the pressure gradient. Therein, sound waves are not possible because they demand the density to adjust along the longitudinal compression and expansion within the waves. The hydrostatic assumption is valid as long as the neglected terms in Equation 2.3 are at least an order-of-magnitude smaller than the remaining terms. This means:

$$\left| \frac{dw}{dt} \right| \ll g. \quad (2.11)$$

This assumption is fulfilled for synoptic-scale motions but is no longer valid for length scales below approximately 10 km (e.g., Holton 2004; Dutton 1976). This means hydrostatic climate models are not suitable for CPCs.

An example for the importance of using a non-hydrostatic model for highly resolved simulations of the atmosphere is shown in Figure 2.13. Depicted are the cross sections of vertical velocities in idealized flow simulations (5 km horizontal grid-spacing) over a 100 m high mountain at the equator. The reference solution (panel a) is derived from a simulation with the state-of-the-art Eulerian/semi-Lagrangian fluid solver (EULAG) model (Prusa et al. 2008). In panel (b) the solution of the Integrated Forecast System (IFS) with a non-homeostatic and in panel (c) with a hydrostatic core is depicted. The non-hydrostatic model is able to reproduce horizontally propagating gravity waves as seen in the EULAG solution while the hydrostatic model produces vertically propagating

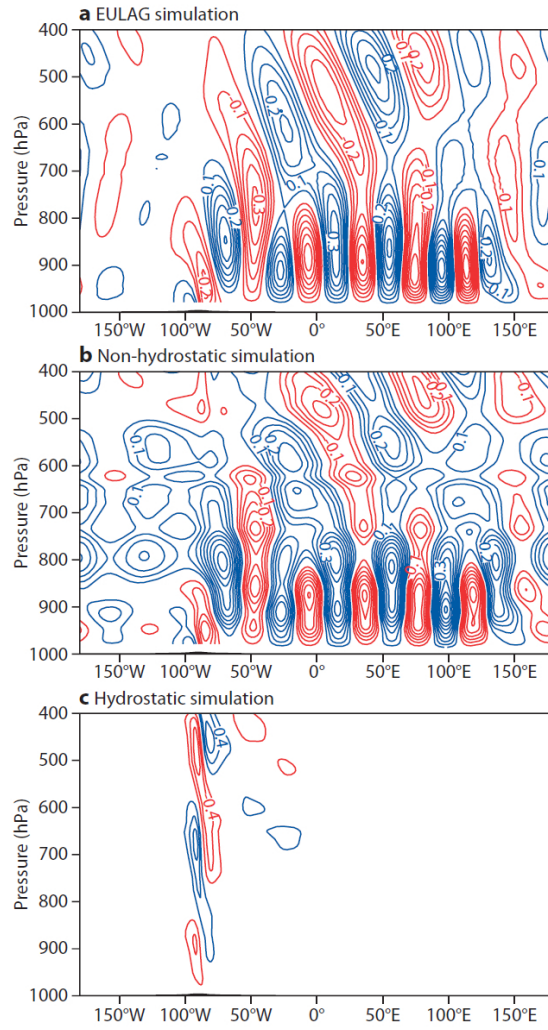


Fig. 2.13 Vertical velocity in an idealized flow simulation at the equator with the non-hydrostatic EULAG model (a) and the corresponding non-hydrostatic (b) and hydrostatic (c) IFS simulations (Wedi and Malardel 2010).

gravity waves. An example of such flow patterns in the real atmosphere can be seen in Figure 2.14.

When a non-hydrostatic model is used at convective-permitting scales, vertical motions are no longer derived diagnostically (like in a hydrostatic model) but solved prognostically which is necessary for the adequate representation of deep convection and boundary driven gravity waves (Wedi and Malardel 2010). However, since deep convective clouds are no longer parameterized it is important to have a correct representation of cloud processes, especially phase changes of water, because they are the source of energy for the uplifting of air. Thereby, the treatment of additional hydrometeors like snow, cloud ice, and graupel get important.

Liu et al. (2011) investigated the sensitivity of simulating winter precipitation with a CPCS (4km grid-spacing) on physical parameterizations. They found that orographic precipitation is highly sensitive to the used cloud microphysics scheme. They tested seven different schemes which are implemented in the Weather Research and Forecasting Model (WRF). Two of them (the Thompson et al. (2008) and Morrison et al. (2009) bulk microphysics schemes) outperformed the others which produced 30 % to 60 % too much precipitation. Between the used schemes there were significant differences apparent in: “domain averages, spatial distributions of hydrometeors, latent heating profiles, and cloud fields” (Liu et al. 2011). Only moderate too weak sensitivities were found concerning the land surface, PBL, and radiation schemes.

A further critical aspect in CPSs is the initialization of deep convection. Therefore, an accurate parameterization of the PBL is crucial (Baldauf et al. 2011). Critical processes in the PBL are its mixing, the formation of cloud layers, and its stratification. Generally helpful for a accurate representation of processes within the PBL is a high vertical resolution close to the surface. Models with parameterized deep convection are less sensitive to errors in the PBL because the triggering of deep convection is parameterized.

In convection-permitting simulations also local or regional forcing of orography and surface fields which were negligible at coarser scales can get important. One example is orographic shading which can induce local and regional wind systems that are important

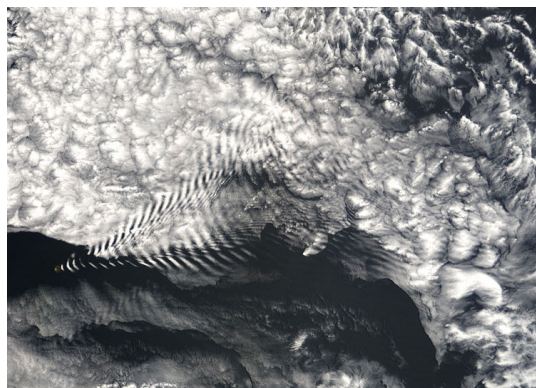


Fig. 2.14 Mountain lee wave propagation at Amsterdam Island at the 19 December 2005 taken by the NASA MODIS satellite (NASA 2013).

for the climate of a region. Another example is the treatment of lakes or cities which are poorly resolved in coarser gridded simulations. Related to this topic is the availability of highly resolved surface boundary conditions (e.g., land use, land type, soil type) which is often a problem in CPCs.

2.5.2 Added Value in Convection Permitting Simulations

Convection permitting climate modeling is a rather young scientific field and is far from being established because of the tremendous demand of computational resources. Therefore, it is still quite unknown how large the added value of CPCs compared to state-of-the-art RCM simulations is. However, there are some theoretical considerations which can help to answer this question.

The most important advantage of CPCs is the ability to avoid error-prone cumulus parameterization schemes by resolving deep convection explicitly (as already discussed in Section 2.5). Beside that the high-resolution enables a more realistic representation of orography and surface fields which again can influence atmospheric dynamics.

In this subsection I will investigate the added value of CPCs in NWP and in climate applications.

2.5.2.1 Convection Permitting Simulations in Numerical Weather Forecasting

In NWP convection resolving models are already widely used for operational forecasts and research purposes (e.g., Mass et al. 2002; Kain et al. 2006; Schwartz et al. 2009; Gebhardt et al. 2011). For example, the Deutscher Wetterdienst (DWD) uses the COSMO model for operational convection permitting forecasting with 2.8 km horizontal grid-spacing since April 2007. Baldauf et al. (2011) conclude that this high-resolution model is able to improve the forecast quality of location, timing, and severity of deep convection and has a better precipitation forecast in summer compared to coarser resolved simulations with parameterized deep convection.

For convection resolving forecasts with the UK Met Office's Unified Model (UM) Roberts and Lean (2008) found a similar result. They showed with the help of the fractions skill score (FSS) method that their 1 km model is able to more accurately simulate the distribution of precipitation and improves the predictability of high accumulations compared to a 12 km model. However, the 1 km model overestimated the precipitation amounts. Forecasts with a 4 km model could not achieve the skill of the 1 km model.

Weusthoff et al. (2010) investigated forecasts from three different NWP models over Switzerland with the FSS (see Roberts and Lean (2008) or Subsection 3.2.2.1) and the upscaling method (see Zepeda-Arce et al. (2000) or Subsection 3.2.2.1) and found significant improvements particularly for convective, more localized precipitation events.

2.5.2.2 Convection Permitting Simulations in Climate Applications

One of the first studies which investigated the performance of CPCSs was done by Grell et al. (2000). They used the Fifth-Generation NCAR/Penn State Mesoscale Model (MM5) to simulate a 14 month period with up to 1 km horizontal grid-spacing covering the Loisach Valley and parts of the Wetterstein and Karwendel massifs in the European Alps. They found that the domain average precipitation increases the higher the resolution of the model is. This is strongest in the winter season because of stronger upslope winds due to the better resolved orography. In summer the effect of daytime thunderstorm development and movement of convective cells could only be simulated with convection permitting resolutions.

Hohenegger et al. (2008) analyzed the performance of a CPCS with 2.2 km grid-spacing covering the entire Alpine Region. They used CCLM to simulate the weather in July 2006 and compared the data to observations and a coarser CCLM run with 25 km grid spacing. They concluded that: “the cloud-resolving resolution yields a more accurate spatial localization of the precipitation maxima, reduces the cold bias, and especially reproduces a better timing of the convective diurnal cycle” (Hohenegger et al. 2008).

In another study, Hohenegger et al. (2009) investigated the soil moisture-precipitation feedback with the same model, region, and time period as described in the paragraph above. They performed one control and two sensitivity studies with perturbed soil moisture. Previous studies have suggested a positive soil moisture feedback (e.g., Betts et al. 1996; Eltahir 1998; Schär et al. 1999; Pal and Eltahir 2001; Findell and Eltahir 2003) meaning that wet soil leads to more precipitation. Hohenegger et al. (2009) found a strong positive soil moisture-precipitation feedback in their coarse resolution (25 km) simulation with parameterized deep convection while their CPCS (2.2 km) shows a predominantly negative feedback. The reason for this is a stable layer which is on top of the PBL. The stronger sensible heating above the drier soil leads to stronger thermals in the CPCS which can more easily break through the stable layer which then leads to more deep convection and a negative soil moisture-precipitation feedback. The initialization of deep convection is much less sensitive to this stable layer in the 25 km model because of the formulation of the applied deep convection parameterization. However, they also found that there are considerable differences in the feedback mechanism if different convection parameterizations are used.

Rasmussen et al. (2011) concentrated on the effects of different grid spacings on the simulation of snowfall in the headwaters of the Colorado River. Therefore, they simulated four cold seasons with the WRF RCM with four different horizontal grid-spacings (2 km, 6 km, 18 km, and 36 km). In the 2 km and 6 km simulations no deep convection parameterization is used. The findings of this study suggest that global and regional models with grid-spacing larger 18 km underestimate snow in high elevations by 20 % to 40 % and overestimate it in low elevations by a similar amount. With grid-spacings

lower than 6 km the WRF model was able to reproduce water-year accumulated snowfall within 20% for two thirds of the used observation sights. Ikeda et al. (2010) confirm these results and conclude that: “Comparison of high-resolution WRF simulations of seasonal snowfall to SNOTEL observations over the Colorado Headwaters regions show very good agreement if a grid-spacing of <6 km is used” (Ikeda et al. 2010).

One of the first studies which analyzed CPS on climate time scales was performed by Kendon et al. (2012). They performed two simulations with the UM model: One simulation with 12 km and one CPCS with 1.5 km horizontal grid-spacing, covering the southern part of the United Kingdom between 1989 and 2008. Heavy rainfall in the 1.5 km model has a more realistic duration and spatial extent compared to the 12 km simulation. The 12 km model simulates too weak heavy precipitation while the 1.5 km run tends to overestimate the intensity. The 1.5 km model furthermore removes the tendency for too much drizzling in the UM and corrects errors in the diurnal cycle of precipitation.

Pryor et al. (2012) investigated the influence of horizontal grid-spacing in the Rossby Centre version 3 (RCA3) RCM on the wind climate in a flat region centered over Denmark. Therefore, the period 1987 to 2008 was simulated with 50 km, 25 km, 12.5 km, and 6.25 km horizontal grid spacing. The mean wind speed 10 m above ground increases by 5% when the grid-spacing is reduced from 50 km to 6.25 km. Stronger signals are visible in the 50 year return level wind speed and wind gusts which increase by 10% respectively 24%. At the lowest model level (approximately 70 m) these increases are stronger and show approximately 10% in the mean and approximately 20% in the 50 year return period. The found increases in wind speed are in the same order of magnitude as the climate change signals in this region. However, comparisons with in situ observations did not show improvements at synoptic and meso- α time scales in the higher resolved simulations.

Summing up the findings of the above discussed studies, the main added value of CPCS compared to coarser gridded simulations are:

- better timing of the convection diurnal cycles (Hohenegger et al. 2008; Kendon et al. 2012),
- improved location and extend of heavy convective precipitation (Hohenegger et al. 2008; Kendon et al. 2012),
- removed drizzling problem (Kendon et al. 2012),
- more accurate distribution of snow (Rasmussen et al. 2011; Ikeda et al. 2010), and
- improved simulation of the snowpack and runoff (Rasmussen et al. 2011; Ikeda et al. 2010).

This thesis builds up on these results and extends them by investigating the common added value of an ensemble of CPCS (see Section 4.1). In addition to precipitation,

also two meter temperature, relative humidity, and global radiation are analyzed. For the evaluation of precipitation fields advanced statistical methods, which are commonly used in NWP (see Subsection 2.5.2.1) are applied.

Based on the findings of the CPCS ensemble evaluation and published literature a second study focuses on the representation of summer- and wintertime extreme precipitation events in complex terrain simulated with the WRF model in three horizontal grid-spacings (see Section 4.2). The simulations are analyzed on different spatial scales to investigate the effect of upscaling of small-scale features in CPCSs to coarser scales.

3

Dynamical Downscaling and Detecting Added Value

3.1 Dynamical Downscaling with RCMs on the Example of CCLM

THIS section gives an overview on the formulation of regional climate models (RCMs) on the example of the COSMO model in CLimate Mode (CCLM). Thereby, the model dynamics (Subsection 3.1.1), numerics (Subsection 3.1.2), and physics (Subsection 3.1.3) are briefly described. The goal is to give an idea how state-of-the-art RCMs are built up, which processes are considered, and which assumptions are taken. Readers who are interested in a more general and holistic description of weather and climate models are referred to textbooks like Warner (2011) or Washington and Parkinson (2005).

3.1.1 Dynamics

The dynamical cores of three dimensional climate models are based on the primitive equations (see Equations 2.1 to 2.7). As discussed in Subsection 2.2.1 these equations combine the Newton's law of motion, the hydrodynamic state equation, the thermodynamic energy equation, and the mass conservation to a set of non-linear, non-homogeneous, prognostic coupled, partial differential equations.

The dynamics of CCLM are based on the full set of primitive equations and describe

non-hydrostatic, compressible flow in a moist atmosphere (Doms 2011). CCLM is designed for regional climate modeling and numerical weather forecasting on the meso- β to meso- γ -scale.

The equations are formulated in rotated geographical coordinates and general terrain following height coordinates (Doms 2011).

$$\frac{\partial u}{\partial t} = - \left\{ \frac{1}{a \cos \phi} \frac{\partial E_h}{\partial \lambda} - v V_a \right\} - \zeta \frac{\partial u}{\partial \zeta} - \frac{1}{\rho a \cos \phi} \left(\frac{\partial p'}{\partial \lambda} - \frac{1}{\sqrt{\Gamma}} \frac{\partial p_0}{\partial \lambda} \frac{\partial p'}{\partial \zeta} \right) + M_u \quad (3.1)$$

$$\frac{\partial v}{\partial t} = - \left\{ \frac{1}{a \cos \phi} \left(u \frac{\partial w}{\partial \lambda} + v \cos \phi \frac{\partial w}{\partial \phi} \right) \right\} - \zeta \frac{\partial v}{\partial \zeta} + \frac{g}{\sqrt{\Gamma}} \frac{\partial p'}{\partial \zeta} + M_w \quad (3.2)$$

$$\begin{aligned} \frac{\partial w}{\partial t} = & - \left\{ \frac{\partial E_h}{\partial \phi} + u V_a \right\} - \zeta \frac{\partial w}{\partial \zeta} - \frac{1}{\rho a} \left(\frac{\partial p'}{\partial \phi} - \frac{1}{\sqrt{\Gamma}} \frac{\partial p_0}{\partial \phi} \frac{\partial p'}{\partial \zeta} \right) + M_v \\ & + g \frac{\rho_0}{\rho} \left\{ \frac{T - T_0}{T} \frac{T_0 p'}{T p_0} + \left(\frac{R_v}{R_d} - 1 \right) q^v - q^l - q^f \right\} \end{aligned} \quad (3.3)$$

$$\frac{\partial p'}{\partial t} = - \left\{ \frac{1}{a \cos \phi} \left(u \frac{\partial p'}{\partial \lambda} + v \cos \phi \frac{\partial p'}{\partial \phi} \right) \right\} - \zeta \frac{\partial p'}{\partial \zeta} + g \rho_0 w - \frac{c_{pd}}{c_{vd}} p D \quad (3.4)$$

$$\frac{\partial T}{\partial t} = - \left\{ \frac{1}{a \cos \phi} \left(u \frac{\partial T}{\partial \lambda} + v \cos \phi \frac{\partial T}{\partial \phi} \right) \right\} - \zeta \frac{\partial T}{\partial \zeta} - \frac{1}{\rho c_{vd}} p D + Q_T \quad (3.5)$$

$$\frac{\partial q^v}{\partial t} = - \left\{ \frac{1}{a \cos \phi} \left(u \frac{\partial q^v}{\partial \lambda} + v \cos \phi \frac{\partial q^v}{\partial \phi} \right) \right\} - \zeta \frac{\partial q^v}{\partial \zeta} - (S^l + S^f) + M_{q^v} \quad (3.6)$$

$$\frac{\partial q^{l,f}}{\partial t} = - \left\{ \frac{1}{a \cos \phi} \left(u \frac{\partial q^{l,f}}{\partial \lambda} + v \cos \phi \frac{\partial q^{l,f}}{\partial \phi} \right) \right\} - \zeta \frac{\partial q^{l,f}}{\partial \zeta} - \frac{g}{\sqrt{\Gamma}} \frac{\rho_0}{\rho} \frac{\partial P_{l,f}}{\partial \zeta} + S^{l,f} + M_{q^{l,f}} \quad (3.7)$$

$$\rho = p \left\{ R_d [1 + (R_v/R_d - 1) q^v - q^l - q^f] T \right\}^{-1} \quad (3.8)$$

The following symbols are used in Equations 3.1 to 3.8:

3.1 Dynamical Downscaling with RCMs on the Example of CCLM

Γ	variation of reference pressure
ϕ	latitude
T_0	constant reference temperature
T	temperature
a	radius of the earth
c_{pd}	specific heat capacities of dry air at constant pressure
c_{vd}	specific heat capacities of dry air at constant volume
D	three-dimensional wind divergence
E_h	kinetic energy of horizontal motion
g	acceleration of gravity
λ	longitude
M_u	source terms due to turbulent mixing in u
M_v	source terms due to turbulent mixing in v
M_w	source terms due to turbulent mixing in w
M_{q^v}	source terms due to turbulent mixing in q^v
$M_{q^{l,f}}$	source terms due to turbulent mixing in $q^{l,f}$
p'	pressure perturbation from p_0
p_0	constant reference pressure
$P_{l,f}$	absolute values of the gravitational diffusion fluxes of water and ice
q^f	mass fraction of ice
q^l	mass fraction of water
Q_T	diabatic heating term
q^v	mass fraction of water vapor
R_d	gas constant for dry air
ρ_0	constant reference density
ρ	density
R_v	gas constant for water vapor
S^l	cloud microphysical sources/sinks per unit mass of moist air
u	zonal wind velocity
V_a	vertical component of absolute vorticity
v	meridional wind velocity
w	vertical velocity
$\dot{\zeta}$	nonnormalized contravariant vertical velocity
ζ	terrain following vertical coordinate

Comparing Equations 3.1 to 3.8 with the primitive equations (2.1 to 2.7) reveals, that there are many terms that look different or pop up in the equations used in the CCLM. This is necessary because of assumptions in the model or adaptations which are made to make the model more efficient for computing.

For example, Equation 3.7 enables to calculate temporal changes of atmospheric water

and ice prognostically which is not included in the original primitive equations.

Additional terms appear because of the transformation of curvilinear but orthogonal spherical coordinate system with geometrical height z to a height following coordinate system with the new terrain following vertical coordinate (ζ). This transformation avoids a costly formulation of the surface boundary conditions which would be necessary if z coordinates would be used in the model (Doms 2011). In terrain following coordinates this is omitted because the lowest level of constant vertical coordinates follows the orography. In CCLM a hybrid vertical coordinate system is used with terrain following levels between the surface orography height and a defined height where the levels convert back to flat horizontal fields. In the current version of CCLM the height-based hybrid smooth level vertical (SLEVE) coordinate system (Schär et al. 2002) is used.

The thermodynamic variables (T , P , and ρ) in the CCLM are split into a sum of a base state and deviations thereof (Doms 2011). Thereby, the base state is horizontally homogeneous (depends only on the height above the surface), time invariant, and in hydrostatic balance. This is beneficial because horizontal pressure gradients are removed from the base state pressure. If pressure does not deviate too strongly from the reference pressure, calculating with the difference can be beneficial for the computational accuracy of calculating the pressure gradient force when sloping coordinate surfaces occur (which is the case because of the terrain following vertical coordinate system).

With the Equations 3.1 to 3.8 the complete set of the thermodynamic state variables is defined. The prognostic variables therein are zonal wind velocity (u), meridional wind velocity (v), vertical velocity (w), temperature (T), pressure perturbation from p_0 (p'), density (ρ), mass fraction of water vapor (q^v), mass fraction of water (q^l), and mass fraction of ice (q^f). These variables are defined if the mixing terms M , the sources and sinks of cloud microphysical sources/sinks per unit mass of moist air (S^l) as well as the absolute values of the gravitational diffusion fluxes of water and ice ($P_{l,f}$), additionally to the diabatic heating term (Q_T) are known. These variables are calculated as functions of the prognostic variables by various parameterization schemes.

To solve the model equations finite differencing methods are necessary which are discussed in the next Subsection 3.1.2.

3.1.2 Numerics

To solve Equations 3.1 to 3.8 constant increments of the independent variables ($\Delta\lambda$, $\Delta\phi$, and $\Delta\zeta$) are used as setup for the computational grid (Doms 2011). With this method it is possible to derive a finite computational (λ , ϕ , ζ)-space with grid-points (i,j,k) with i in the λ -direction, j in the ϕ -direction, and k in the ζ -direction. The location of the grid-points in the three dimensional grid is derived by:

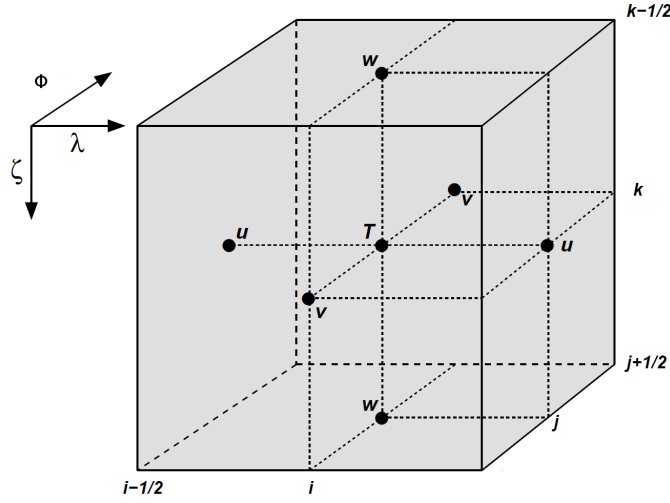


Fig. 3.1 A grid-box in the CCLM displaying the Arakawa-C/Lorenz staggering of the dependent variables (Doms 2011).

$$\begin{aligned}
 \lambda_i &= \lambda_0 + i \cdot \Delta\lambda, & i &= 0, \dots, N_\lambda, \\
 \phi_j &= \phi_0 + j \cdot \Delta\phi, & j &= 0, \dots, N_\phi, \\
 \zeta_k &= k \cdot \Delta\zeta, & k &= 0, \dots, N_\zeta.
 \end{aligned} \tag{3.9}$$

In Equation 3.9 N_λ , N_ϕ , and N_ζ denote the number of grid-points in the λ -, ϕ -, and ζ -direction, respectively. The south-western corner of the model domain is defined by λ_0 and ϕ_0 . Each grid-point (i, j, k) represents the center of a volume with the side length $\Delta\lambda$, $\Delta\phi$, and $\Delta\zeta$. The sides of the grid-boxes are located at $\lambda_{i+1/2}$, $\phi_{j+1/2}$, and $\zeta_{k+1/2}$.

In Figure 3.1 the Arakawa-C/Lorenz staggering of scalars (located in the center) and velocity components (located at the box faces) within a grid-box of CCLM is shown.

The extend of the computational domain is smaller than the total domain size to be able to implement boundary conditions. This means that the lateral physical boundaries have an offset from the outer boundaries. The region within this offset is called boundary zone. Default two grid points are used for the width of the boundary zone. This width can be larger (but not smaller) than two grid-points. For all points within the model domain (excluding the boundary zone) the model equations are solved. The variables in the boundary zone are set to the specified boundary values.

To avoid inconsistencies and to get a smooth transition between the lateral boundary conditions (LBCs) and the model solution a relaxation zone is introduced. The high-resolution CCLM fields are adjusted gradually within this zone to fit the LBCs of the

driving model. Therefore, a relaxation boundary condition is defined which is similar to that proposed by Davies (1976) and Davies (1983). In CCLM an attenuation function (α_b) is calculated which controls the strength of the LBCs influence on the model solution (Kallberg 1977):

$$\alpha_b = 1 - \tanh\left(\frac{d}{2\Delta x}\right). \quad (3.10)$$

In Equation 3.10 Δx denotes the horizontal grid-spacing and d is the distance from the lateral boundary. If $d = 0$ then $\alpha_b = 1$ and if $d \gg \Delta x$ then $\alpha \rightarrow 0$. Usually, 8 grid-points are directly affected by the LBCs (Doms 2011).

Vertically, grid stretching is applied for higher efficiency. Thereby, the distance of vertical model levels is smaller near the surface and gets larger in higher altitudes.

Since the CCLM is a non-hydrostatic model with a compressible model atmosphere sound waves, which are not important for meteorological fields, are part of the model solutions (cf., Subsection 2.5.1). For a more efficient computation, the prognostic equations are split into terms which are related to fast propagating acoustic waves and terms which are related to slow moving waves according to the method described by Klemp and Wilhelmson (1978). How this mode splitting is implemented in the CCLM can be seen in Doms (2011).

Due to the time splitting there are two time steps used in the model. A shorter one for sound waves and a longer one for slow moving waves (Δt). The discrete time levels are therefore $t = t_0 + n\Delta t$ where n is the time step counter and t_0 is the starting time of the simulation.

Two numerical time integration schemes are available in CCLM. The first one is the Leapfrog-scheme which has second-order accuracy (Klemp and Wilhelmson 1978). The second one is the Runge-Kutta-scheme and was implemented due to the need for decreasing numerical noise at the grid-scale for convection permitting simulations. It is adapted from the time-slitting approach of Wicker and Skamarock (2002).

The 3rd-order Runge-Kutta-scheme works with a 5th-order advection upwind scheme which takes care of the horizontal advection of the dynamic variables (Doms 2011). Thereby, the tendencies of the two horizontal directions are added. Formally the used Runge-Kutta-scheme is of 2nd-order accuracy but has 3rd-order accuracy for linear problems. Combined with the 5th-order advection scheme it is one of the most effective schemes of this type (Baldauf 2008). More details about the implementation of this scheme can be found in Doms (2011).

Numerical smoothing is introduced to artificially damp small-scale computational noise around two grid interval wavelengths ($2\Delta x$) and to prevent the initiation and growth of non-linear instabilities (Doms 2011). Numerical noise is introduced by nu-

merical dispersion especially in the Leapfrog-scheme. Small-scale noise can also occur because of aliasing and may lead to weak non-linear numerical instabilities. Furthermore, physical processes which generally act on a grid-point basis will generate $2\Delta x$ waves.

In CCLM time filtering is implemented which helps to avoid high-frequency oscillations. In addition, multiple options for spatial numerical smoothing are implemented which typically use horizontal diffusion and Rayleigh damping. They are applied to avoid reflections of gravity waves from the upper boundary of the model. For the descriptions of those methods see Doms (2011) and the literature therein.

In convection permitting simulations numerical smoothing with horizontal diffusion can lead to systematic biases. This is because in a terrain following coordinate system over complex orography horizontal diffusion leads to unwanted vertical mixing. Since orography is generally getting steeper when the horizontal grid-spacing is reduced this problem gets more severe in highly resolved simulations (Doms 2011). For example, horizontal diffusion of temperature will tend to cool the valleys and heat up the mountain tops. The same can happen to atmospheric moisture which is diffused from the valleys to the mountain tops.

The usage of a reference atmosphere helps to reduce these errors in the CCLM. For instance, the unwanted vertical mixing of temperature will be zero if the vertical temperature gradient is equal to the gradient used in the reference atmosphere. However, large errors can still occur if the stratification is very different from those in the reference atmosphere (i.e., for very stable or unstable stratification).

To furthermore reduce these errors a flux-limited scheme is used in the CCLM. This scheme enables to reduce orographic induced biases and avoids mass-conservation errors by artificially reducing the fluxes according to the steepness of the model surface. The implemented scheme reduces the fluxes gradually with increasing steepness of the terrain-following coordinates. The fluxes become zero if a threshold height difference between two neighboring grid-points is exceeded. This threshold is 250 m (namelist-switch `hd_dhmax`) by default (fitted to a grid-spacing of 7 km) and should be adjusted accordingly if the horizontal grid-spacing is changed.

High-resolution modeling in complex terrain leads to another long-standing problem which is the simulation of unrealistic high precipitation values above mountain tops and too less precipitation in valleys (Doms 2011). One reason for this is the usage of average altitudes of grid-cells which leads to solitary (single grid-cell) mountain tops and valley floors. This introduces un-physical feedbacks to the simulated flow affecting the model physics in inaccurate ways. Investigations of this behavior (e.g., Gassmann 2002; Davies and Brown 2001) have revealed that the orography has to be reasonably well resolved in the applied resolution to achieve correct behavior of the flow.

Therefore, Doms (2011) suggests a weak filtering of the orography to improve the

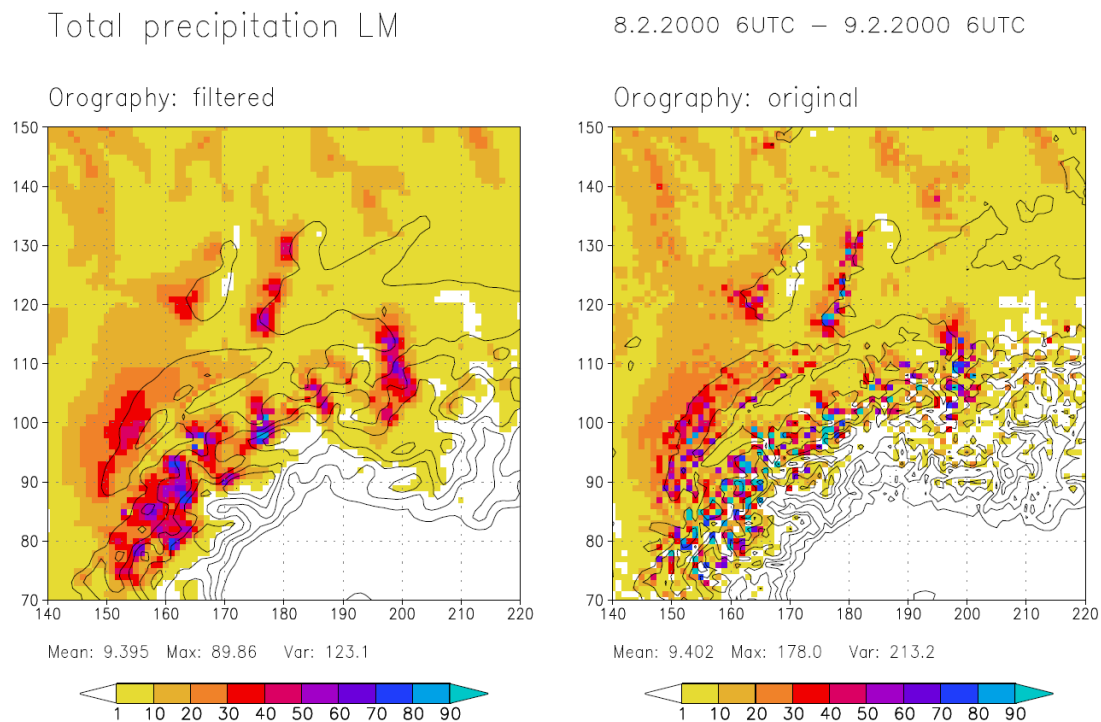


Fig. 3.2 Differences in the precipitation distribution of a COSMO simulation with filtered (left) and unfiltered orography (right) over the European Alps. Shown are 24 h precipitation sums from simulations of February 8 2000, 00 UTC (Doms 2011).

interaction of the dynamics with the surface. For this purpose a 10th-order Raymond (1988) filter is applied (with a filter constant $\epsilon = 0.1$). This almost completely removes $2\Delta x$ and $3\Delta x$ waves and leaves the remaining components nearly unchanged.

An example for the large impact of such a filtering on the simulation of precipitation can be seen in Figure 3.2. The simulation with the unfiltered orography shows a very noisy spatial precipitation pattern with strong horizontal precipitation gradients. In the filtered simulation the patterns are much smoother while the large-scale patterns and the domain-wide average precipitation are conserved. However, the precipitation maximum and the spatial variance are reduced by a factor of approximately 2 (Doms 2011).

3.1.3 Physics

In this Subsection the implementation of physical subgrid-scale processes via parameterizations is discussed. The outcome of parameterization schemes are directly used in the model equations, for instance, via the mixing terms M , the sources and sinks of the

cloud microphysics S^l , the precipitation fluxes $P_{l,f}$, or to the radiative heating term Q_T (cf., Equations 3.1 to 3.8).

3.1.3.1 Subgrid-Scale Turbulence

Subgrid-scale turbulence parameterizations link the explicitly resolved atmospheric motions with the unresolved fluctuating scales of motion. The representation of turbulent fluxes in an atmospheric model is important because they lead to an exchange of momentum, humidity, and heat between the surface and the free atmosphere.

The default subgrid-scale turbulence scheme of the CCLM uses a second-order closure suggested by Mellor and Yamada (1974) and Mellor and Yamada (1982). The scheme is based on prognostic turbulent kinetic energy (TKE) and is formulated in terms of liquid water potential temperature and total water content. It includes effects from thermal circulations and subgrid-scale condensation (Doms et al. 2011).

Optional, a three-dimensional TKE-based scheme is implemented in the CCLM which should be used in highly resolved simulations to avoid common approximations of boundary layer processes. The scheme was designed for large eddy simulations and is based on a model described in Herzog et al. (2002a); Herzog et al. (2002b). However, at the moment this scheme does not consider cloud water.

3.1.3.2 Surface Layer Parameterization

Surface fluxes of moisture, heat, and momentum can have large impacts on the results of numerical models. Fluxes like these are coupling the atmosphere with the surface model. In CCLM modified Businger relations (Businger et al. 1971) are used for the stability and roughness-length dependent surface flux formulation (Doms et al. 2011). For the flux calculation a computational efficient analytic procedure based on the work of Louse (1979) is applied.

Optional in the CCLM is a TKE-based surface transfer scheme which is related to the subgrid-scale turbulence TKE scheme mentioned above. Thereby, the surface layer is the layer between the lowest model level and the earths surface. This layer is divided in three parts: a laminar-turbulent sublayer, a roughness layer, and a constant-flux or Prandtl layer (Doms et al. 2011).

3.1.3.3 Grid-Scale Clouds and Precipitation

The correct simulation of clouds and precipitation is essential for the water and energy cycle of the earth (cf., Section 2.5). The various microphysical processes which lead to

the formation of clouds and precipitation are highly dependent on and interact with the thermodynamic conditions in the atmosphere.

The standard parameterization scheme for grid-scale clouds and precipitation is based on Kessler-type¹ bulk formulation and clusters cloud and precipitation particles into specified categories of water substances. Those categorized particles interact with the microphysical processes which themselves have feedbacks to the thermodynamic of the atmosphere (Doms et al. 2011). The scheme was developed for meso- β - and meso- α -scale simulations and accounts for stratiform mixed-phase clouds.

Beside water vapor three different categories of water are used in the basic scheme:

- *cloud water* q^c are particles which have a radius smaller than 50 μm and therefore no relative fall speed compared to the airflow.
- *Rain water* q^r consist of spherical droplets which have a non-negligible fall velocity. The distribution of the droplet size is derived from an exponential Marshall-Palmer size-distribution. The terminal velocity of the drops is purely dependent on the drop diameter.
- *Snow* q^s particles are treated as thin plates with a size proportional to the mass of the particles. The terminal velocity is only dependent on the particle size which is derived from a Gunn-Marshall size-distribution.

In the specific water content (q_{spec}) budget equation (including mass fraction of water vapor (q^v), cloud water (q^c), cloud ice (q^i), and graupel (q^g), depending on the used scheme) advective and turbulent processes are taken into account while rain water (q^r) and snow (q^s) is only advective transported.

In Figure 3.3 the microphysical processes in the CCLM standard scheme are depicted. The microphysical source/sink terms S enable the mass-transfers between the different water categories.

Beside the above described basic scheme there are three more cloud precipitation schemes implemented in CCLM (Doms et al. 2011) (namelist-switch `itype_gscp`):

1. The *warm rain scheme* is adapted from the Kessler (1969) scheme and has no ice face processes.
2. The *one-category ice scheme* is the above described basic scheme for applications on the meso- β - and meso- α -scale.
3. The *cloud ice scheme* is an extension of the standard scheme and includes additionally prognostic cloud ice and the corresponding source/sink terms. It is the default scheme in CCLM.

¹Kessler (1969) suggested a simple parameterization which relates the autoconversion rate to the cloud liquid water content linearly. Because of its simplicity this parameterization is widely used in cloud-related modeling studies.

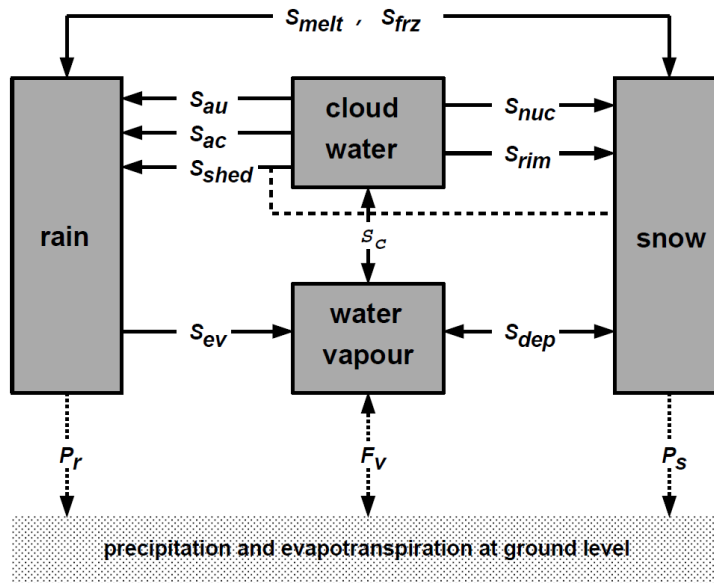


Fig. 3.3 Hydrological cycle in the standard CCLM cloud and precipitation scheme. The following symbols are used: autoconversion rate S_{au} , accretion rate S_{ac} , evaporation rate S_{ev} , rate of cloud water condensation and evaporation S_c , precipitation flux of rainwater/snow due to gravitational sedimentation of raindrops/snowflakes P_r/P_s , evaporation rate of rainwater in subcloud layers S_{ev} , increase of rainwater with time due to autoconversion S_{au} , rate of the initial formation of snow due to nucleation and subsequent diffusional growth of pristine ice crystals S_{nuc} , rate of change of snow mass fraction resulting from diffusion growth of snow particles S_{dep} , riming rate S_{rim} , melting rate of snow to form rain S_{melt} , freezing rate of rain to form snow S_{frz} , and rate at which water is shed by melting wet snow particles collecting cloud droplets to produce rain S_{shed} (Doms et al. 2011).

4. The *graupel-scheme* was designed for a more accurate representation of deep convective clouds and should be used in convection permitting simulations (see Figure 3.4).

3.1.3.4 Moist Convection Parameterization

Explicitly resolving cumulus convection demands for horizontal grid spacings smaller approximately 4 km (e.g., Weisman et al. 1997). This means in coarser resolved simulations deep convection is a subgrid-scale process and has to be parameterized. It turned out that even on low meso- γ -scales a parameterization for shallow convection is necessary.

In CCLM there are three moist convection parameterizations options:

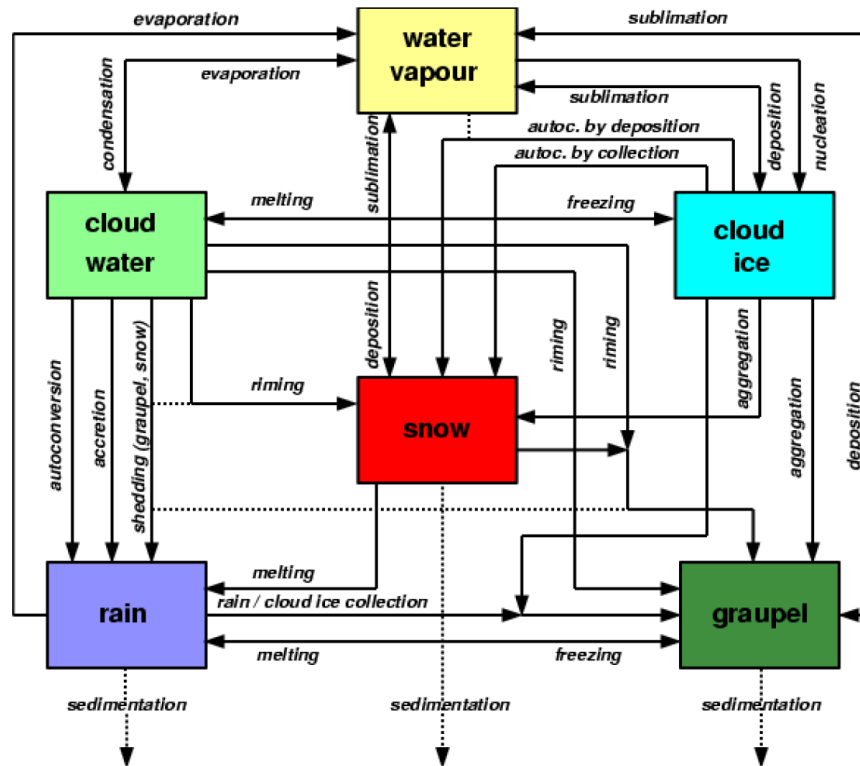


Fig. 3.4 Hydrological cycle in the graupel scheme of CCLM (Reinhardt and Seifert 2006).

1. The *mass flux Tiedtke scheme* is based on the work of Tiedtke (1989). It is the default scheme in CCLM and will be described in more detail below.
2. The *Kain-Fritsch scheme* proposed by Kain and Fritsch (1993) is not fully implemented and therefore not recommended for usage.
3. A *shallow convection scheme* extracted from the Tiedtke scheme is recommended for convection permitting simulations.

To give an example how a convection parameterization scheme is working the basics of the widely used Tiedtke mass flux scheme (Tiedtke 1989) are explained below. In the Tiedtke scheme three classes of moist convection are distinguished: shallow convection, penetrative convection, and mid-level convection. The first two have their roots in the planetary boundary layer (PBL) but have a different vertical extend in the atmosphere. In contrast mid-level convection originates in the free atmosphere. In the Tiedtke scheme only one type of convection can occur in one grid-cell at a time.

The first step in the scheme is to calculate vertical mass fluxes at the cloud base

which is derived from the grid-scale variables T , specific humidity (q), saturation vapor pressure (q_{sat}), and dry static energy (s) ($s = c_p T + gz$). For shallow and penetrative convection this mass flux is proportional to the integrated moisture convergence from the surface to the cloud base. For mid-level convection it is proportional to the vertical velocity w in the grid-cell.

A simple stationary cloud model is then used to calculate the vertical redistribution of heat, moisture, and momentum for the up- and downdrafts from the previously calculated mass flux at cloud base. This is then used to calculate the feedbacks of subgrid-scale vertical circulation on the resolved scales.

The downdrafts originate at the level of free sinking² and the mass-flux therein is proportional to the updraft mass-flux at the cloud base. The disposable proportionality factor is controlling the intensity of the downdraft (currently set to a fixed value of 0.3 in CCLM).

For precipitation, evaporation at sub-saturated levels below the cloud base is implemented. Precipitation reaches the ground as convective rain or snow dependent on the temperature in the lowest model level.

To be computationally more efficient the Tiedtke scheme does not have to be called every time-step (by default it is called every 10th timestep). Convection tendencies stay constant between two calls of the scheme.

3.1.3.5 Subgrid-Scale Clouds

In the grid-scale clouds and precipitation scheme (see Subsection 3.1.3.3) cloudiness is only dependent on the presence of cloud water (q^c) (Doms et al. 2011). Therefore, a grid-box is either totally filled with clouds if $q^c > 0$ (relative humidity = 100 %) or cloud free if $q^c = 0$ meaning that the cloud area fraction is either 0 or 1.

However, even if the relative humidity in a grid-box is below 100 % there can be subgrid-scale clouds which influence the radiative transfer in the atmosphere. Therefore, in the CCLM a fractional cloud cover (σ_c) is defined in each grid-box which is empirically dependent on the relative humidity, the height of the layer, and the convective activity. This scheme also cares for temperature inversions at the cloud tops to account for anvils with an increase of σ_c .

²The level of free sinking is assumed to be the highest model level where negative buoyancy of a mixture of equal parts of cloud air and saturated environmental air at wet-bulb temperature occurs compared to the environment (Doms et al. 2011).

3.1.3.6 Radiation

With the radiation transfer scheme the heating rate due to radiation is parameterized within atmospheric models. For this purpose the Ritter and Geleyn (1992) radiative transfer scheme, referred to as RG92, is used in CCLM. It accounts for five longwave (thermal) and three shortwave (solar) spectral intervals. Radiation in the RG92 scheme interacts with cloud water droplets, cloud ice crystals, water vapor, ozone, and takes into account effects of Rayleigh scattering. The graupel produced by the graupel-microphysics-scheme and the snow is not interacting with radiation in the RG92 scheme.

Within the scheme also partial cloudiness (produced by the sub-grid cloud scheme; see Subsection 3.1.3.5) is considered by attributing two sets of optical properties and fluxes to each layer, one for the cloudy and one for the cloud free part (Geleyn and Hollingsworth 1979). Thereby, clouds in adjacent model layers have maximum overlap while clouds which are separated by cloud free layers are independent from each other (random overlap assumption).

The RG92 radiation-transfer scheme is computationally expensive. Therefore, it is usually called hourly in meso- β -scale simulations (Doms et al. 2011). For the intermediate time steps the short and longwave heating rates stay constant. In highly resolved simulations the calling frequency can be increased to get an improved interaction with the cloud field. It is also possible to operate the scheme on a coarser grid to save computational resources.

3.1.3.7 Sub-Grid-Scale Orography

Small-scale orographic features cannot be resolved directly in state-of-the-art climate simulations. However, they are important for atmospheric dynamics and not accounting for those features can lead to an underestimation of surface drag. This can cause too weak cross-isobaric flow in the PBL, biases in the surface pressure (in the order of 1 hPa to 2 hPa), and an overestimation of wind speed by approximately 1 m s^{-1} throughout the troposphere (Doms 2011).

To reduce these impacts a sub-grid-scale orography scheme (SSO) was implemented in CCLM which is based on the work of Lott and Miller (1997). Within that scheme the low-level flow is blocked when the subgrid-scale orography is sufficiently high. The upper part of the low-level flow produces gravity waves when flowing over the orography.

3.1.3.8 Soil Processes

The coupling of the atmospheric model with the surface is done via fluxes which are dependent on stability and roughness-length. To calculate those fluxes the ground temperature and specific humidity has to be known. These two parameters are predicted by the surface model which consists of a separate set of equations for thermal and hydrological processes within the soil (Doms et al. 2011). In CCLM vegetation is calculated explicitly which leads to additional exchanges between plants, soil, and air.

The default soil model in CCLM is TERRA wherein the ground temperature is calculated in a two-layer model according to Jacobsen and Heise (1982). The Richardson equation (Richards 1931) is used to calculate the soil water content for two or three layers. Transpiration of plants and evaporation from land surface are functions of water content and transpiration from soil and additionally depend on the ambient temperature and radiation.

Many parameters in TERRA depend on the soil texture (sand, sandy loam, loam, loamy clay, and clay) (Doms et al. 2011). Additionally three soil types are specified (peat, ice, and rock) whereby no hydrological processes are considered for the last two. Generally, TERRA is called at all grid points with a land surface fraction of more than 50%. For the sea grid points the surface temperature has to be provided by the driving model.

Optionally, a multi-layer version of TERRA can be used which includes freezing/melting of soil water/ice, a different process of snow melting, and time dependent snow albedo. In the multi-layer approach the soil type does not depend on the layer thickness and the structures of the layers are the same in the thermal and hydrological part of the model (Doms et al. 2011).

3.1.3.9 Initial and Boundary Data

To start and run the model five different groups of data are necessary (Schättler 2012):

- external parameters for the surface,
- external parameters for plants, ozone, and aerosols
- initial soil and surface variables
- initial atmospheric variables, and
- boundary data.

Constant External Parameters for the Surface External parameters are needed to provide CCLM information about the lower boundaries and are typically stored in an

3 Dynamical Downscaling and Detecting Added Value

external parameter file. The fields are two dimensional and have to cover the entire computational domain.

In Table 3.1 those external parameters are listed which have to be provided to CCLM in any case.

Tab. 3.1 Constant external parameters for the surface (Schättler 2012).

Name	Description
HSURF	Height of surface topography
FIS	(alternatively) geopotential of surface
FR_LAND	Fraction of land in the grid-cell
SOILTYP	Soil type of the land (varies from 0 to 9)
Z0	Roughness length

If the SSO scheme is used four additional two dimensional fields (listed in Table 3.2) have to be provided to the model.

Tab. 3.2 Constant external parameters for the SSO scheme (Schättler 2012).

Name	Description
SSO_STDH	standard deviation of sub-grid-scale orography [m]
SSO_GAMMA	anisotropy of the orography [-]
SSO_THETA	angle between the principal axis of orography and east [rad]
SSO_SIGMA	mean slope of sub-grid-scale orography [-]

Since the lake model demands for the location and the depth of lakes (see Table 3.3) those two fields have to be provided if the lake model is applied.

Tab. 3.3 Constant external parameters for lakes (Schättler 2012).

Name	Description
FR_LAKE	lake fraction in a grid element [0,1]
DEPTH_LK	lake depth [m]

In Table 3.4 additional optional external parameter fields for the surface are listed. They include fields for the minimum stomata resistance of plants, surface emissivity, and ground fraction covered by forests.

3.1 Dynamical Downscaling with RCMs on the Example of CCLM

Tab. 3.4 Other constant external parameters (Schättler 2012).

Name	Description
PRS_MIN	minimum stomata resistance of plants
EMIS_RAD	thermal radiative surface emissivity
FOR_E	ground fraction covered by evergreen forest
FOR_D	ground fraction covered by deciduous forest

External Parameters for Plant Characteristics, Ozone Contents and Aerosol Types

Here external parameters are discussed which are not constant for the simulation period and therefore are updated with the boundary conditions. The fields mentioned in Table 3.5 are describing the plants in CCLM.

Tab. 3.5 Plant characteristics (Schättler 2012).

Name	Description
PLCOV_MX	plant cover dataset for vegetation time
PLCOV_MN	plant cover dataset for time of rest
PLCOV12	12 monthly climatological mean values for plant cover
LAI_MX	leaf area index dataset for vegetation time
LAI_MN	leaf area index dataset for time of rest
LAI12	12 monthly climatological mean values for leaf area index
ROOTDP	root depth
NDVI_MRAT	ratio of monthly mean normalized differential vegetation index to annual maximum for 12 months

Additionally to the plant fields information about the amount and distribution of ozone has to be provided (see Table 3.6).

Tab. 3.6 Ozone contents (Schättler 2012).

Name	Description
VIO3	Vertical integrated ozone content
HMO3	Ozone maximum

By default aerosols in CCLM are treated as constant for different land-surface types. It is, however, also possible to read in a monthly aerosol climatology (see Table 3.7).

Tab. 3.7 Aerosol characteristics (Schättler 2012).

Name	Description
AER_SO4	(Tegen et al. 1997) aerosol type sulfate drops
AER_DUST	(Tegen et al. 1997) aerosol type mineral dust
AER_ORG	(Tegen et al. 1997) aerosol type organic
AER_BC	(Tegen et al. 1997) aerosol type black carbon
AER_SS	(Tegen et al. 1997) aerosol type sea salt

Initial Soil and Surface Variables Additionally to external parameters also initial data are needed to run CCLM. Mandatory surface variables are shown in Table 3.8.

Tab. 3.8 Necessary surface variables (Schättler 2012).

Name	Description
T_SNOW	Temperature of snow surface
W_SNOW	Water content of snow
WI	Water content of interception water
QV_S	Specific water vapor content at the surface
TS	Temperature of surface

Also soil variables have to be provided to run CCLM. By the default the multi-layer soil model is used which demands the fields listed in Table 3.9.

Tab. 3.9 Necessary soil variables (for multi-layer soil model) (Schättler 2012).

Name	Description
T_SO	Temperature of (multi-layer) soil levels
W_SO	Water content of (multi-layer) soil levels
FRESHSNW	Indicator for freshness of snow
RHO_SNOW	Prognostic snow density

Initial Atmospheric Variables Finally also the atmospheric variables which are listed in Table 3.10 have to be provided as initial conditions to CCLM.

Tab. 3.10 Necessary atmospheric variables (Schättler 2012).

Name	Description
Necessary atmospheric variables	
U	Zonal wind speed
V	Meridional wind speed
W	Vertical wind speed (defined on half levels)
T	Temperature
PP	Pressure deviation from a reference pressure
QV	Specific water vapor content
QC	Specific cloud water content
QI	Specific cloud ice content
QR	Specific rain content
QS	Specific snow content
QG	Specific graupel content

Many external parameters like the land-sea mask, topography, and vegetation variables are taken from a dataset which is provided by Deutscher Wetterdienst (DWD) (Doms et al. 2011). Therein the GTOPO30 dataset is used to derive the orography and land-sea mask. GTOPO30 is provided by the U.S. Geological Service (see <http://edcdaac.usgs.gov/gtopo30/gtopo30.asp>). The land-cover is taken either from the Global Land Cover Characteristics (GLCC) (see <http://edcdaac.usgs.gov/glcc/glcc.asp>) or the Coordination of Information on the Environment (CORINE) (see <http://www.epa.ie/whatwedo/assessment/land/corine/>) dataset. Soil-types are provided by the Digital Soil Map of the World (DSMW) (see <http://www.fao.org/ag/agl/agll/dsmw.HTM>). The PrEProcessor (PEP) tool (Smiatek et al. 2008) can be used to derive the data for the region of interest.

Boundary Data Additionally to the initial data which determine the initial conditions of a simulation also boundary data have to be provided to CCLM. The boundary data consist of the atmospheric variables specified in Table 3.10, the necessary surface variables from Table 3.9, and optionally variables concerning the plant characteristics (Table 3.11), surface temperature (TS in Table 3.8), ozone properties (Table 3.6), and aerosol types (Table 3.7).

Tab. 3.11 Optional plant characteristics boundary conditions (Schättler 2012).

Name	Description
PLCOV	plant cover
LAI	leaf area index
ROOTDP	root depth

3.2 Searching and Detecting Added Value

It is often not straightforward to search and detecting added value in convection permitting climate simulations (CPCSs). Compared to coarser gridded simulations, one of the benefits of CPCSs is that they are able to resolve smaller scale features. Therefore, it is intuitive to search for added value in those scales which are not, or only badly, resolved in their coarser gridded counterparts. However, in the atmosphere energy is transferred from small to large scales and vice versa. This means added value in convection permitting simulations (CPCSs) can potentially also be found in the large e.g., synoptic-scale.

An important topic when simulations with different horizontal grid-spacings are evaluated is the horizontal scale on which the simulations are compared. There are statistical methods, introduced further down in this section, which enable to evaluate scale independent or derive metrics on different scales. However, many traditional statistical methods demand for a common grid on which the simulated and observed fields have to be regridded. But, which grid should be used as common one? One approach would be to always evaluate on the coarsest given grid. This might be necessary because a coarse gridded simulation, even if it is perfect on it's scale, get's penalized if it is evaluated on smaller grids. However, this also means that all the fine-scale features in the highly resolved simulation are smoothed out and cannot longer be evaluated. To overcome this problem the simulations can be regridded to the scale of the observation dataset which should then have at least a similar resolution as the simulation with the smallest grid-spacing. Detected added value with this approach however, would not necessarily imply that the coarser-scale simulations are performing worse (they might be even perfect on their resolved-scale), but it would still demonstrate additional useful information in the finer scale simulations of CPCSs.

Large parts of the upcoming sections are similar to, or taken from Prein and Gobiet (2011). Readers who are interested in a even larger variety of evaluation methods which are suitable to detect added value in CPCSs or a more complete illustration of the presented methods are reverred to Prein and Gobiet (2011).

3.2.1 Mean Climate

In the atmosphere energy and mass is transferred from large-scales to smaller ones and vice versa. Thereby, meso-scale features can upscale and affect large-scales (e.g., the synoptic-scale) significantly especially in areas with complex terrain or coastlines. Typically, only in presence of time invariant meso-scale features, like the two mentioned before, added value in climatologic mean values is detectable in CPCSs. One example for such an added value is the improvement in the spatial patterns of precipitation through the shadowing effect of mountain ranges.

Typical methods to detect added values in climatological average fields are bias maps, spatial correlation coefficients, or annual cycles.

3.2.1.1 Bias Maps

Biases are systematic errors which can be calculated by subtracting observed values at a given time or time span from simulated values. For deriving a map this has to be done point-wise on a common grid:

$$\text{bm}_{ij} = \frac{1}{N} \sum_{t=1}^n (x_{ijt} - o_{ijt}). \quad (3.11)$$

Thereby, the simulated field (x_{ijt}) and the observed field (o_{ijt}) have to be given for common times t , common longitudes i , and latitudes j . Thereby $t = 1, \dots, n$ and the total N , over which is averaged, has to be long enough to capture natural variability (30 years are often used) to derive a meaningful climatological bias of the simulation. It is advisable to draw bias maps not only on annual basis but also on seasonal, because error characteristics in climate models are often varying seasonally (see also Subsection 3.2.1.3).

3.2.1.2 Spatial Correlation

The correlation coefficient (r_{xo}) is a measure of linear connection between two variables and is defined as the standardized covariance (cov_{xo}):

$$\begin{aligned} r_{xo} &= \frac{\text{COV}_{xo}}{\sigma_x \cdot \sigma_o} \\ \text{COV}_{xo} &= \frac{\sum_{i=1}^N (x_i - \bar{x}) \cdot (o_i - \bar{o})}{N} \\ \sigma_x &= \sqrt{\frac{\sum_{i=1}^N (x_i - \bar{x})^2}{N}} \\ \sigma_o &= \sqrt{\frac{\sum_{i=1}^N (o_i - \bar{o})^2}{N}} \\ r_{xo} &= \frac{\sum_{i=1}^N (x_i - \bar{x}) \cdot (o_i - \bar{o})}{N \cdot \sigma_x \cdot \sigma_o}. \end{aligned} \quad (3.12)$$

Thereby σ_x and σ_o are the standard deviations of the simulated field x_{ijt} and observed field o_{ijt} . In Equation 3.12, a bar above a variable means averaging. A useful tool to

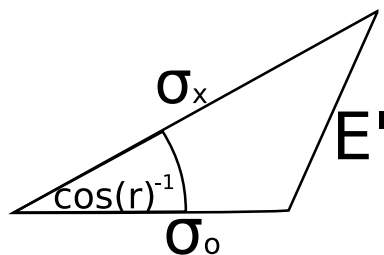


Fig. 3.5 Geometrical relationship between r_{xo} , E' , and σ_o and σ_x .

displaying and compare correlation coefficients together with the pattern root-mean-squared-errors (E' s), σ_o , and σ_x is the Taylor diagram (Taylor 2001). The mathematical formulation of E' is:

$$E^2 = \bar{E}^2 + E'^2$$

$$\bar{E} = \bar{x} - \bar{o}$$

$$E' = \left\{ \frac{1}{N} \sum_{k=1}^N [(x_k - \bar{x}) - (o_k - \bar{o})]^2 \right\}^{1/2} \tag{3.13}$$

$$E'^2 = \sigma_x^2 + \sigma_o^2 - 2\sigma_x\sigma_o r. \tag{3.14}$$

Hereby, the root-mean-squared-error (E^2) is the sum of the squared average bias (\bar{E}^2) and the squared E' (E'^2). Equation 3.14 can be geometrically interpreted by using the law of cosines $c^2 = a^2 + b^2 - 2ab \cos \phi$ where a , b , and c are the sides of a triangle, and ϕ is the angle opposite of c . The geometrical relationship of r_{xo} , E' , σ_x , and σ_o is displayed in Figure 3.5.

3.2.1.3 Annual Cycle

The annual cycle is a basic pattern of climate which is caused by the changing orbital position of the earth during the course of a year. Thereby, atmospheric parameters are influenced by the orbital position either directly by the variation of incoming solar radiation or indirectly by changes in the synoptic circulation (e.g., monsoon systems, strength of westerlies). Climate models typically have different error characteristics during different seasons because of the changing atmospheric and surface processes. A good example is the predominance of convective precipitation in mid-latitude summers and the mostly frontal precipitation during winters.

Looking at biases in the annual cycle can reveal insights in weaknesses of the representation of physical processes within a climate model. Thereby, data are typically

spatially and temporally averaged for each month of the year. The biases between the simulated minus the reference values can then be displayed as a time line representing the average monthly climatologically situation over a specific area.

3.2.2 Spatiotemporal High Resolution

Detecting added value of CPCs in climate mean fields is often problematic because temporal and/or spatial averaging tends to cancel out improvements on small spatial scales (except those which are triggered by meso-scale time invariant features like orography; see Subsection 3.2.1). Therefore, statistical methods are needed which are capable to investigate spatiotemporal highly resolved fields. Beside those methods also reliable high-resolution gridded observation datasets are needed for evaluations on fine scales. However, reliable sub-daily observations on kilometer-scale grids are often not available.

In most cases traditional statistical methods, like those discussed in Subsection 3.2.1, can also be applied to spatiotemporally, highly resolved fields. However, there are some atmospheric parameters like precipitation, global radiation, or cloud cover which demand for special evaluation methods because spatial and temporal highly resolved fields of those parameters are discontinues and highly variable.

For example, a typical summertime mid-latitude precipitation field can have large areas with non-precipitation and small areas with precipitation. Thereby, the transition between no precipitation to precipitation can be very sharp. Furthermore, the generation of e.g., intermittent summertime convective precipitation is a highly non-linear, stochastic process. This means, even a perfect model would probably not be able to simulate intermittent convective precipitation at the exactly same time and location where it is observed. Even when the model is able to capture the larger scale precipitation patterns well, errors on the small-scale dominate the total error (e.g., Mass et al. 2002). In general, small misplacements cannot be avoided because upscale error propagation leads to a decreasing predictability limit toward small scales (1 km – 100 km) (Wernli et al. 2008). This means small spatial or temporal shifts between observed and simulated precipitation should not be considered as model errors but are unavoidable in intermittent convective precipitation producing systems.

If traditional statistical metrics like correlation coefficients, or root-mean-square-errors (RMSEs) are used to evaluate the skill of simulations in high spatiotemporal resolution the so called *double penalty problem* occurs. This means a small shift in the simulated precipitation field is penalized twice: first because there is precipitation observed where non is simulated and second because there is precipitation simulated where non is observed. Considering the double penalty problem is especially important for CPCs because the higher the horizontal grid-spacing of a simulation the finer the locations of precipitation objects are defined. For example, detectable displacements in a simulation

with 50 km horizontal grid-spacing can only be larger than 50 km whereas in a CPSs displacements can be smaller than approximately 3 km.

Multiple approaches have been developed (especially within the numerical weather prediction (NWP) community) to overcome the double penalty problem. Those methods do not require a perfect fit of the simulation and the observation at the fine-scale. In the following subsections an overview of commonly used methods is given. Methods which are applied in Chapter 4 are explained in detail while others are briefly introduced.

3.2.2.1 Filtering Approaches

The common feature of filtering methods is that they separate the spatial structures in different scales and compare them with the observation. Thereby, filtering approaches can further be separated in neighborhood methods and scale separation methods.

Neighborhood Methods Neighborhood or fuzzy verification methods give credits to simulated events which are close to the observation. Ebert (2008) provides a good overview of 10 fuzzy verification methods which are used in the verification of numerical weather predictions. A similar study was done by Ament et al. (2008) who found 3 fuzzy verification methods out of 12 which have an outstanding performance in detecting a broad range of forecast errors:

- fractions skill score (FSS) (Roberts and Lean 2008),
- Upscaling (Zepeda-Arce et al. 2000), and
- Intensity-Scale (Casati et al. 2004).

Those three methods are in detail discussed in the following paragraphs. For the sake of completeness seven additional methods are mentioned with their references below:

- Minimum coverage (Damrath 2004),
- Fuzzy logic, joint probability (Damrath 2004),
- Multi-event contingency table (Atger 2001),
- Pragmatic approach (Theis et al. 2005),
- Practical perfect hindcast (Brooks et al. 1998),
- Conditional square root for ranked probability score (Germann and Zawadzki 2004), and
- Areal-related RMSE (Rezacova et al. 2007).

Fractional Skill Score Roberts and Lean (2008) developed a verification method which investigates how the skill of a simulation varies with spatial scale. The basic idea behind

the FSS is that a simulation is useful if the spatial frequency of events is similar in the forecast and in the observation. The precondition for using this method is that the observation and the simulation are given on the same grid. In the first step, the originally observed and simulated fields are transferred to observed binary fields (I_o) and simulated binary fields (I_x) by choosing a set of precipitation thresholds (qs) (e.g., $q = 0.5 \text{ mm d}^{-1}$, 1 mm d^{-1} , 2 mm d^{-1} , and 4 mm d^{-1}) and setting all gridcells exceeding the threshold to 1 and all others to 0,

$$I_o = \begin{cases} 1 & o \geq q \\ 0 & o < q \end{cases} \quad \text{and} \quad I_x = \begin{cases} 1 & x \geq q \\ 0 & x < q. \end{cases}$$

Second, for all grid-points in the binary fields the spatial density of ones compared to zeros is calculated for a given squared neighborhood of length n :

$$\begin{aligned} O_{(n)}(i, j) &= \frac{1}{n^2} \sum_{k=1}^n \sum_{l=1}^n I_O \left[i + k - 1 - \frac{(n-1)}{2}, j + l - 1 - \frac{(n-1)}{2} \right], \\ X_{(n)}(i, j) &= \frac{1}{n^2} \sum_{k=1}^n \sum_{l=1}^n I_X \left[i + k - 1 - \frac{(n-1)}{2}, j + l - 1 - \frac{(n-1)}{2} \right]. \end{aligned} \quad (3.15)$$

In Equation 3.15 the field of observed fractions ($O_n(i, j)$) and field of simulated fractions ($X_n(i, j)$) contain the fractions of values exceeding the threshold for a square of length n . Thereby, $i = 1, \dots, N_x$ and $j = 1, \dots, N_y$, where N_x corresponds to the numbers of columns in the domain and N_y to the number of rows. The fractional fields $O_n(i, j)$ and $X_n(i, j)$ are generated for different spatial scales by changing the value of n from $n = 1, \dots, 2N - 1$, whereby $N = \max(N_x, N_y)$. If neighborhood points lie outside the domain, their value is assumed as zero.

After $O_n(i, j)$ and $X_n(i, j)$ are derived, the third step is to calculate fraction skill scores. Therefore, the mean squared error (MSE) is calculated:

$$\begin{aligned} \text{MSE}_{(n)} &= \frac{1}{N_x N_y} \sum_{i=1}^{N_x} \sum_{j=1}^{N_y} [O_{(n)i,j} - X_{(n)i,j}]^2, \\ \text{MSE}_{(n)\text{ref}} &= \frac{1}{N_x N_y} \left[\sum_{i=1}^{N_x} \sum_{j=1}^{N_y} O_{(n)i,j}^2 + \sum_{i=1}^{N_x} \sum_{j=1}^{N_y} X_{(n)i,j}^2 \right]. \end{aligned} \quad (3.16)$$

From Equation 3.16 the FSS can be calculated as an MSE skill score:

$$\text{FSS}_{(n)} = \frac{\text{MSE}_{(n)} - \text{MSE}_{(n)\text{ref}}}{\text{MSE}_{(n)\text{perfect}} - \text{MSE}_{(n)\text{ref}}} = 1 - \frac{\text{MSE}_{(n)}}{\text{MSE}_{(n)\text{ref}}}. \quad (3.17)$$

$\text{MSE}_{(n)\text{perfect}}$ is the MSE of a perfect simulation and therefore 0 for a given neighborhood length n . $\text{MSE}_{(n)\text{ref}}$ is the largest obtainable MSE from the given simulation and reference dataset. This means an FSS of 1 indicates the best possible simulation.

Upscaling The upscaling verification method was first published by Zepeda-Arce et al. (2000) and is conceptually built on the assumption that a useful simulation resembles the observation when averaged to a coarser scale. In the upscaling method the threat score (TS) is calculated as a measure of scale. The TS compares the area of precipitation above a threshold between a simulation and an observation (e.g., see Wilks 2005) and is defined as:

$$\text{TS} = \frac{A_c}{A_o + A_x - A_c}, \quad (3.18)$$

thereby, A_c is the area where the simulation correctly produced precipitation above the threshold, A_o is the total observed area, and A_x the total simulated area. The best possible TS is one whereas the worst is zero. The TS is scale-dependent and gets typically higher with increasing scale. Furthermore, the TS can be expressed as a function of spatial scale and precipitation intensity by regriding the simulated and observed fields on grids with different spacings and by using different precipitation thresholds.

Intensity-Scale Casati et al. (2004) used a method which gives credits to a simulation which has more accurate structures than a random arrangement of the observation. As a first step, simulated and observed data have to be preprocessed. Therefore, all non-zero precipitation values are dithered by adding uniformly distributed noise with a magnitude of $\pm 1/64 \text{ mm h}^{-1}$. Thereafter, the precipitation values are normalized with a (base 2) logarithmic transformation and the pixels with zero precipitation are set to -6 . The normalization is necessary to produce more normally distributed data and to remove skewness. These data are then recalibrated with the following transformation function:

$$X' = F_O^{-1}(F_X(X)), \quad (3.19)$$

where each value of the simulated field X is substituted with the value of the observed field O having the same empirical cumulative probability F_O and F_X . With this procedure biases in the marginal distribution of the simulated precipitation are erased.

After the preprocessing the simulated and observed fields are converted into a binary fields using thresholds $q = 0 \text{ mm h}^{-1}, 1/32 \text{ mm h}^{-1}, 1/16 \text{ mm h}^{-1}, \dots, 128 \text{ mm h}^{-1}$:

$$I_O = \begin{cases} 1 & O > q \\ 0 & O \leq q \end{cases}$$

and

$$I_{X'} = \begin{cases} 1 & X' \geq q \\ 0 & X' < q. \end{cases}$$

Then the binary error Z is calculated:

$$Z = I_{X'} - I_O. \quad (3.20)$$

With a two-dimensional discrete Haar wavelet decomposition the binary error can be expressed as the sum of components on different spatial scales:

$$Z = \sum_{l=1}^L Z_l, \quad (3.21)$$

where l is referring to the spatial scale of the error and not to the scales of the precipitation features or their displacements. A detailed description of the two dimensional Haar wavelet decomposition can, for example, be found in Mallat (1999) or Nievergelt (1999).

With the mean squared Z -values the MSE of the binary image is calculated:

$$\text{MSE} = \overline{Z^2}. \quad (3.22)$$

Since the components of a discrete wavelet transformation are orthogonal $\overline{Z_l Z_{l'}} = 0$ $l \neq l'$ the MSE can be written as:

$$\text{MSE} = \sum_{l=1}^L \sum_{l'=1}^L \overline{Z_l Z_{l'}} = \sum_{l=1}^L \overline{Z_l^2}$$

and (3.23)

$$\text{MSE} = \sum_{l=1}^L \text{MSE}_l,$$

where $\text{MSE}_l = \overline{Z_l^2}$. Thereby, MSE_l depends on the spatial scale l and the threshold u which enables the evaluation of precipitation on different scales and intensities. With the now obtained data the MSE skill score can be calculated for every scale and threshold:

$$SS = \frac{\text{MSE} - \text{MSE}_{random}}{\text{MSE}_{best} - \text{MSE}_{random}} = 1 - \frac{\text{MSE}}{2\varepsilon(1 - \varepsilon)}, \quad (3.24)$$

where $\text{MSE}_{best} = 0$ is a perfect simulation, $\text{MSE}_{random} = 2\varepsilon(1 - \varepsilon)$ is the MSE of a randomly created binary field and ε is the fraction of rain-pixels in the observation. By assuming that the random observed and simulated binary fields are Bernoulli distributed (Be) variables $I_X \sim \text{Be}(\varepsilon)$ and $I_O \sim \text{Be}(\varepsilon)$ which have (unbiased) means $E(I_{X'}) = E(I_O) = \varepsilon$ and variances $\sigma_{I_O}^2 = \sigma_{I_{X'}}^2 = \varepsilon(1 - \varepsilon)$ it can be shown that the binary error (Equation 3.20) has a mean $E(Z) = 0$ and a variance $\sigma_Z^2 = \sigma_{I_O}^2 + \sigma_{I_{X'}}^2 = 2\varepsilon(1 - \varepsilon)$. The expected value of MSE is then $\text{MSE}_{random} = E(Z^2) = E(Z - E(Z))^2 = \sigma_Z^2 = 2\varepsilon(1 - \varepsilon)$. With the assumption that the MSE is uniformly distributed over all scales SS can be written as the sum of its means over all scales by using Equation 3.23 and Equation 3.24:

$$SS_l = 1 - \frac{\text{MSE}_l}{2\varepsilon(1 - \varepsilon)/L}. \quad (3.25)$$

3.2.2.2 Scale Separation Methods

The goal of the here presented methods is to investigate performance as a function of spatial scale. Fourier or wavelet transformations are common tools to decompose atmospheric fields and to look at different scales separately.

The Discrete Cosine Transformation (DCT) Using Fourier transformation enables to decompose a periodic function into its wavenumbers of partial frequencies (Peixoto and Oort 1992). However, problems can occur if datasets with sharp boundaries (like RCM output) are standard Fourier transformed because of aliasing of large-scale variabilities into shorter scales.

A possible solution of this problem is the use of the discrete cosine transformation (DCT) method. Denis et al. (2002[a]) were the first who used the 2D DCT for limited areas. Therefore, the precipitation field has to be mirrored at the position $i = j = -1/2$ to make it symmetric. Thereafter, the Fourier transformation can be applied, centered on $i = j = -1/2$. This is a special case of a Fourier transformation which is called DCT because the sine components of the Fourier series are zero for symmetric functions. Concerning a two dimensional matrix (z_{ij}) of N_i by N_j grid-points, the direct and inverse DCT are defined as:

$$Z(m, n) = \beta(m)\beta(n) \sum_{i=0}^{i=N_i-1} \sum_{j=0}^{j=N_j-1} z(i, j) \cos \left[\pi m \frac{(i + 1/2)}{N_i} \right] \cos \left[\pi n \frac{(j + 1/2)}{N_j} \right] \quad (3.26)$$

$$z(i, j) = \sum_{m=0}^{m=N_i-1} \sum_{n=0}^{n=N_j-1} \beta(m)\beta(n) Z(m, n) \cos \left[\pi m \frac{(i + 1/2)}{N_i} \right] \cos \left[\pi n \frac{(j + 1/2)}{N_j} \right] \quad (3.27)$$

$$\beta(m) = \begin{cases} \sqrt{\frac{1}{N_i}}, & \text{for } m = 0 \\ \sqrt{\frac{2}{N_i}}, & \text{for } m = 1, 2, \dots, N_i - 1 \end{cases} \quad (3.28)$$

$$\beta(n) = \begin{cases} \sqrt{\frac{1}{N_j}}, & \text{for } n = 0 \\ \sqrt{\frac{2}{N_j}}, & \text{for } n = 1, 2, \dots, N_j - 1 \end{cases} \quad (3.29)$$

Thereby, z_{ij} is the value of the field at grid-point (i, j) , and the real spectral coefficient (Z_{mn}) corresponds to the 2D-wavenumber at (m, n) . In the next step the Z_{mn} is used to calculate spectral variances ($\sigma^2(m, n)$):

$$\sigma^2(m, n) = \frac{Z^2(n, m)}{N_i N_j} \quad (3.30)$$

To generate variance spectra of a 2D-field, the $\sigma^2(m, n)$ have to be connected to a specific wavelength. To do so, the method of *binning* was suggested by Denis et al. (2002[a]). It is based on dividing the wavenumber field into multiple quarters of ellipses. The space between two ellipses can be connected to a specific wavenumber for which the variances are summed up. For a more detailed description see Denis et al. (2002[a]). An application of this method to high resolved RCM output can be found in Kapper (2009) and Prein et al. (2013[b]).

Variogram and Correlograms The basic idea of evaluating fields with the variogram method is related to publications of Gebremichael and Krajewski (2004), Germann and Joss (2001), Harris et al. (2001), and Zepeda-Arce et al. (2000). Marzban and Sandgathe (2009) proposed this method to compare two fields in terms of their covariance structures.

In this thesis correlograms and variograms are used to compare spatial similarities and dissimilarities between observations and model output. Correlograms and variograms are frequently used in geostatistics to explore the spatial organization of different phenomena (e.g., Isaaks and Srivastava 1989). They illustrate how the correlation and variance depend on spatial scale. Therefore, spatial data $z(u)$ at the locations u and sample data pairs at different distances are taken. The distance between a given data pair is usually called the “lag” (plus/minus some lag tolerance (d); e.g., $d = 10\,000$ m). The lag vector (h) consists of I values where $i = 0, 1, 2, \dots, I$ and $h_i = h_{i-1} + 2d$. The lagged versions

of the data at locations $z(u)$ is $z(u+h)$. Defining number of pairs (N) separated by lag h (plus or minus d) the statistics for lag h can be computed as covariance:

$$C(h) = \frac{1}{N(h)} \sum_{\alpha=0}^{N(h)-1} z(u_\alpha) \cdot z(u_\alpha + h) - m_0 \cdot m_{+h}, \quad (3.31)$$

correlation,:

$$r(h) = \frac{C(h)}{\sqrt{\sigma_0 \cdot \sigma_{+h}}}, \quad (3.32)$$

and variance:

$$\sigma^2(h) = \left(\frac{1}{2N(h)} \sum_{\alpha=0}^{N(h)-1} [z(u_\alpha + h) - z(u_\alpha)]^2 \right) \cdot \frac{1}{2}. \quad (3.33)$$

In Equation 3.31 m_0 and m_{+h} denote the mean of the $z(u)$ and $z(u+h)$ values:

$$m_0 = \frac{1}{N(h)} \sum_{\alpha=0}^{N(h)-1} z(u_\alpha), \quad (3.34)$$

$$m_{+h} = \frac{1}{N(h)} \sum_{\alpha=0}^{N(h)-1} z(u_\alpha + h), \quad (3.35)$$

and σ_0 and σ_{+h} in Equation 3.32 are the corresponding standard deviations:

$$\sigma_0 = \frac{1}{N(h)} \sum_{\alpha=0}^{N(h)-1} [z(u_\alpha) - m_0], \quad (3.36)$$

$$\sigma_{+h} = \frac{1}{N(h)} \sum_{\alpha=0}^{N(h)-1} [z(u_\alpha + h) - m_{+h}]. \quad (3.37)$$

Once $r(h)$ and $\sigma^2(h)$ are calculated they can be plotted against h . The plots are then called correlograms and variograms. In correlograms similarities within a field are measured without accounting for magnitude differences while variograms give insight in dissimilarities and are sensitive to differences in magnitude.

Scale Dependent Analysis by Regridding A method to do scale-dependent analysis with observations from station data is proposed in Prein et al. (2013[b]). Thereby, the skill of simulated precipitation fields to accurately reproduce point measurements for different horizontal scales of precipitation systems is evaluated by resampling the data

to common grids with different grid-spacings. The grid spacings can range from the finest simulated grid to a grid which contains at least a couple of grid-points within the evaluation domain to retain some spatial variability.

With this method it is possible to investigate the upscaling effect of small-scale features, which are resolved in fine gridded simulation, to larger scales. The proposed resampling technique, does not use any interpolation and is able to spatially conserve precipitation amounts within a region (for details about the method see Suklitsch et al. (2008)). On each new grid, precipitation values are calculated at the locations of the observation station by inverse-distance average the simulated precipitation values at the four nearest grid-points around the station. Those values are then compared to the observed values to calculate the spatial Pearson correlation coefficient (CC), spatial standard deviations normalized by the standard deviation of the observations, and RMSE. The resampling approach enables the evaluation of the same spatial scales in simulations with different grid-spacings and makes it possible to conduct a quantitative analysis of the upscaling effect of small-scale features on larger scales.

Intensity-scale The intensity-scale method, published by Casati et al. (2004) was already introduced in Subsection 3.2.2.1. By using Haar wavelets, reference and simulated precipitation fields are separated in different scales which then are evaluated by an MSE skill score. Since the intensity-scale method uses spectral decomposition and skill scores on different scales and intensities it can be assigned to both, fuzzy and scale separation methods.

3.2.2.3 Displacement Approaches

Beside the above described filtering approaches, displacement approaches are the second category of methods which enable an evaluation of spatiotemporal highly resolved precipitation simulations. Displacement approach methods can be further categorized in feature based approaches and field deformation methods.

Feature Based Approaches The basic idea behind object based or feature based spatial verification methods is to identify relevant features in the simulated and observed fields and compare characteristic attributes of both fields with each other. The Structure-Amplitude-Location (SAL) method (Wernli et al. 2008) will be discussed below in detail while other relevant methods are just listed below with their reference.

- Cluster Analysis (Marzban and Sandgathe 2006),
- Method for Object-based Diagnostic Evaluation (MODE) (Davis et al. 2006),
- Contiguous Rain Area (CRA) (Ebert and McBride 2000), and

- Procrustes (Micheas et al. 2007).

SAL Verification Method Wernli et al. (2008) introduced an object-based quality measure which considers three components accounting for the Structure-Amplitude-Location (SAL) of a precipitation field. The SAL method aims to address the following issues:

- quantify the quality of a simulated precipitation field over a fixed area (e.g., a river catchment),
- considering the structure of the precipitation field (e.g., scattered convective cells, frontal rain, ...), and
- a one to one matching between the reference and the observed field is not required.

As a first step individual precipitation objects have to be identified for calculating the location and structure components. Therefore, a precipitation threshold is chosen:

$$R^* = fR^{\max}. \quad (3.38)$$

In Equation 3.38 R is the precipitation field, R^* is the precipitation threshold, and R^{\max} is the maximum rainfall within the considered domain. For the constant f , Wernli et al. (2008) suggested a value of $f = 1/15$ because this factor leads to contours which are reasonable with contours identified by eye. Gridcells cluster to an object if one of the neighborhood cells is above the threshold f . A possible algorithm to identify objects can be found in Wernli and Sprenger (2007).

The amplitude component A is calculated by using the normalized differences of the average precipitation values:

$$A = \frac{D(R_x) - D(R_o)}{0.5 [D(R_x) + D(R_o)]}. \quad (3.39)$$

$D(R)$ denotes the domain average precipitation in the observed (o) or simulated (x) field.

$$D(R) = \frac{1}{N} \sum_{(i,j) \in D} R_{ij}, \quad (3.40)$$

where R_{ij} are the grid-point values of the precipitation amount. A is a simple quantity, showing information of the domain wide amount of precipitation by ignoring the fields sub-regional structure. It has values between $[-2 \dots +2]$ whereby a perfect simulation in terms of amplitude leads to $A = 0$. An A -value of ± 1 corresponds with an over- or underestimation of precipitation by the factor of 3.

The location component L consists of two additive parts: $L = L_1 + L_2$:

$$L_1 = \frac{|\mathbf{x}(R_x) - \mathbf{x}(R_o)|}{d}, \quad (3.41)$$

where d is the maximum distance between two boundary points of domain D and $\mathbf{x}(R)$ corresponds to the center of mass of the precipitation field R . L_1 has values between 0 and 1 and gives a first-order estimation of the precipitation distribution in the considered region whereby $L_1 = 0$ if the centers of mass are at the same location. However, many different fields can have equally centers of mass which makes the second quantity L_2 necessary. It accounts for the distances between the center of mass of the total precipitation field and single precipitation objects. Therefore, the total precipitation amount is calculated for every object:

$$R_n = \sum_{(i,j) \in R_n} R_{ij}. \quad (3.42)$$

Then the averaged and weighted distances r between the centers of mass of the individual objects are calculated:

$$r = \frac{\sum_{n=1}^M R_n |\mathbf{x} - \mathbf{x}_n|}{\sum_{n=1}^M R_n}, \quad (3.43)$$

whereby, M is the total number of precipitation objects. r can have a maximum value of $d/2$ (half of the maximum distance between two grid points in the domain). It is zero if there is only one object in the domain. It should be noted that $\sum_{n=1}^M R_n$ is not equal to $\sum_{(i,j) \in D} R_{ij}$ (in Equation 3.40) because the former only considers grid-points above the threshold R^* . L_2 is now calculated as follows:

$$L_2 = 2 \left[\frac{|r(R_x) - r(R_o)|}{d} \right]. \quad (3.44)$$

L_2 is only greater than zero if either the observation or the simulation has more than one object in the domain. L_2 can range from zero to one which means that L can have values between zero and two. Zero indicates that the total center of mass as the averaged distances of the objects and the center of mass are the same in the observation and in the simulation. However, this does not mean a perfect match between the two fields, because the L -value is for example invariant to rotations around the center of mass.

The last missing component in the SAL method is the structure (S) component in which the volumes of the precipitation objects are compared and which contains information about the mass and the shape of the objects. Therefore, first a scaled volume V_n is calculated for every object:

$$V_n = \sum_{(i,j) \in R_n} R_{ij} / R_n^{\max} = R_n / R_n^{\max}. \quad (3.45)$$

In Equation 3.45 R_n^{\max} stands for the maximum precipitation within the object n and has to be $R_n^{\max} \leq R^{\max}$. Then V , the weighted mean of all objects scaled precipitation volume is computed for the reference and the simulated field:

$$V(R) = \frac{\sum_{n=1}^M R_n V_n}{\sum_{n=1}^M R_n}. \quad (3.46)$$

Similar to the A -component, the S -component is the normalized difference in V :

$$S = \frac{V(R_x) - V(R_o)}{0.5 [V(R_x) + V(R_o)]}. \quad (3.47)$$

S becomes negative if too small or too peaked objects are simulated or positive if widespread precipitation is modeled but small convective cells are observed.

3.2.2.4 Field Deformation

Field deformation approaches have in general, that they evaluate how much a field has to be transformed to match the observation. This is in particular interesting for precipitation because models often produce phase errors and displace weather systems in space or time.

Often used methods and their references are:

- Displacement Amplitude Score (Keil and Craig 2007),
- Forecast Quality Index (FQI) (Venugopal et al. 2005), and
- Image Warping (e.g., Dickinson and Brown 1996; Alexander et al. 1999; Åberg et al. 2005; Gilleland et al. 2010).

To give an idea how these methods are working the Displacement Amplitude Score (Keil and Craig 2007) is discussed as an example below.

Displacement Amplitude Score The displacement amplitude score was published by Keil and Craig (2007) and in a revised version by Keil and Craig (2009). An optical flow technique is used to avoid problems in identifying features and problems occurring through linking specific objects in the simulation to objects in the observation.

The optical flow method is based on a pyramid algorithm where the fields first are re-gridded on a coarser grid where 2^F pixels are averaged on one pixel element. F is

thereby called the sub sampling factor. On the coarse grid for every grid-cell of the simulation the distance of the minimum squared error (compared to the observation) is searched in a neighborhood of ± 2 grid-cells. The obtained vector field of displacements is then applied to the original simulated image which generates an intermediate image accounting for large-scale displacements. Afterwards, the intermediate image is coarse grained by averaging 2^{F-1} pixels which is the next pyramid level and the displacement vector field is calculated and applied as mentioned above. This algorithm is repeated until the full resolution is obtained. After the total displacement vector field, which morphs the simulation to the observation, is defined, the displacement vector field, which morphs the observation to the simulation, is calculated with the same algorithm.

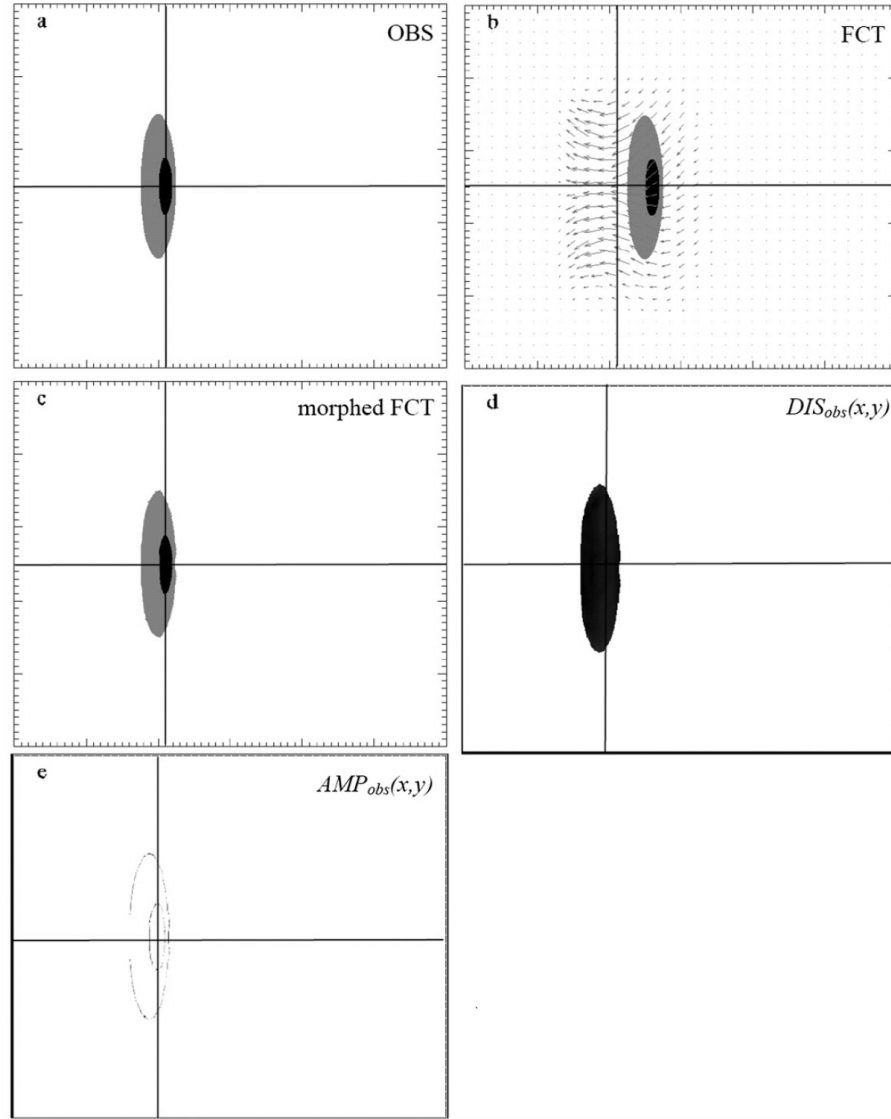
The resulting displacement vector fields are the sum of the vector fields at each pyramid level and are used to build the final morphed images. More details on the algorithm can be found in Keil and Craig (2007) and Zinner et al. (2008).

The displacement and amplitude score is then calculated by considering two quantities. The first accounts for the displacement error which is the magnitude of the displacement vector giving the distance of a simulation to an observed object (if any). The second accounts for the amplitude error which is the difference between the observed and the morphed simulation field. Accordingly, the same quantities are calculated for the morphed observation onto the simulation.

If two objects in the simulation and the observations are separated by more than the maximum search distance, they are treated as two independent objects and the amplitude error accounts for one missed event and one false alarm.

Finally, the displacement and amplitude errors are combined to yield the displacement amplitude score. Thereby, the two components are weighted so that the maximum possible displacement error between two objects equals the amplitude error for the same two objects that would occur if the distance between the two objects would have been larger as the maximum search distance.

To visualize the above described formalism, Figure 3.6 shows an idealized example of an observation (panel a) and an identical forecast field (panel b) which is 50 pixels shifted to the right. Also shown in panel b is the displacement vector field which minimizes the differences between the observation and forecast. In panel c the morphed forecast is displayed. The magnitude of the displacement vector field which is within the boundaries of the observed object is quite uniform as visible in panel d. Finally, panel e shows the amplitude error between the observed and morphed forecast field. The small remaining residual errors at the object boundaries are caused by the interpolation during the morphing.



H

Fig. 3.6 An idealized example of an observed object (OBS) (panel a) and a forecasted (FCT) object (panel b) which is 50 grid-boxes shifted to the right. Here the simulation is shifted towards the observation. Panel b shows the vectors of the displacement array. Panel c displays the morphed forecast while panel d shows the observation space displacement error field and panel e the amplitude error field (from Keil and Craig 2009).

Tab. 3.12 Attributes measured by the traditional and new spatial precipitation verification methods (after Brown et al. 2009).

Attribute	Traditional	Feature Based	Neighbor-hood	Scale	Field Deformation
Performance at different scales	Indirect	Indirect	Yes	Yes	No
Location errors	No	Yes	Indirect	Indirect	Yes
Intensity errors	Yes	Yes	Yes	Yes	Yes
Structure errors	No	Yes	No	No	Yes
Hits, etc.	Yes	Yes	Yes	Indirect	Yes

3.2.2.5 Overview of the Ability of Spatial Rainfall Verification Methods

The spatial verification methods introduced in the subsections above provide great opportunities for better interpretable and more accurate precipitation evaluations. Thereby, each method is useful in certain situations and to answer certain questions. However, all of them also have limitations.

The major limitation of feature based approaches (scale separation and feature based) is that they do not clearly isolate different kinds of errors (e.g., amplitude, displacement). In case of the displacement methods (feature based and field deformation) the matching criteria are somehow arbitrary and many parameters have to be fitted.

Advantages of feature based approaches are that they account for uncertainties in the simulation and the observation and are able to deal with unpredictable scales. They give scale dependent information and are mostly simple and easy to interpret. The displacement approaches are able to measure the displacement and give credits to close precipitation fields. Furthermore, feature based approaches are able to measure the structure of precipitation while field deformation methods are able to account for aspect ratio and orientation of the rainfall objects.

In Table 3.12 a quick overview is given on the attributes that are measured by different methods.

4

Added Value in Convection Permitting Simulations

THIS chapter consists of two separate studies. In the first one, presented in Section 4.1, convection permitting climate simulations (CPCSs) of three different regional climate models (RCMs) are compared to coarser resolved simulations. Multiple statistical methods are applied to get a holistic view of added value which can be consistently found in different RCMs. The second study in Section 4.2 builds up on the results of the first one. Here the representation of heavy precipitation events in one CPCS and two coarser gridded runs are investigated by comparing the simulations with observations on different spatial scales.

4.1 Added Value of Convection Permitting Seasonal Simulations

In this section an ensemble of non-hydrostatic RCMs is evaluated, which allows more general conclusions than the analysis of single models. In addition to the often evaluated parameters precipitation and two meter air temperature also relative humidity, and global radiation are analyzed. The study area contains the eastern part of the European Alps and a mountainous and a hilly sub-region therein.

The major scientific question, which leads through this study is: which aspects can be consistently improved by CPCSs compared to coarser gridded simulations? To answer

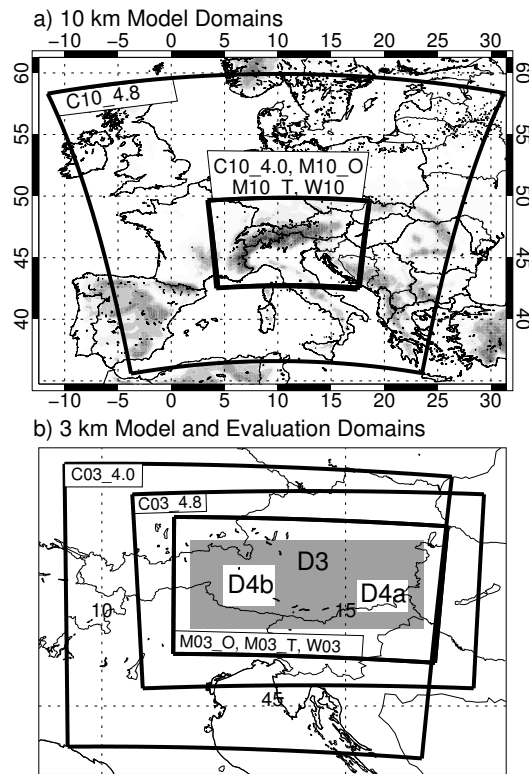


Fig. 4.1 Computational domain boundaries for the 10 km (panel a) and 3 km simulations (panel b). Additionally the evaluation domain D3 (gray box) and the two sub-regions D4a and D4b (white boxes therein) are displayed (panel b).

this question, results which are consistent in the majority of the simulations are emphasized. The analyzed ensemble consists of five simulations on a approximately 10 km horizontal grid and five simulations on a approximately 3 km grid which are performed with three different RCMs. In the next section basic information about the used model ensemble and reference data are provided. In the following two sections results are presented and discussed in detail. The last two sections show summaries and results.

4.1.1 Experimental Setup, Data, and Models

Figure 4.1 depicts the model and evaluation domains which are used in this study. The domain setup differs between the different simulations, but all 10 km simulations cover at least the European Alpine region and all 3 km simulations cover at least D3. The evaluations are focusing on D3 and the sub-regions D4a and D4b. The minimum distance

between the evaluation domain D3 and the lateral boundaries of the RCMs is eight grid-boxes and therefore larger than the relaxation zones. The first sub-region represents a hilly area in south-eastern Styria (D4a) which lies on the foothills of the Alps. The climate of this region is characterized by the predominant influence of Mediterranean cyclones and deep convection especially in summer. From the North and the West, the region is shielded by the Alps. In summer, convective precipitation events on the one hand and partly long lasting dry spells on the other hand characterize this region. The typical weather conditions in winter are dry ones. The second sub-region is centered on the highest peaks of the Austrian Alps which are in the Hohe Tauern National Park (D4b). The Großglockner, with an elevation of 3798 m, is the highest summit in this region, and the valleys are roughly on a height of 550 m. Precipitation patterns in this area reveal a great spatial variability from the scale of single slopes upwards. There is a precipitation maximum in summer and a minimum in spring or fall (Barry 2008). The strong surface height variation and the diversity of weather and climate regimes within a relatively small region are challenging tasks for RCMs.

In order to capture a significant part of the broad range of weather regimes the periods June, July, and August (JJA) 2007 and December 2007, and January and February 2008 DJF are chosen for the simulations. Compared to the climatological mean, JJA was warmer than average and had at the same time an average amount of precipitation. In DJF warm and dry conditions were predominant. The main reason for the selection of these two seasons was the availability of homogeneous, highly resolved lateral boundary conditions (LBCs) and reference data.

Three RCMs have been used for the simulations.

- The Wegener Center of the University of Graz (WEGC) used the COnsortium for Small scale MOdeling COSMO Model in Climate Mode CCLM in the version 4.0. The CCLM is the climate version of the former “Lokalmodell” of the German weather service with a non-hydrostatic core. A detailed description of the COSMO model is given by Steppeler et al. (2003) and Doms and Förstner (2004) and for the CCLM model by Böhm et al. (2006), Rockel et al. (2008b), and in Section 3.1.
- CCLM was also used by the Brandenburg University of Technology Cottbus (BTU) but in the version 4.8. The major differences to CCLM 4.0 are that, beside corrections and modifications of the source code, a new reference atmosphere and a subgrid-scale orography scheme were introduced in version 4.8. However, there are also some differences in the model setup (see Table 4.1). These simulations are described into some details by Georgievski et al. (2011).
- WEGC also applied the Pennsylvania State University (PSU)/National Center for Atmospheric Research (NCAR) Fifth-Generation NCAR/Penn State Mesoscale Model (MM5) version 3.7.4. Details about the model are given in Dudhia (1993).
- The Weather Research and Forecasting Model (WRF) version 2.2.1 was again used

by WEGC. Like the other RCMs it has a non-hydrostatic core and is developed by several research institutes in the USA. A detailed description can be found in Skamarock et al. (2005).

The major difference between the simulations with 10 km horizontal grid-spacing and those with 3 km is that the deep convection parameterizations are switched off in the latter. Simulations on the 3 km grid are permitting deep convection and hence they are referred to as CPCs. The 3 km simulations use the results of the coarser simulations as lateral boundary conditions (LBCs) in two different ways. The first one is called one-way coupling, which means that there is no feedback of information from the 3 km simulation to the 10 km run and information from the 10 km to the 3 km simulation is only provided via the lateral boundaries. This approach was used for the CCLM simulations and one pair of MM5 runs (M10_O and M03_O; see Table 4.1 for acronyms). In COSMO model in CLimate Mode (CCLM), hourly data from the 10 km simulations were provided as lateral boundaries of the CPCs, while the CPC of MM5 was updated every time step of its parent simulation (20 seconds). The second approach is called two-way coupling, meaning that there is a feedback from the 3 km to the 10 km simulation. Thereby, information from the interior of the 3 km domain is fed into the 10 km domain every time step and the 10 km simulation is fed into the 3 km simulation via the LBCs, in turn. The feedback from the interior of the 3 km domain is realized by replacing the coarse grid solution with the solution of the coincident points of the fine grid. For numerical stability, the fed back fields are additionally smoothed with a five point 1–2–1 smoother that removes two-grid-length noise, and damps other short wavelengths strongly. The models thereby do not conserve mean values. The advantage of a two-way nesting approach is a better behavior at outflow boundaries of the finer gridded simulation. A similar two-way coupling approach was used in the WRF simulations and the second pair of MM5 runs (M10_T and M03_T). Detailed information about the model setups, the nesting strategies, and the hereafter used acronyms of the simulations can be found in Table 4.1.

For the 10 km simulations the LBCs were taken from the Integrated Forecast System (IFS) of the European Centre for Medium-Range Weather Forecasts (ECMWF). Those data have a T799 L91 resolution (roughly 25 km horizontal grid-spacing at mid latitudes, and 91 vertical levels). A temporal resolution of three hours is achieved by combining IFS analyses (00, 06, 12, and 18 UTC) and short-term forecast fields (3+ h and +9 h of the 00 UTC and 12 UTC forecasts; see also Suklitsch et al. (2011)). It is assumed that these boundary conditions represent the real weather conditions adequately, and hence the RCMs performance can be judged apart from the quality of the LBCs.

The surface boundary conditions (SBCs) were initialized with two different spin-up periods. For the CCLM4.0 and MM5 simulations a long spin-up period was imitated by initializing the SBCs from simulations which start at the beginning of January 2007. This has the advantage that the soil with its long term memory for initial conditions

(e.g., Seneviratne et al. 2006) can be assumed to be in a more balanced state at the beginning of the simulations. A shorter spin-up period of one month (May for JJA 2007 and November for December, January, and February (DJF) 2007 to 2008) was used in the WRF and CCLM 4.8 simulations.

The evaluations in this study are performed with the Integrated Nowcasting through Comprehensive Analysis (INCA) dataset (Haiden et al. 2010), provided by the Austrian Central Institute for Meteorology and Geodynamics (ZAMG). The INCA dataset has a $1 \text{ km} \times 1 \text{ km}$ resolution on an hourly basis and covers the Austria territory. It is derived through a combination of numerical weather predictions (NWP) (ALADIN, ECMWF) with current observation data from stations, radars, and satellites, and is further refined with highly resolved orographic information. The station density is especially high in mountainous regions. However, most of the stations are located in the valleys. More technical details about the INCA system and its data processing can be found in Haiden et al. (2010).

The usage of the INCA dataset as reference data has two major advantages. First, its high spatial and temporal resolution and second, it allows for an assessment of the RCMs performance by providing the following four atmospheric parameters: air temperature two meters above surface (T2M), precipitation amount at surface (PR), relative humidity two meters above surface (RH), and global radiation at surface (GL).

However, the advantage of the high spatial and temporal resolution of INCA has also a disadvantage. Even though INCA is constrained by observations, the output contains errors especially in regions with low station density. For T2M, a mean absolute error of 1.0 K to 1.5 K in lowland areas and 1.5 K to 2.5 K in Alpine valleys is estimated (Haiden et al. 2010). Precipitation mean absolute errors for point values and 15 minutes time scale can reach up to 50 % in summer and more than 100 % in winter. For larger scales of the order of 100 km^2 the errors get significantly smaller. Relative humidity was found to be very accurate (5 % to 7 %) in a hilly sub-region in southern Styria (Kann et al. 2011). However, no information is available about the accuracy of relative humidity in mountainous areas and global radiation in general.

4.1 Added Value of Convection Permitting Seasonal Simulations

Tab. 4.1 Listing of all simulations with their acronyms and key settings. For CPCs only differences to their corresponding 10 km simulations are mentioned.

Acronym	Numerical settings	Physical settings
C10_4.0	3 rd order two time-level Runge-Kutta split-explicit scheme (3rd RK) (Klemp and Wilhelmson 1978; Wicker and Skamarock 2002); time step (Δt) is 80 s	Kain-Fritsch (KF) moist convection (Kain and Fritsch 1993; Kain 2003); cloud ice scheme with prognostic cloud water and cloud ice, prognostic rain and snow; turbulent kinetic energy (TKE)-based turbulence scheme including sub-grid-scale effects of condensation/evaporation; Ritter and Geleyn (1992) RG92 radiation scheme.
C03_4.0	3rd RK; Δt is 25 s	shallow convection; graupel as additional prognostic variable
C10_4.8	2 nd order leapfrog scheme (2nd LF) (Grell et al. 1995); Δt is 60 s	Tiedtke moist convection (Tiedtke 1989); cloud ice scheme with prognostic cloud water and cloud ice, prognostic rain and snow; RG92 radiation scheme
C03_4.8	3rd RK; Δt is 25 s	shallow convection; graupel as additional prognostic variable
M10_O	2nd LF; Δt is 20 s	KF moist convection; LBCs between finer and coarser model domains are updated with the model-internal time steps but two-way coupling (TWC) is applied; Dudhia short wave radiation scheme (Dudhia 1989)
M03_O	Δt is 6.67 s	shallow convection
M03_S	as M03_O but with smoothed 10 km orography field	
M10_T	as M10_O but TWC with M03_T. One-point feedback with heavy smoothing (OFHS) is applied.	
M03_T	as M03_O but TWC with M10_T. OFHS is applied.	
W10	3rd RK; Δt is 20 s	KF moist convection; Eta grid-scale cloud and precipitation scheme (Rogers et al. 2001); TWC with W03 with OFHS; Dudhia short wave radiation scheme
W03	Δt is 20 s	no convection parameterization

4.1.2 Results

This chapter is made up of four parts according to the different evaluation aspects of the simulations. In Subsection 4.1.2.1 the error ranges of the seasonal mean fields are analyzed. In Subsection 4.1.2.2 the representation of sub-daily processes, temporal variability, and correlation on grid-point-scale is focused. In Subsection 4.1.2.3 the representation of extremes in the models is analyzed and in Subsection 4.1.2.4 advanced evaluation methods are used to evaluate hourly precipitation fields.

4.1.2.1 Spatial Error Ranges and Variability

Figure 4.2 shows spatial error ranges of the seasonal bias fields. The term “error range” used here denotes the distance between the 25 % to the 75 % quantile of the error and is visible as box lengths in Figure 4.2.

In JJA the error ranges of all CPCs for T2M are smaller than those of the corresponding 10 km simulations and those of IFS (Figure 4.2 a). The average error range decreases by 0.6 K from 2.4 K in the 10 km simulations to 1.8 K in the CPCs. This effect is especially strong in the mountainous region D4b and it is smaller in the hilly region D4a (both not shown).

In DJF (Figure 4.2 b) the average error ranges of the CPCs and the 10 km simulations are both 1.9 K. Only the C03_4.8 and M03_O simulations are able to reduce the error ranges of their parent simulations. In DJF the CCLM 4.0 simulations have a remarkably strong cold bias of -3 K whereas the median biases of the other simulations are similar to those in JJA.

The JJA relative PR and the relative error ranges in both 3 km CCLM simulations are increased compared to the 10 km simulations (Figure 4.2 c). This is different in the one-way nested MM5 simulations because in M10_O PR is highly overestimated in large areas of D3 which is not the case in the M03_O run leading to decreasing error ranges. In all three one-way coupled simulations, the median JJA precipitation sums are not improved in the CPCs. For the two-way coupled MM5 and WRF simulations the error ranges stay nearly constant, because the 3 km fields are fed back to their driving 10 km parent simulation.

In DJF (Figure 4.2 d) the relative error ranges of PR are much larger than those in JJA. However, the absolute error ranges (not shown) are smaller because there is generally less PR in winter and DJF 2007 to 2008 was remarkably dry in many parts of the Eastern Alps. In this season IFS has clearly a smaller error range than all RCM simulations. There is a slight decrease in median PR of the CPCs which improves the general wet bias of the 10 km simulations (except for M03_O). Like in JJA the error ranges of the two-way coupled 3 km and 10 km simulations of MM5 and WRF are very

similar but in DJF also those of the one-way coupled simulations do not differ notably.

The median errors of RH in JJA and DJF are roughly within $\pm 10\%$. MM5 and WRF are generally too dry and both versions of CCLM are too wet (Figures 4.2 e and 4.2 f). In DJF the error ranges are larger than in JJA, but an improvement of the median biases of the CPCs can be seen except for M03_O. The error ranges are not reduced in the CPCs in general.

All CPCs have higher GL values compared to their parent simulations which is stronger pronounced in JJA (Figure 4.2 g) but also visible in DJF (except for C03_4.0 and M03_O) (Figure 4.2 h). Comparing the individual RCMs, the CCLM4.0 has a strong negative bias in JJA GL which is most probably related to an overestimation of cloud cover in this model. All other relative median RCM biases are within a range of $\pm 20\%$. Remarkable is the different behavior of the one-way and two-way nested simulations of MM5. The M03_O and M03_T simulations look very similar but the M10_O has much higher GL values than the M10_T. In DJF (Figure 4.2 h) the relative error ranges are larger for CCLM and WRF than those in JJA. However, the absolute error ranges are smaller because of the lower GL values in DJF. In general, the CPCs do not reduce the error ranges.

Summing up, the only systematic added value in terms of seasonal mean spatial patterns of CPCs is found in summertime temperature. Large differences between the two resolutions have been found in summer precipitation patterns in case of one-way coupling. In addition, summertime global radiation is systematically increased in the high-resolution simulations. In winter, the differences between the two resolutions are less systematic and less pronounced.

Concerning the overall performance, the CCLM 4.0 simulations show often larger error ranges (e.g., GL in DJF Figure 4.2 h) or larger differences (e.g., T2M in DJF Figure 4.2 b or GL in JJA 4.2 g) than the rest of the simulations. Because of this and because the differences between the C10_4.0 and C03_4.0 simulations are similar to the differences between the C10_4.8 and C03_4.8 runs the results of the CCLM 4.0 simulations are not shown in the evaluation results of the next section. This also reduces the information density in the plots and helps to focus on the essential information.

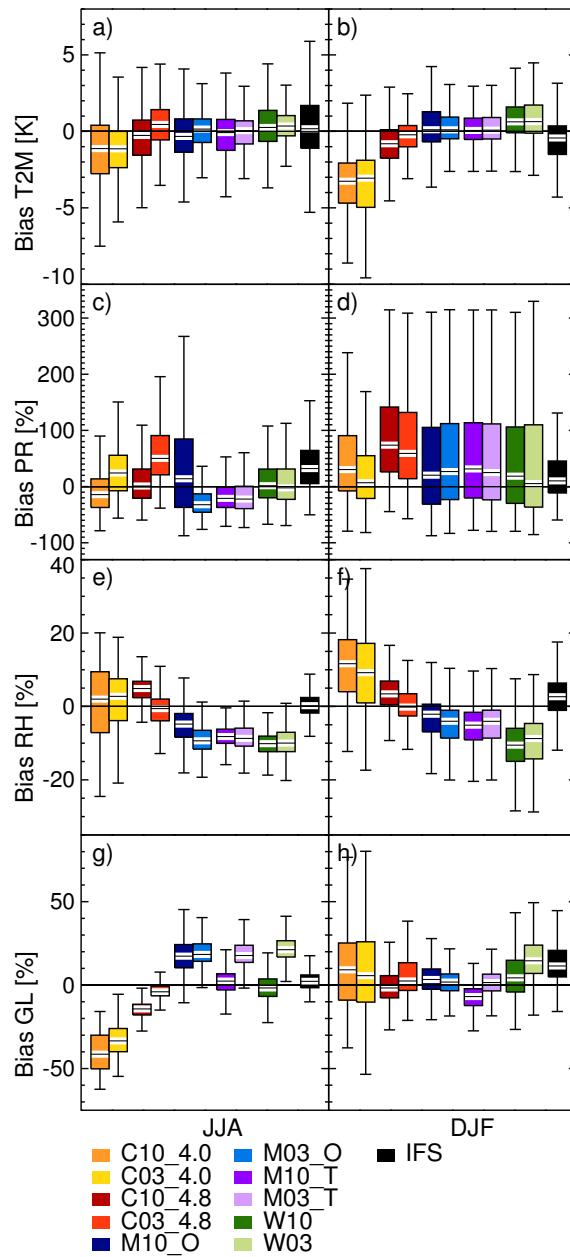


Fig. 4.2 Spatial box-whisker plots of the seasonal mean bias fields of domain D3 for T2M, PR, RH, and GL (top down). Relative differences are depicted for PR and GL. Left column shows results of JJA and right column those of DJF. The box length denotes the 25% and 75% quantile of the grid-cells in D3, the whiskers have maximal one and a half times the length of the box.

4.1.2.2 Diurnal Cycles, Temporal Correlation, and Variability

In this subsection the temporal performance of the RCMs is analyzed. For this purpose, two methods are used: diurnal cycles of the spatially averaged fields and Taylor plots (see Subsection 3.2.1.2) where hourly time series are evaluated on grid-point basis.

Diurnal Cycles In Figure 4.3 the mean diurnal cycles of the spatially averaged fields are displayed for the the eastern part of the European Alps and the two sub-regions D4a and D4b.

The diurnal cycles of JJA T2M (Figure 4.3 a, b, c) are scattered around those of INCA within a range of ± 2 K. In DJF (Figure 4.3 A, B, C) the performance of the RCMs is roughly the same. In both seasons, the CPCSs have no deviations from their parent simulations in common.

In JJA PR has a distinct diurnal cycle with a maximum in the afternoon due to convective rainfall in D3 (Figure 4.3 d) which is most pronounced in the mountainous region (Figure 4.3 f). In the hilly sub-region D4a (Figure 4.3 e) no distinct diurnal cycle is visible. All RCMs are able to qualitatively reproduce this diurnal cycle and they are generally improving the timing of the afternoon peak compared to IFS. An added value in the one-way nested CPCSs compared to their parent simulations becomes visible in the better timing of the PR peak later in the afternoon and a more correct onset of PR at noon. While the C03_4.8 simulation deteriorates the amplitude of the diurnal cycle the M03_O simulation improves the amplitude of the afternoon peak compared to M10_O. The two-way coupled 10 km and 3 km simulations have nearly identical diurnal cycles.

In DJF (Figure 4.3 D, E, F) PR shows no clear diurnal cycle. The RCMs perform well in D4a (Figure 4.3 E) and overestimate PR in D4b (Figure 4.3 F) which contributes to a general overestimation of PR in D3 (Figure 4.3 D). There is no systematic difference between the 10 km simulations and the CPCSs in winter.

The diurnal cycle of RH is inversely related to T2M, but reveals some additional information and distinct model deficiencies. The shape is captured reasonably well by all simulations during JJA (Figure 4.3 g, h, i) but the minima occur too early and partly large offsets to INCA exist in the MM5 and WRF simulations. In DJF (Figure 4.3 G, H, I) the RCMs have more problems to properly reproduce the diurnal cycle of RH. The performance becomes worse in the mountainous region D4b (Figure 4.3 I) where the CCLM and the WRF simulations have nearly constant RH values during the entire day and all four MM5 simulations even show an inverse diurnal cycle. In both seasons no common differences between the CPCSs and their parent simulations are visible.

Concerning the diurnal cycle of GL (not shown) the amplitude of the CPCSs is higher than those of the 10 km simulations, especially during summer in the mountains. This

is consistent with the results from Subsection 4.1.2.1 (Figure 4.2).

In summary, the major added value of CPCs in the diurnal cycle is found in the more correct timing of the afternoon maximum and the noon onset of convective precipitation in summer and especially over mountainous terrain.

Temporal Correlation and Variability The ability of the RCMs to reproduce the temporal characteristics (Pearson’s correlation coefficients and standard deviations) of the considered atmospheric parameters on an hourly and grid-point basis in D3 is analyzed with the help of Taylor plots (Figure 4.4; the Taylor plot method is described in Subsection 3.2.1.2).

In all simulations the temporal correlation of T2M lies between 0.88 to 0.93 in JJA (Figure 4.4a) and 0.83 to 0.90 in DJF (Figure 4.4b). There are only small differences (below 0.02) in the median correlation coefficients between the CPCs and their parent simulations. Concerning the median normalized standard deviation in JJA the CPCs show a small (below 5%) but consistent increase compared to their parent simulations while in DJF there are positive and negative differences. IFS has the highest correlation coefficients in both seasons. The generally high correlation coefficients are not surprising as the main part of the correlation is caused by the diurnal cycle. Correlation is worse for variables that have no regular diurnal variation. In JJA the temporal standard deviation is well captured in all simulations while in DJF the standard deviations are slightly underestimated. The horizontal and vertical lines, which represent the 25% to 75% quantile distance of individual grid-point values are not visible, because those values are clustering very dense around the median correlation coefficients and normalized standard deviations. This means, there is no big difference in temporal correlation coefficients and standard deviations in different areas of D3.

For PR in JJA (Figure 4.4c) the correlation coefficients are between 0.12 and 0.25 and the standard deviations are spreading widely, which can be seen from the large vertical 25% to 75% quantile distance. Common in all CPCs is their higher temporal variability compared to their parent simulations. The poor performance of highly resolved simulations of PR is a well known issue and is related to the “double penalty problem” which is discussed in Subsection 3.2.2. To avoid this problem special methods like the fractions skill score (FSS) or the Structure-Amplitude-Location (SAL) analysis are applied in Subsection 4.1.2.4. In DJF (Figure 4.4d) the correlation is generally higher than in JJA because of the predominance of large-scale precipitation which is more deterministic than convective precipitation. Datapoints of individual gridcells are spreading widely according to the large 25% to 75% quantile distances. Compared to their parent simulations all CPCs show an increase in the median normalized spatial standard deviation which is largest (10%) in the M03_O simulation. All RCMs have too high standard deviations and the differences in the correlation coefficients between

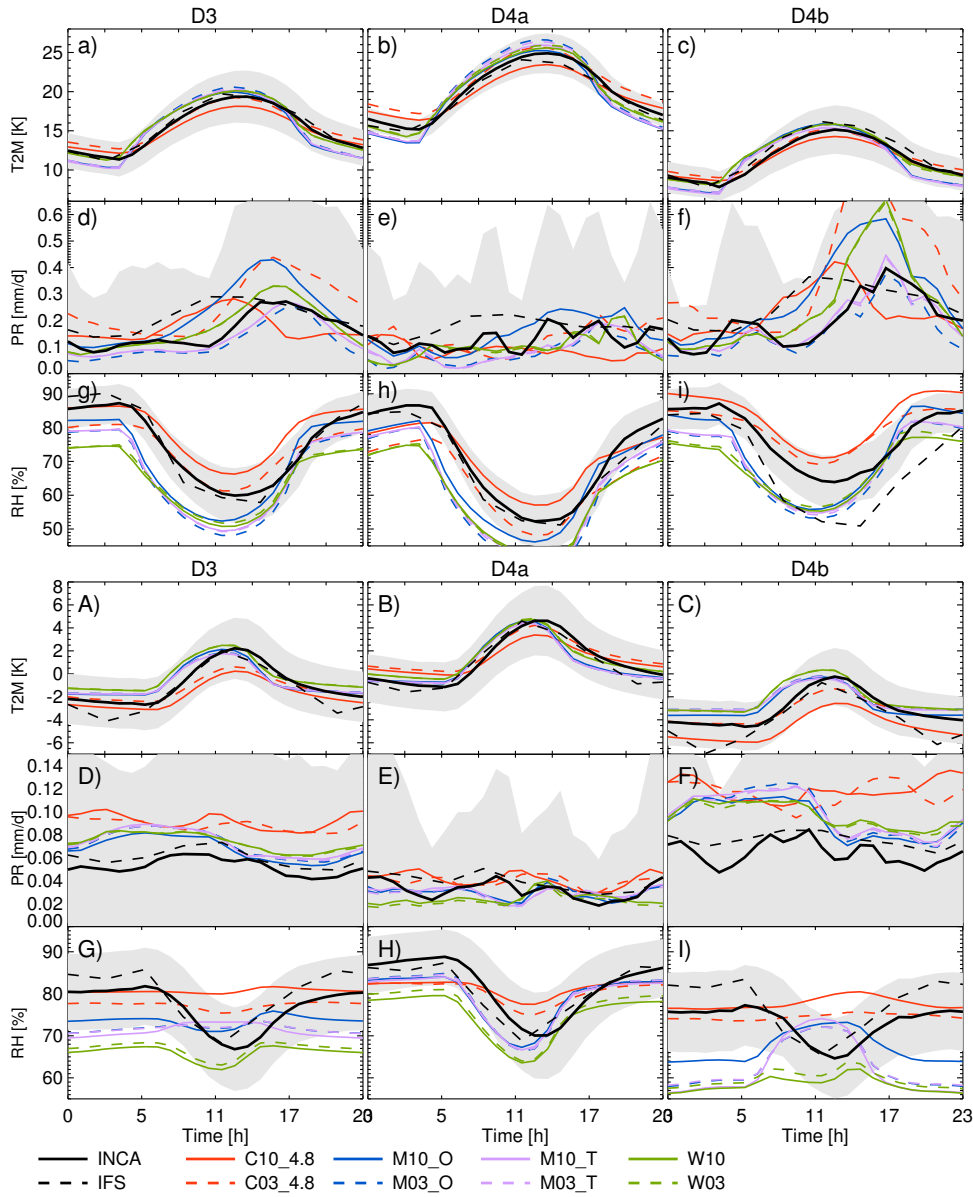


Fig. 4.3 Diurnal cycles of the spatially averaged simulations in domain D3, and in the sub-regions D4a, and D4b (left to right). The upper half of the figure (small letters) show results for JJA and the lower half (capital letters) those for DJF. In each panel the rows display T2M (panel a to c and A to C), PR (panel d to f and D to F), and RH (panel g to i and G to I). The shaded area depicts the 25% and 75% percentiles of spatially averaged diurnal cycles of the reference data (INCA).

CPCSs and their parent simulations are inconsistent.

For RH in JJA (Figure 4.4 e) the majority of the simulated correlation coefficients are lower than those of IFS. The CPCSs feature slightly smaller correlation coefficients than their corresponding 10 km runs, except for C03_4.8. In common are increased median normalized standard deviations in the CPCSs (4 % to 6 %). The CCLM (MM5) simulations have generally too low (high) temporal variability, while it is well represented in WRF. In DJF (Figure 4.4 f) the correlation coefficients of the CCLM simulations are lower than in JJA. Also the standard deviations are too low which is in agreement with the nearly constant averaged diurnal cycles shown in Figure 4.3 I. The differences in the median correlation coefficients are inconsistent however, the median normalized standard deviations are commonly larger in the CPCSs (except for C03_4.8).

The RCMs capture the temporal characteristics of GL with median correlation coefficients between 0.85 and 0.93 in JJA (Figure 4.4 g). Note, a major part of these high values belong to the diurnal cycle of the sun. A shift towards higher temporal variability is visible in all CPCSs compared to their parent simulations, which is consistent with generally higher GL values of the CPCSs (see e.g., Figure 4.2 g). Similar results are found in DJF (Figure 4.4 h), but the correlation coefficients are higher than in JJA with values ranging from 0.93 to 0.95.

In summary, there are no systematic changes in the temporal correlation coefficient or variability between the CPCSs and their parent simulations, except an increase of the variability in summer precipitation and global radiation. High correlation coefficients and accurate variability can be found for all simulated temperature and global radiation fields, while for relative humidity the simulations of MM5 and WRF are outperforming those of CCLM which shows too low temporal variability. Results for precipitation are especially poor in summer, partly due to the double penalty problem (see Subsection 4.1.2.4).

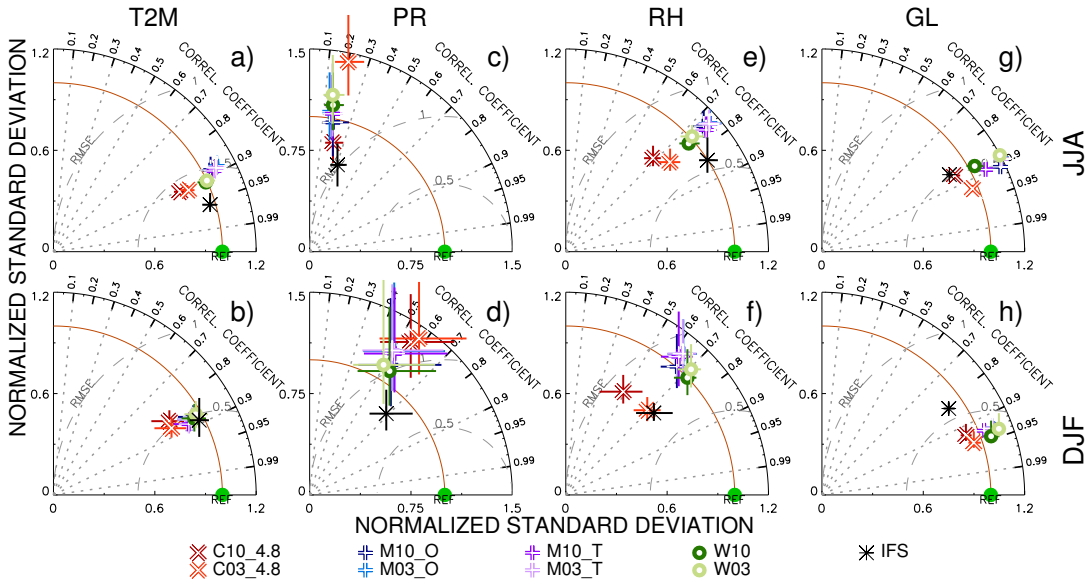


Fig. 4.4 Taylor plots of hourly values on grid-point basis. Different colors and symbols indicate different simulations. The median statistical values are shown as symbols and the spread of the data points (25 % quantile to 75 % quantile) are shown as vertical and horizontal lines. The upper panels show results for JJA and the lower one those for DJF. Columns correspond to T2M, PR, RH, and GL (from left to right).

4.1.2.3 Extremes

In this subsection the differences between the distributions of hourly, grid-point values of INCA and the RCM simulations by focusing on the representation of extremes, defined as values below the 5 % and above the 95 % percentile are analyzed.

For T2M in JJA (Figure 4.5 a) and DJF (Figure 4.5 A) the CPCs have generally lower minima (Q0) and higher maxima (Q100) than their corresponding 10 km simulations, which results in a more realistic distribution in most cases (compare Subsection 4.1.2.1). In JJA (Figure 4.5 a) the simulations have a larger spread and higher deviations from the reference dataset for minimum compared to the maximum T2M. The 0 % to 5 % (Q0–Q5) quantile values are slightly colder in all CPCs than in their parent simulations whereas the 95 % to 100 % (Q95–Q100) quantile values are generally warmer. In DJF (Figure 4.5 A) there are no such common changes. The RCMs are able to improve the extreme values of IFS in JJA, which has too low Q0–Q5 and too high Q95–Q100 values. In D4a (not shown) all simulations have too low minimum T2M while in D4b (not shown) all simulations have too low maximum temperatures.

Concerning hourly maximum grid-point precipitation, all CPCs have larger and more

realistic Q100 values than their parent simulations (Figure 4.5 b). An especially large improvement can be seen for the C03_4.8 run which reduces the Q100 difference of its parent simulation from -44 mm h^{-1} to $+9 \text{ mm h}^{-1}$ (Figure 4.5 b). However, there is no systematic difference between the two resolutions in the Q95–Q100 deviations. The lower quantile differences Q0 and Q0–Q5 are zero because of the many non-precipitating hours in the distribution of INCA and the simulations. Compared to IFS the RCMs are able to improve the median Q95–Q100 and Q100 difference. In the sub-domains D4a and D4b (not shown) similar results are found.

Similar to JJA there is also more intense PR in DJF (Figure 4.5 B) in the CPCs than in their parent simulations which reduces the differences to INCA. Nevertheless, the most extreme precipitation events are still underestimated by the CPCs in all simulations and all domains.

Concerning RH in JJA (Figure 4.5 c) there is a consistent decrease in the Q0–Q5 values in all CPCs compared to their parent runs while there are no common differences in the Q95–Q100 values. The W03 simulation and especially the MM5 runs have unrealistically high maxima which are partly close to 300 %. In DJF (Figure 4.5 C) the WRF simulations have unphysical minimum values which are below 0 % RH. There are no common changes in the Q0–Q5 and Q95–Q100 values between the CPCs and the corresponding 10 km simulations. All simulations are overestimating the median of the Q95–Q100 values by approximately 20 %. As in JJA all MM5 simulations have too high maximum values of RH. In D4a (not shown) extremes are better represented than in D3, while in D4b (not shown) the deviations from INCA distribution are especially large.

4.1 Added Value of Convection Permitting Seasonal Simulations

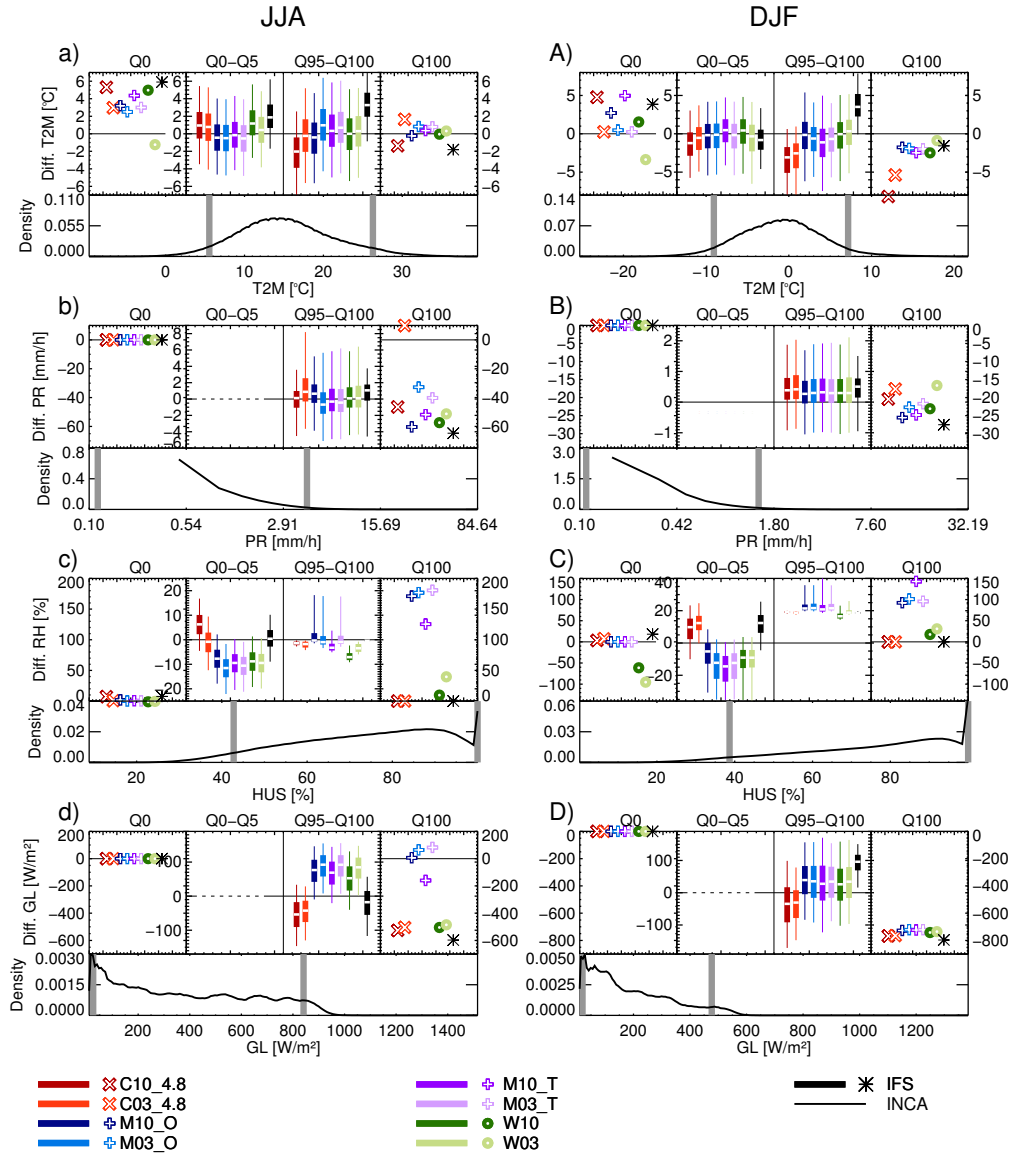


Fig. 4.5 Simulated minus observed quantile differences (upper panels) and density distributions of INCA (lower panels) for JJA (left) and DJF (right) for T2M, PR, RH, and GL (rows in top-down sequence) on D3. In the quantile differences plots the parts labeled with Q0 and Q100 show the difference in the minimum (Q0) respectively maximum (Q100) of the hourly grid-point values (simulations minus INCA). The box-whisker plots show the differences between the zero to fifth (Q0-Q5) (simulated minus INCA) and the 95th to 100th (Q95-Q100) quantile values. The two vertical gray lines in the density plot depict the 5% and 95% quantiles and the displayed x-axis range shows maximum and minimum values in INCA.

For GL (Figure 4.5 d and D), only the upper tail of the frequency distribution is of relevance in this study: the Q0 and Q0–Q5 values refer to nighttime conditions and hence deviations from INCA become vanishingly small. In JJA (Figure 4.5 d) the Q95–Q100 values of the CPCs are higher than in their parent simulations, which is not the case for the Q100 values. In DJF (Figure 4.5 D), no common changes between the CPCs and their parent runs are visible. The large negative deviations in the Q100 values can be attributed to erroneous maximum values in the INCA dataset.

Summing up, there is a consistent improvement in the representation of the most extreme hourly precipitation values in CPCs. In the case of T2M the CPCs have lower minimum values and higher maximum values than their parent simulations, which lead to more realistic cold temperature extremes in most cases.

4.1.2.4 Evaluation of PR at High Temporal and Spatial Resolution

The evaluation of simulated PR at high spatial and/or temporal resolution is difficult, because at small scales hourly PR partially gets unpredictable and double penalty problems can occur (e.g., Figure 4.4 c and Figure 4.4 d).

In this subsection two methods are applied, which are able to avoid the double penalty problem and to evaluate the spatial properties of high-resolution precipitation fields more appropriate than most traditional statistical methods, like correlations coefficients or mean square errors.

Fractions skill score Figure 4.6 depicts the average fractions skill scores FSSs of all records with precipitation in JJA depending on the selected threshold values and horizontal extension of the moving window (horizontal scale). Compared to IFS the FSSs are widely improved by the simulations especially for threshold above 1 mm h^{-1} (Figure 4.6 c). However, this improvement is partly caused by the three hourly resolution of IFS. The CPCs have higher FSS than their corresponding 10 km simulations (except the M03_T and W03 simulations below 1 mm h^{-1} threshold and the M03_O at all thresholds). Differences between the two resolutions are larger at higher precipitation thresholds (e.g., 2 mm h^{-1} in Figure 4.6 d). The scales on which the simulations have more than random skill are the same in both, the CPCs and their parent simulations in the two-way coupled simulations. C03_4.8 improves the scales at which C10_4.8 has more than random skill by a factor of 2 (for 0.5 mm h^{-1}) and a factor of 5 (for 2 mm h^{-1}). In the case of the one-way coupled MM5 simulations it is the other way around and the M03_O deteriorates the scale above random skill of the M10_O simulation. The main reason for this might be the general underestimation of PR in the M03_O simulation (cf. Figure 4.2). Above 5 mm h^{-1} threshold (Figure 4.6 e) only the CPCs and the M10_O simulation have FSSs greater than zero. The good performance of the M10_O simulation

compared to the M03_O run is partly related to the underestimation of precipitation in the latter which is very similar to the M03_T simulation.

In DJF (Figure 4.7) the differences between the FSSs of the CPCSs and their corresponding 10 km simulations are smaller than in JJA because winter precipitation is generally more dominated by large-scale and non-convective processes (e.g., frontal precipitation). However, except for the WRF and the one-way nested MM5 simulations, the CPCSs have higher FSSs and a better representation of small scales than their 10 km parent simulations. IFS has large FSSs at 0.1 mm h^{-1} threshold and outperforms all RCMs except WRF. For higher thresholds most simulations exceed the FSSs of IFS. Only the C03_4.8 run is able to improve the scales on which the simulations have more than random skill compared to its parent simulation (cf. Figure 4.7 b). For the other simulations there is no difference in this value except for the W03 run which deteriorates the performance of the W10 simulation.

Comparing the FSSs of JJA with those of DJF it becomes visible that at small threshold values (e.g., 0.1 mm h^{-1}) the FSSs are generally larger in DJF compared to JJA. This is because DJF precipitation is dominated by large-scale processes which are better represented in RCMs than convective precipitation occurring frequently in JJA. For higher thresholds (e.g., 0.5 mm h^{-1} or 1 mm h^{-1}) the FSS in JJA are larger than those in DJF because precipitation above e.g., 1 mm h^{-1} occurs more often in JJA than in DJF (Figure 4.5 b and 4.5 B), and the probability that it is observed and simulated at the same time is therefore much higher in JJA.

Structure-Amplitude-Location Evaluation The Structure-Amplitude-Location evaluation is an object based method which evaluates precipitation fields concerning the three characteristics after which it is named (see Subsection 3.2.2.3). Since we found that there are no large changes in the location (L) component between different simulations, the focus here lies on changes in the structure (S) and amplitude (A) component. It should be noted that the A-component is different from the PR bias, because in the SAL evaluation only records with precipitation in the INCA dataset are considered.

In Figure 4.8 the two dimensional distribution of the S- and A-components are shown for JJA. On average the CPCSs have a median shift of -0.72 in the S-component which means there are smaller and/or more peaked precipitation objects in the CPCSs than in their parent simulations. For all models but MM5, this also means an improvement of the structure of precipitation objects in the CPCSs because the S-components are more centered on zero. Furthermore, the median A-components of the CPCSs are 0.15 higher than those of the 10 km simulations which leads to an average overestimation of precipitation in all CPCSs, because the A-components of the 10 km simulations (except those of M10_O) are close to zero. The combination of smaller S values and larger A values in the CPCS means that there is more intense rainfall from smaller and/or more peaked

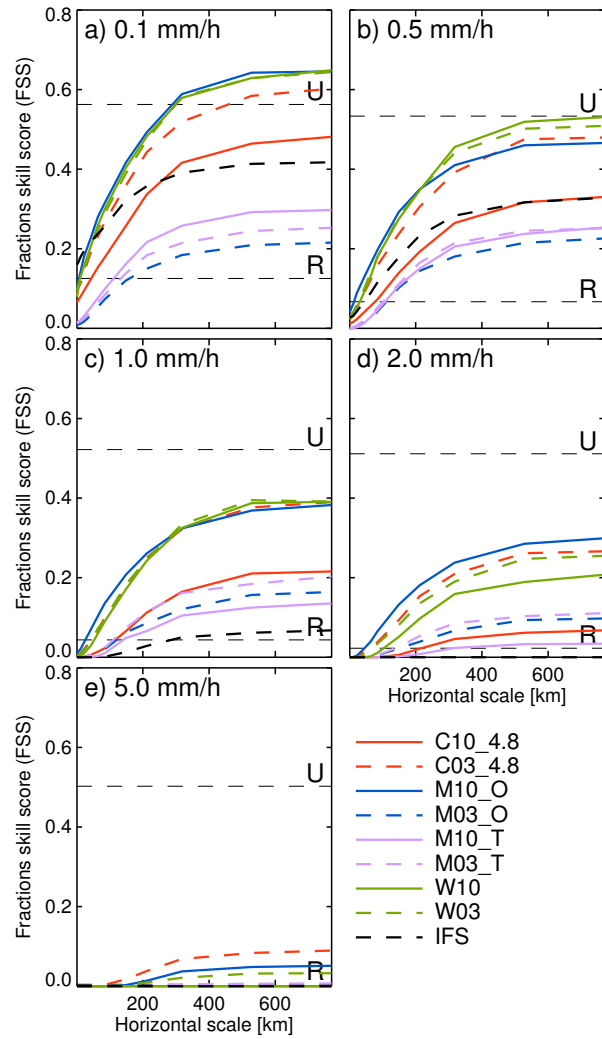


Fig. 4.6 Hourly median FSS of the JJA precipitation fields in D3. Different precipitation thresholds are depicted in each panel. A random simulation would have a FSS of R (lower dashed line) whereas reasonable skill can be assumed by values above the uniform (U, dashed line).

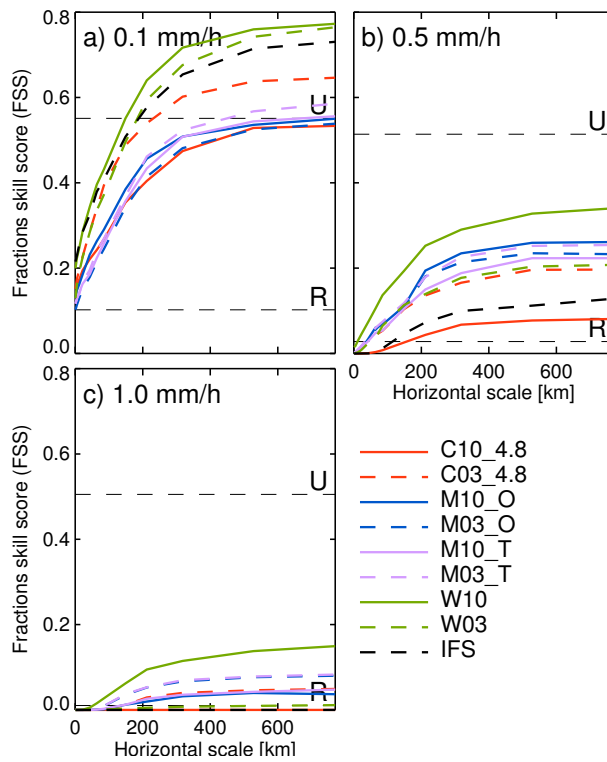


Fig. 4.7 Same as in Figure 4.6 but for DJF.

precipitation objects. Compared to IFS (Figure 4.8i) the RCMs are able to improve the S- and A-component of precipitation objects to a large extent. The contingency tables in the lower right corner of each panel reveals insights into the representation of correctly simulated precipitation (OJ/MJ), non-precipitation records (ON/MN), the amount of missed events (OJ/MN), and the amount of false alarms (ON/MJ) of each simulation. All CPCS (except MM5) show on average 23 % less missed events than their corresponding 10 km simulations. However, only the C03_4.8 simulation is also able to decrease the amounts of false alarms.

In DJF (Figure 4.9) the median S-components of the CPCSs are decreasing by -0.48 which leads to an improved structure of PR objects in all CPCSs (except for W03). The median A-components slightly increase in the CPCSs on average by 0.1. The RCMs are able to improve the S- and A-component of IFS (Figure 4.9i) even though IFS performs better than in JJA. The contingency tables show that the missed events in the CPCSs of MM5 and WRF are reduced by 13.6 % on average while they stay constant for CCLM 4.8. However, at the same time also the false alarms increase by 18 % in M03_T, and 67 % in W03. In case of M03_O they stay relatively constant and only the C03_4.8 simulation can reduce the false alarms by 25 %.

4.1 Added Value of Convection Permitting Seasonal Simulations

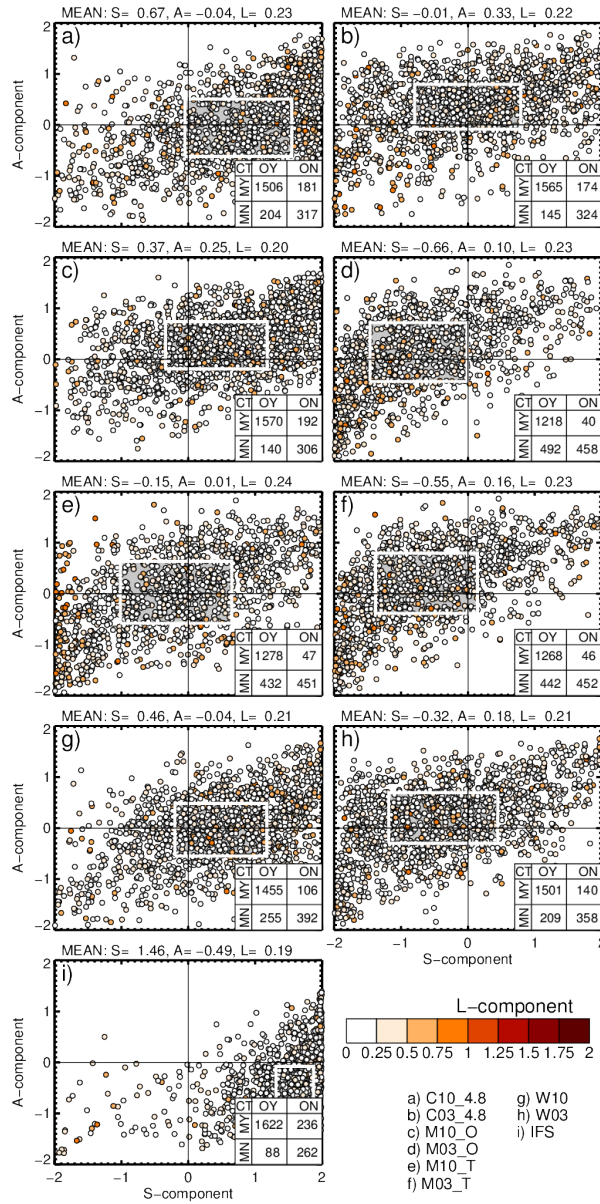


Fig. 4.8 Structure-Amplitude-Location evaluation diagrams for JJA in domain D3. The left column shows the results for the 10 km simulations (except panel i which depicts IFS) and the right column those of the CPCs. In rows there are CCLM_4.8, MM5OW, MM5TW, WRF, and IFS in top-down order. Each circle in the plot corresponds to one precipitation event. The colors of the circles depict the L-components. The median values of SAL are written above each panel and the box inside the plots shows the 25% to 75% quantile of the S- and A-components. In the lower right corner of the panels contingency tables are depicted. Therein OY denotes hours with PR in INCA, ON records without PR in INCA, MY records with PR, and MN records without PR in the simulations. The numbers in the table show the records where PR was simulated and observed (OY/MY), no PR was simulated and observed (ON/MN), PR was observed but not simulated (OY/MN), and no PR was observed but simulated (ON/MY).

4 Added Value in Convection Permitting Simulations

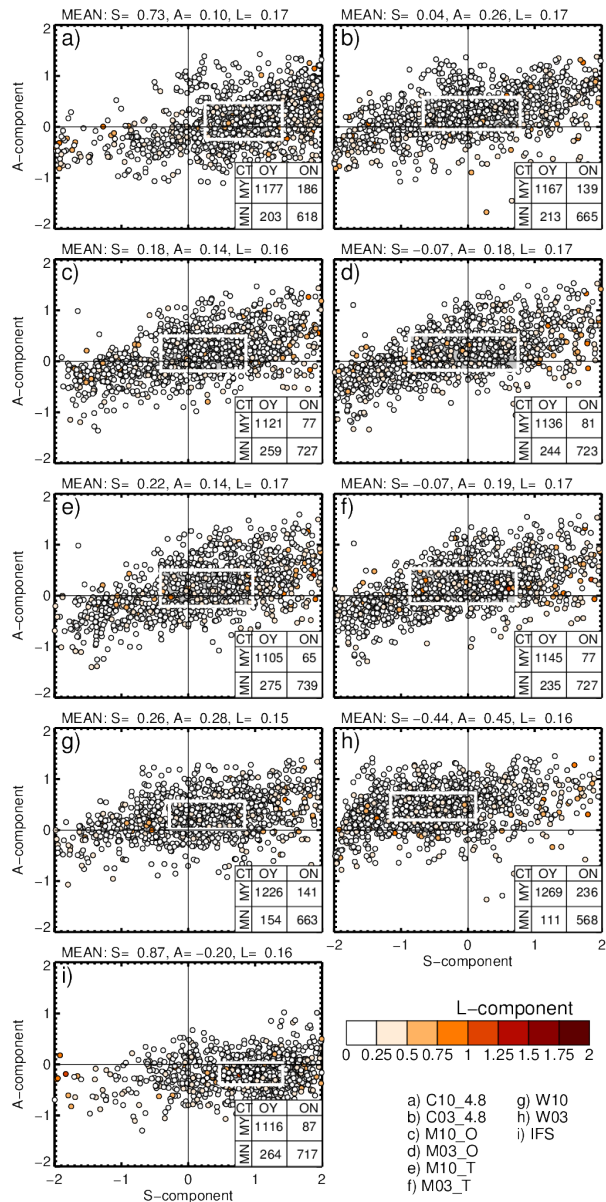


Fig. 4.9 Same as in Figure 4.8 but for DJF.

4.1.3 Discussion

In this subsection the results presented in Subsection 4.1.2 are discussed and interpreted. The main focus lies on the explanation and interpretation of consistent (common, model independent) differences between the CPCs and their parent simulations.

In order to investigate the effects of a higher resolved model orography more properly, a new MM5 simulation is introduced (M03_S). This simulation uses a smoothed 10 km orography while the rest of the model setup is the same as in the M03_O simulation (see Table 4.1). The smoothing of the 10 km orography with a 1–2–1 smoother is necessary to eliminate features of two-grid-interval wavelengths. Even though the orography of the M03_S and M10_O simulation are not identical, the slope angles, the mountain heights, and the elevation of the valleys are similar. The slope angles and vertical difference between valleys and peaks are important because steeper slopes and higher differences can initialize stronger vertical wind speeds and lift air more easily to the level of condensation and free convection. Therefore, comparing results from the M03_S with the M03_O simulation helps to separate the effect of better resolved orography from the effect of better resolved dynamics and deep convection in the CPCs.

4.1.3.1 Improved Representation of T2M

Figure 4.2 shows that spatial differences in the seasonal averaged T2M fields in JJA are commonly decreasing in all CPCs compared to their parent simulations. In DJF however, only the C03_4.8 and M03_O simulations show such an improvement. The main reason for this can be found in the improved representation of orography in the CPCs as shown in Figure 4.10.

In Figure 4.10 a the same data are shown as in Figure 4.2 a for M10_O, M03_O, and additionally for M03_S however, here a height correction of 6.5 K km^{-1} is applied to account for the height differences between model and the INCA orography. This height correction leads to a similar error range in all three simulations regardless of their grid-spacings and the underlying orography. Similar results can also be found for the other simulations (not shown).

In DJF (Figure 4.10 b), contrary to JJA, the application of a height correction does not remove but only decreases the error range differences. This is because the error ranges in the CPCs are increased. Especially positive differences are getting larger (e.g., the 75% quantile) because there is already an overestimation of T2M in the valleys in the CPCs (not shown) which gets even amplified by the height correction (the valleys in INCA are deeper than in the models which leads to an increase of T2M due to the height correction). The reason for the persistent differences compared to JJA might be related to the more stable stratification of the atmosphere (smaller temperature gradients) in DJF. This means height differences do not have such a strong influence as in JJA.

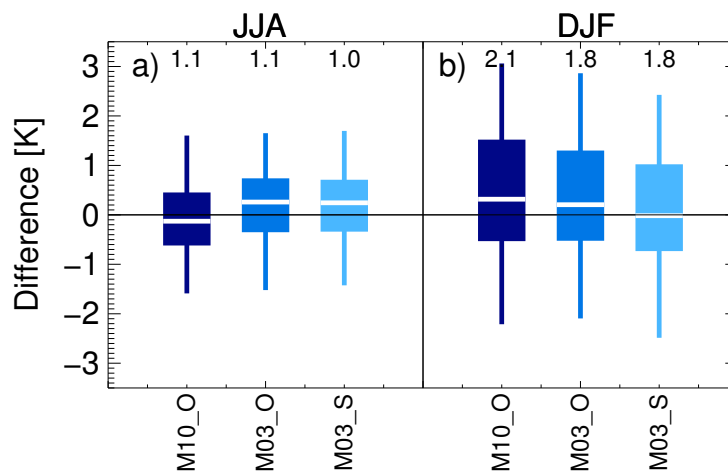


Fig. 4.10 Spatial differences of seasonal averaged T2M fields for three selected MM5 simulations depicted as box-whisker plots. The T2M fields include a correction based on a mean temperature lapse rate of 6.5 K km^{-1} . The left panel a depict results for JJA while the right panel b shows results for DJF.

Furthermore, inversions which are hard to simulate even with a 3 km grid-spacing model occur frequently during DJF. A worse simulation of inversions in the RCMs can lead to an overestimation of T2M in the valleys (in INCA the T2M in the valleys are well captured because of a high station density).

4.1.3.2 Improved Diurnal Cycle of PR in JJA

An improved onset of rising PR at noon and a better timing of the PR peak in the afternoon is shown for average JJA PR in the CPCs in Figures 4.3d and 4.3f. The reason for these improvements is the explicit treatment of convective PR and not the better resolved orography, as shown in Figure 4.11. By comparing the diurnal cycles of M10_O (solid blue line) with those of M03_O (dashed blue line) and M03_S (dotted blue line) the described improvements become visible. The convective (parameterized) part of PR in M10_O (red solid line) contributes more than 50% to the total PR (blue solid line) and shows a too early onset of increasing PR in the morning and a too early and peaked maximum in the afternoon. However, the resolved part of PR (orange solid line) has the correct onset and a later but rather weak peak in the afternoon. This is continued when the resolution is increased (M03_O and M03_S). Comparing the results of M03_O with M03_S, the resolution of the model orography has no effect on the improved timing of the diurnal cycle of convective precipitation. This indicates that the improvements in capturing the timing of convective PR is driven by the higher resolved atmospheric dynamics rather than the higher resolved orography.

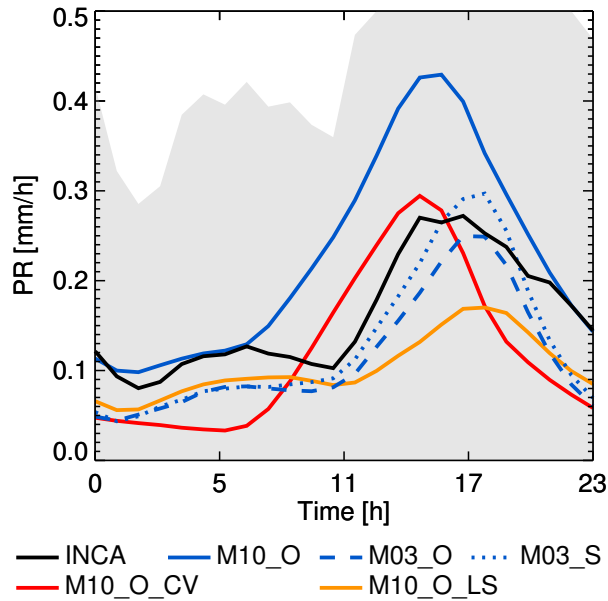


Fig. 4.11 Average JJA PR diurnal cycle in domain D3. The red line (M10_O_CV) shows the parameterized (convective scheme) part of the total precipitation in the M10_O (solid blue line) while the orange line (M10_O_LS) depicts the resolved part.

4.1.3.3 Improvements of Extreme PR

In Figure 4.5 an improvement of the most extreme precipitation rates in DJF (Figure 4.5 B) and especially JJA (Figure 4.5 b) in the CPCs is shown. Figure 4.12 depicts this improvement exemplarily for M03_O and M03_S and their parent simulation M10_O. In JJA (Figure 4.12 a), the maxima PR (Q100) is underestimated by approximately 60 mm h^{-1} in M10_O but only by approximately 33 mm h^{-1} in M03_O (the maximum in INCA is 85 mm h^{-1}). However, only a small part of this improvement can be attributed to the steeper orography in M03_O, because the M03_S simulation has a similar bias of approximately 36 mm h^{-1} as the M03_O. Figure 4.12 b shows the same data as 4.12 a, but here all fields are spatially averaged to the 10 km grid of M10_O. On this scale there is only a small difference in the Q100 PR between the CPCs and their parent simulation and also the differences to the maximum PR in INCA are much smaller. In addition, the Q95–Q100 differences show only minor changes. The reason for the improved extreme precipitation rates in Figure 4.12 b therefore relies on the fine spatial structures of such events, which are more properly captured by the model when the dynamics of the atmosphere is higher resolved.

In DJF (4.12 A), the differences between the M03_O and M03_S compared to the M10_O simulation are not as large as in JJA. Still there is an improvement in the Q100

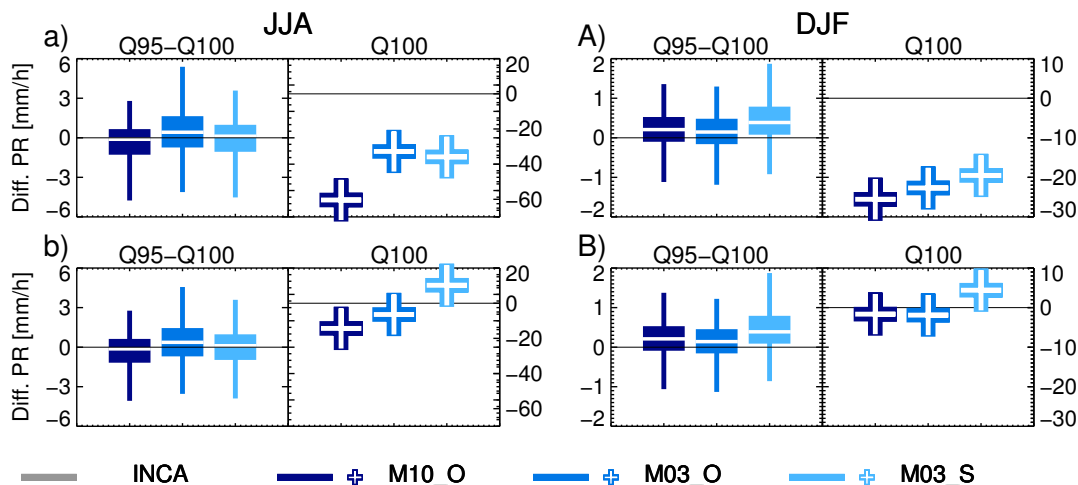


Fig. 4.12 Simulated minus observed quantile deviations (upper panels) for PR in JJA (left panels a and b) and DJF (right panels A and B) on D3. The upper panels (a and A) show results on the original grid-spacing while the lower panels (b and B) display the results averaged to the 10 km M10_O grid. The right quantile differences plot (labeled with Q100) shows the difference in the maximum of the hourly grid-point values (simulations minus INCA). The box-whisker plots show the differences between the 95th to 100th (Q95–Q100) quantile ranges.

difference in the CPCSs visible. Similar to JJA, also in DJF the evaluation on the 10 km grid (4.12 B) reveals that the underestimation of the maximum PR relies on the grid-spacing of the simulations and that it is nearly vanishing within an evaluation on a 10 km scale.

4.1.3.4 Improved Spatial Properties of PR

The more accurate spatial distribution of hourly rainfall in CPCSs, which is shown in the FSS evaluations in Subsection 4.1.2.4, is likely attributed to improvements in the deep convective dynamics during JJA and a more accurate representation of predictable local effects (e.g., orographic uplift). The results agree well with findings of Roberts and Lean (2008) and Weusthoff et al. (2010) even though some differences exist. Weusthoff et al. (2010) found highest improvements in the FSS of convection permitting simulations for lower precipitation thresholds whereas Roberts and Lean (2008) found them for higher thresholds similar to those in this study. Furthermore, improvements of scales on which simulations have more than random skill found by Roberts and Lean (2008) can only be seen in the C03_4.8 simulation.

The general more realistic structure of precipitation object (smaller and/or more

peaked) which was shown in the SAL evaluations in Subsection 4.1.2.4 is in good agreement with findings by Wernli et al. (2008) who compared high-resolution precipitation forecasts with coarser scale global model forecasts.

4.1.3.5 Increase of GL

In Figure 4.2 g and 4.2 h a consistent increase of GL in most CPCSs is depicted. This increase can be up to 20 % in JJA, is especially large in the two-way coupled simulations, and leads to changes in the surface energy budget (not shown). For instance, the additional energy increases the latent heat flux in W03 and M03_T simulation, while in the M03_O run the sensible heat is increased. In C03_4.8 both reactions occur, depending on the region. In this subsection atmospheric fields which are important for GL are investigated in JJA between 06:00 am and 06:00 pm.

To understand the reason for the increase in GL it is important to understand how the shortwave radiation is interacting with the atmosphere in the models. In the MM5 and WRF simulations the Dudhia 1989 short wave radiation scheme (D89) (Dudhia 1989) is used. Within this scheme a simple downward integration of solar flux is applied which knows three interaction mechanisms: (1) cloud albedo and absorption parameterized with the cloud liquid water (CLW), (2) water vapor absorption (Lacis and Hansen 1974), and (3) clear air scattering. In Figure 4.13 a the parameterized transmission coefficient of shortwave radiation and its dependency on CLW, as it is parameterized in the D89 scheme, is depicted. At CLW values below 10 g m^{-2} more than 90 % of the shortwave radiation can transmit while above 1000 g m^{-2} the transmission part is only 10 %. In the CCLM simulations the Ritter and Geleyn (1992) radiative transfer scheme (RG92) is used which is more complex than the D89 scheme. Solar radiation in the RG92 scheme interacts with cloud water droplets, cloud ice crystals, water vapor, ozone, and takes into account effects of Rayleigh scattering. In the RG92 scheme also partial cloudiness is treated by attributing two sets of optical properties and fluxes to each layer, one for the cloudy and one for the cloud free part (Geleyn and Hollingsworth 1979). Thereby, clouds in adjacent model layers have maximum overlap while clouds which are separated by cloud free layers are independent from each other (random overlap assumption).

A general feature in all CPCSs are the higher values of CLW above approximately 500 g m^{-2} compared to their parent simulations (all lines are above the diagonal in Figure 4.13 a). This means that already dense clouds become even denser in the CPCSs. This should not have a very strong effect on the GL values in the CPCSs because the transmission coefficients do not change a lot at these high values and the total amount of values higher than 500 g m^{-2} in the entire distribution is marginal (cf. Figure 4.13 c).

In case of the M03_T simulation, the number of low CLW values (smaller approximately 300 g m^{-2}) is higher than in the M10_T run (the violet line is below the diagonal

for small CLW values in Figure 4.13 a). Also the GL is increased (Figure 4.13 b) while the mean CLW stays constant (approximately 38 g m^{-2} Figure 4.13 c). However, the 75 % quantile (upper box) of CLW is clearly decreased (from 34 g m^{-2} to 2 g m^{-2}). This shifts the transmission coefficients towards higher values and supports the increase of GL. If one-way coupling is applied less CLW values below approximately 300 g m^{-2} occur in the M03_O simulation compared to the M10_O run (blue line is above the diagonal below approximately 300 g m^{-2}) and GL values are only slightly increasing (Figure 4.13 b). The boxes and whiskers of CLW are quite similar even though M03_O has a slightly higher mean and upper whisker value (Figure 4.13 c). The water vapor absorption is a function of the atmospheric water vapor (AWV) which stays the same in both, the CPCs and their parent simulations in MM5 (Figure 4.13 d). In the D89 scheme the clear air scattering is proportional to the atmosphere's mass path length and can therefore only be responsible for small changes in GL.

Considering those results the primary effect which causes changes of GL between the CPCs and the 10 km simulations of MM5 are changes in the low values (lower than approximately 200 g m^{-2}) of the CLW distribution because the gradient of the transmission curve is much larger and the large majority of CLW values are smaller than approximately 200 g m^{-2} (see Figure 4.13 c). This means that in M03_T there are larger fractions with “cloud free areas” compared to M10_T which directly leads to an increase of GL. Since the W03 and W10 are also two-way coupled and the D89 scheme was used in WRF as well, the reason for the increasing GL values might be similar. In M03_O an increase of the “cloud free areas” fraction is not visible compared to M10_O (because M10_O already has low CLW values) and therefore GL changes are small.

To investigate the reasons of the GL increases in CCLM the simulations of both versions (4.8 and 4.0) are considered because in the CCLM 4.8 runs no AWV and cloud area fraction (CAF) fields have been stored. The low CLW values (below approximately 500 g m^{-2}) are very similar in the C03_4.8 and C10_4.8 runs whereas C03_4.0 has clearly lower values than C10_4.0 (Figure 4.13 a). However, both show a similar median increase in GL (24 W m^{-2} in C03_4.0 and 28 W m^{-2} in C03_4.8) (Figure 4.13 b). In C03_4.0 the mean and the 75 % quantile (upper box limit) of the CLW is decreasing compared to C10_4.0 (Figure 4.13 c) while the mean is slightly increasing and the 75 % quantile is constant in the C03_4.8 run (compared to C10_4.8). There is more AWV in the C03_4.0 simulation than in the C10_4.0 run (Figure 4.13 d) and the median CAF decreases by 14 % (Figure 4.13 e).

Summing up, for C03_4.0 the increase of GL compared to C10_4.0 can be related to a higher “cloud free area” fraction indicated by increased low CLW values and decreased CAF (similar as in MM5). Changes in the cloud ice content cannot be investigated because cloud ice was not stored. The reason for the GL increase in C03_4.8 cannot be fully analyzed because of missing data.

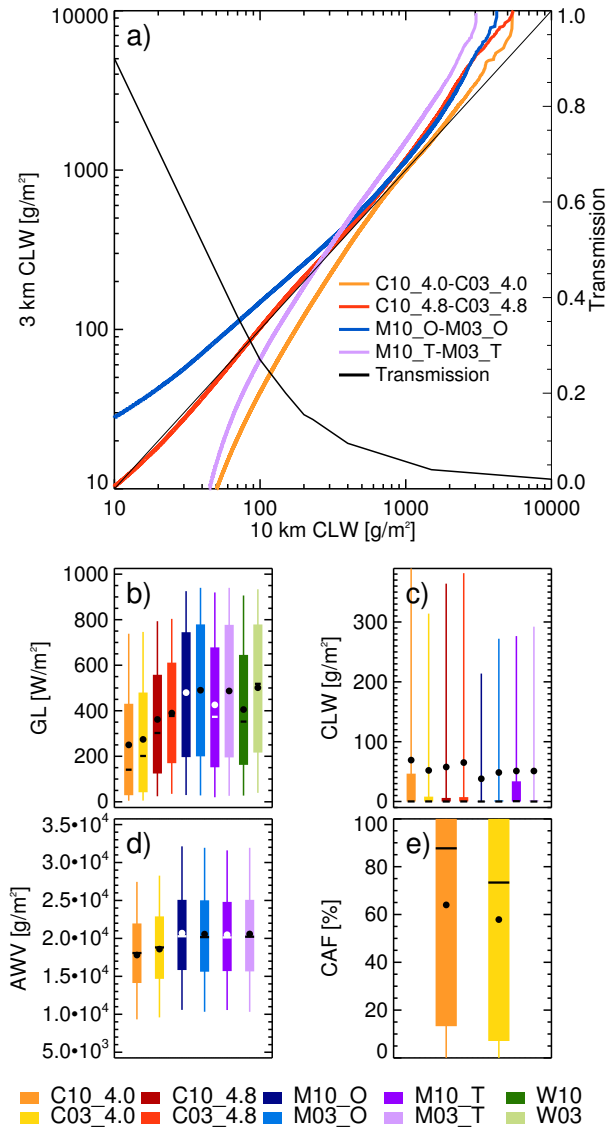


Fig. 4.13 Panel a shows a quantile-quantile plot of cloud liquid water from the 10 km (x-axis) and 3 km simulations (left y-axis) on D3 for hourly grid-point values between 06:00 am and 06:00 pm in JJA. The secondary y-axis gives the shortwave transmission coefficient depending on CLW as it is parameterized in the MM5 and WRF simulations for a solar zenith angle of 37° and zero surface albedo (Stephens 1978). The box-whisker plots below (panels b to e) show hourly grid-point values for GL (panel b), integrated CLW (panel c), AWV (panel d), and CAF (panel e) between 06:00 a.m. and 06:00 p.m.. The dots show the arithmetic mean values of the distributions. Note, not all parameters are available for every simulation.

4.1.3.6 Two-way vs. One-way Coupling

If two-way coupling is applied the atmospheric fields in the 10 km simulation are overwritten by the values of the CPCS within the area of the 3 km nest. This means that the 3 km run is compared to a coarser (smoothed) version of itself. On the other hand, also one-way coupled CPCSs are often more similar to their corresponding 10 km simulations than to the observations (except for precipitation) or to CPCS of other RCMs. This indicates that a large part of the errors in CPCS comes from the RCM formulation, the RCM setup, or from the LBCs of the CPCSs. The small domains in the CPCSs are contributing to this behavior (see Subsection 4.1.3.8). Comparing the one-way coupled M03_O simulations with the two-way coupled M03_T run shows that in this study the benefit of two-way coupling is rather small because the results of both simulations are very similar.

4.1.3.7 Added Value in the Sub-regions and Seasons

Detecting added value is generally easier in the mountainous region D4b than in the hilly area of D4a because of the high impact of better resolved orography in complex terrain. For instance, this can be seen in the improvements of the JJA precipitation diurnal cycle where no diurnal cycle is visible in D4a (Figure 4.3 e) whereas a strongly amplified cycle is visible in D4b (Figure 4.3 f). Furthermore, improvements in the seasonal mean T2M fields are much stronger in D4b than in D4a because of the large improvements of the complex orography in D4b.

Added value is additionally easier to find in JJA than in DJF mainly because of the more accurate representation of convective processes during the hot season and the well mixed conditions in the troposphere. Furthermore, in DJF the large-scale flow is more dominant than in JJA which reduces the influence of small-scale processes.

4.1.3.8 Domain Size

A notable limitation of this study are the relatively small sizes of the 3 km simulation domains (see Figure 4.1) which have an East-West/North-South extension between approximately 580 km/approximately 510 km (in C03_4.0) and approximately 440 km/approximately 370 km (in M03_O, M03_T, and W03). This implicates that the boundary conditions from the 10 km simulations have a strong influence on the CPCSs, especially in situations with strong synoptic scale weather patterns (e.g., passages of cold fronts) which occur more frequently in DJF. In such situations the CPCSs have only a limited degree of freedom and are strongly determined by the solution of their parent simulations. In larger domains the differences between the CPCSs and their parent simulations might be more amplified.

4.2 Importance of Grid-Spacing for Simulating Precipitation Extremes

Because the results from the above study in Section 4.1 show high potential for an improved representation of heavy precipitation in CPCs compared to coarser gridded simulations the simulation of precipitation extremes is investigated in more detail. Since heavy precipitation events are typically rare events longer time periods than in Section 4.1 have to be investigated to be able to get statistically robust results. Therefore, the eight year period 2001 to 2008 is simulated with three different grid-spacings of 4 km, 12 km, and 36 km over the headwaters of the Colorado River (hereafter: Colorado Headwaters). These simulations enable to investigate a sample of heavy precipitation events which makes a statistical evaluation of such events possible. The focus lies on events in DJF and JJA because heavy precipitation events in these seasons have typically different synoptic-scale forcing and meso-scale processes. In March, April, and May (MAM) and September, October, and November (SON) a mixture of DJF and JJA types of heavy precipitation events can occur. Analyses from these transitional seasons are briefly described in Subsection 4.2.2.6.

An important difference to the first study is the applied nesting strategy. While in the first study a two step nesting strategy was used (the outcome of first step 10 km grid-spacing simulations were used as LBCs for the 3 km CPCs) here all three simulations were forced with exactly the same LBCs over a common domain (the headwaters of the Colorado River). This has the advantage that errors in the coarse resolution 36 km simulation are not propagating into the finer resolved runs via the LBCs. This means the simulations are independent from each other which is beneficial for the detection and attribution of differences between them. Furthermore, in this study the computational domain is much larger and the evaluation domain is further apart from the lateral boundaries which also is advantageous.

The main research questions are:

1. What is the effect of grid-spacing on the representation of heavy precipitation events in the Colorado Headwaters?
2. On which spatial scales do differences occur?
3. Which grid-spacing should be used to simulate heavy precipitation events?

4.2.1 Experimental Setup, Data, and Models

The simulations were performed with the WRF model version 3.1.1 (Skamarock et al. 2008) for an eight-year period from January 1st 2001 to December 31st 2008 (plus three months of spin-up) by the Colorado Headwaters research group at the National Cen-

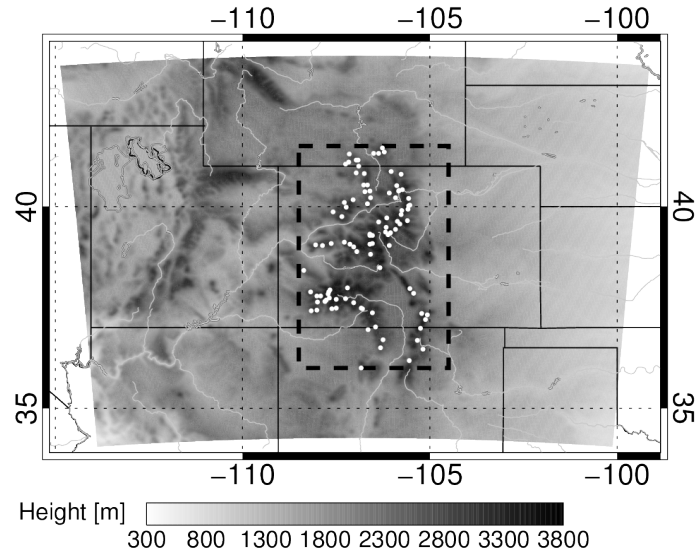


Fig. 4.14 The shading shows the orography in the model domain. The Colorado Headwaters are highlighted in the black dashed rectangle. White dots show the location of SNOTEL stations.

ter for Atmospheric Research (NCAR) (Rasmussen et al. 2011). Three single domain simulations with horizontal grid-spacing of 4 km (WRF4), 12 km (WRF12), and 36 km (WRF36) (Figure 4.14) were performed. Compared to the two step nesting strategy in the previous study (see Subsection 4.1.1) the here used setup leads to simulations which are independent from each other and are performed within a common computational domain. The initial conditions and three-hourly lateral boundary forcing are derived from the 32 km North American Regional Reanalysis (NARR) (Mesinger et al. 2006). The domain and model setup are the same as in Ikeda et al. (2010); Rasmussen et al. (2011); Liu et al. (2011). While deep convection was parameterized in the 12 km and 36 km simulation using the Betts–Miller–Janjić scheme (Betts and Miller 1986; Janjić 1994), no convective parameterization was used in the 4 km simulation because deep convection is partially simulated at this grid spacing (Weisman et al. 1997). Still properties like maximum vertical velocities are underestimated even in simulation with a 4 km grid (Weisman et al. 1997). However, Langhans et al. (2012) demonstrated that in simulations with 4.4 km, 2.2 km, 1.1 km, and 0.55 km horizontal grid-spacing bulk flow properties like heating or moisture tendencies but also precipitation are converging and are nearly resolution independent.

The evaluation of simulated heavy precipitation events is conducted in the Colorado Headwaters region (the area inside the dashed rectangle in Figure 4.14) using shielded weighing precipitation gauges at 99 stations within the SNOTEL (white dots in Fig-

ure 4.14) network (Serreze et al. 1999). All 99 stations have a complete record of daily precipitation for the entire period 2001 to 2008. The stations are located in the region with highest snowpack (between 2400 m and 3500 m above mean sea level) in forest clearings. The SNOTEL precipitation gauges have a resolution of 2.5 mm. The largest error source of weighing type gauges is the undercatch of snowfall due to wind (Serreze et al. 1999; Yang et al. 1998; Rasmussen et al. 2012). This error might be especially large for heavy precipitation events that typically occur with strong wind. However, the forest clearing in which SNOTEL gauges are typically located reduce the wind speed to less than 2 m s^{-1} , leading to underestimate of snowfall by only 10 % to 15 % (Rasmussen et al. 2012). For comparisons of SNOTEL observations with model precipitation, the model values at four nearest grid-points around each station are weighted with inverse-distance averaging. In addition to the SNOTEL observations, the Climate Prediction Center (CPC) precipitation dataset (Higgins et al. 2000) and the NARR precipitation are used for comparisons.

In this study, heavy precipitation events are defined as events above the 97.5th percentile of daily domain-averaged total SNOTEL precipitation within the 8-year period 2001 to 2008. Compared to the 30-year period 1980 to 2010 in DJF four of the ten most extreme events occurred within 2001 to 2008 including the two most extreme events (the 30- and 15-year event in terms of return level in 1980 to 2010). In JJA two of the ten most extreme events occurred in the simulated period which are the 7.5- and 3.75-year event in 1980 to 2010. Selecting events above the 97.5th percentile leads to a sample of heavy precipitation events which consists of the 18 most intense precipitation days in each season within 2001 to 2008. The selection of heavy precipitation events from SNOTEL observations means that only events at high altitude are investigated. A selection based on valley stations may lead to a different set of events.

4.2.2 Results and Discussion

4.2.2.1 Spatial Patterns of Mean Heavy Precipitation Events

Figure 4.15 displays the average of the heavy precipitation sample in the Colorado Headwaters in DJF (upper panels a–d) and JJA (lower panels e–h). In DJF domain average precipitation measured at SNOTEL stations (panel a) is more than twice as high than JJA precipitation (panel e). Also the spatial patterns differ. In DJF (Figure 4.15 a) the precipitation maximum is located in the south-western part of the Colorado Headwaters because in this season heavy precipitation is typically associated with a south-westerly flow bringing moist air from the Pacific. In JJA where typically situations with weak synoptic-scale forcing lead to strong precipitation the heaviest precipitation occurs in the north-eastern part of the Colorado Headwaters (the Front Range Mountains; Figure 4.15 e).

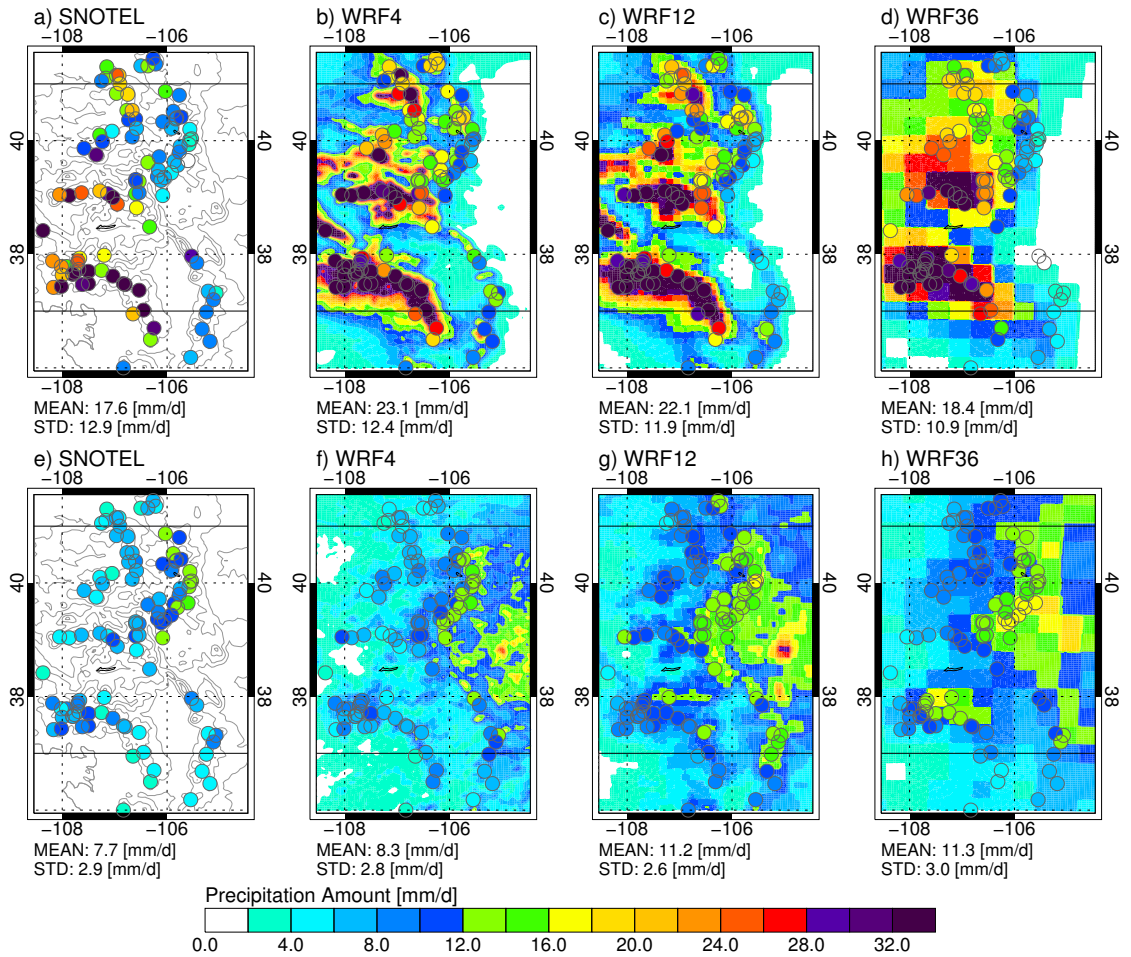


Fig. 4.15 Average heavy precipitation (events above the 97.5th percentile) in the Colorado Headwaters in DJF (upper panels a–d) and JJA (lower panels e–h). SNOTEL observations are displayed in the first column followed by WRF4, WRF12, and WRF36 simulations (from left to right). Below each panel the spatial mean and standard deviation (STD) are displayed for precipitation values at SNOTEL sights.

Comparing the simulations, in DJF smaller grid-spacings lead to more precipitation while in JJA the opposite is true. In DJF there are only approximately 3% of total precipitation convective induced in the WRF12 and WRF36 simulation which means that there is only a small amount of precipitation coming from the convection parameterization. In this season the higher precipitation values in simulations with smaller grid-spacings are probably due to the improved representation of meso-scale orographic forcing (Ikeda et al. 2010; Rasmussen et al. 2011). In JJA the convective precipitation amounts for 62% in WRF12 and 69% in the WRF36 simulation (compared to zero in the WRF4 simulation) which contributes to the overestimation of heavy precipitation in this season. A more detailed analysis of differences between observed and simulated precipitation events is given in Subsection 4.2.2.3.

4.2.2.2 Power Spectra

Figure 4.16a illustrates the median power spectra of the 18 simulated DJF heavy precipitation events, the spectra of the model topography and those of the CPC and NARR dataset. The spectra are derived via the discrete cosine transformation (DCT) which is described in Subsection 3.2.2.2 and Denis et al. (2002[a]).

Most variance can be found in the large-scales (high wavelengths). Clearly visible is the strong relationship between the spectra of the simulated events and those of the orography. This shows the strong relationship of precipitation to orographic uplift in the region in DJF. The spectra of the 4 km and 12 km simulations start to diverge at wavelengths smaller than approximately 50 km (clearly for DJF) where the 4 km simulation has higher variability. This spatial scale indicates the effective resolution of the 12 km run which is approximately four times its grid-spacing. The same ratio can be seen for the 36 km simulation, and similar results were found for WRF kinetic energy spectra by Skamarock (2004). The CPC spectrum agrees fairly well with the simulated spectra. The NARR spectrum shows a lower variability than the other spectra.

In JJA (Figure 4.16b) the relationship between the spectra of the orography and those of the simulated events is much weaker than in DJF. This is because the heaviest DJF precipitation occurs typically near to mountain slopes where strong upslope winds exist whereas heavy JJA precipitation originates from deep convection which can be induced by upslope winds but is not restricted by the location of mountain slopes. Between approximately 50 km to approximately 170 km the 12 km run and between approximately 80 km to approximately 300 km the 36 km simulation has higher variances than the 4 km run which is probably caused by the convection parameterization in the coarser models. As in DJF also in JJA the spectra of the CPC dataset fit very well to the simulations whereas the variances in the NARR spectrum are lower.

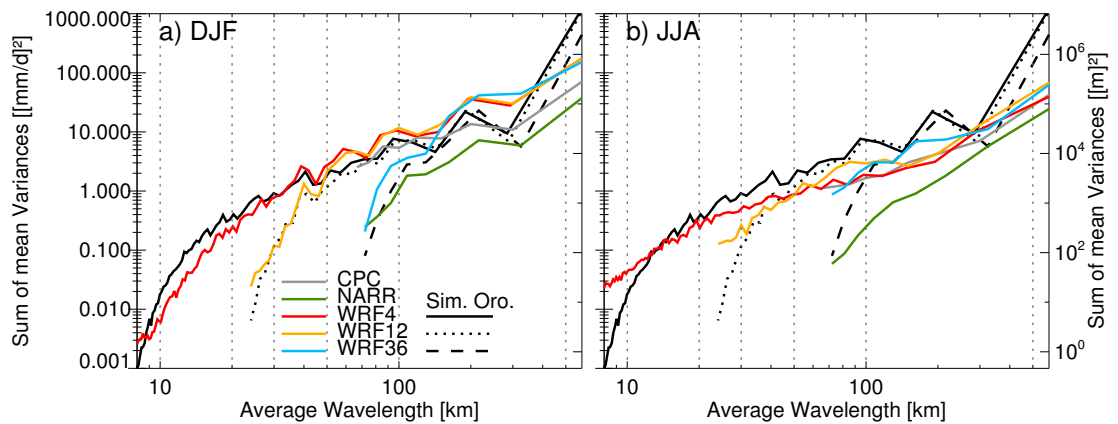


Fig. 4.16 Variance spectra from the DCT of the median heavy precipitation events (events above the 97.5th percentile) in (a) DJF and (b) JJA. The spectra of the orography in the simulations (Sim. Oro.) are shown as black solid, black dotted, and black dashed lines for the 4 km, 12 km, and 36 km models, respectively. Both axes are logarithmically scaled.

4.2.2.3 Spatial Differences

Relative differences between the averaged 18 events (simulated minus observed) in DJF are depicted in Figure 4.17 a–c for the 4 km, 12 km, and 36 km simulations. During this season all simulations tend to overestimate heavy precipitation in the northern part of the domain. The overestimation is also larger at low elevated stations and tends to get smaller above approximately 3200 m. Precipitation differences increase with resolution but the root-mean-square-errors (RMSEs) decrease because absolute differences get smaller.

In JJA (Figure 4.17 d–f), the 4 km simulation is clearly more robust in terms of average difference, RMSE, and spatial patterns compared to the coarser resolution simulations which tend to overestimate heavy JJA precipitation. Differences of individual events are additionally less spread in the 4 km run which means that not only the median but also single events are better represented compared to the coarser simulations. There is no clear zonal, meridional, or height dependency in the differences.

4.2 Importance of Grid-Spacing for Simulating Precipitation Extremes

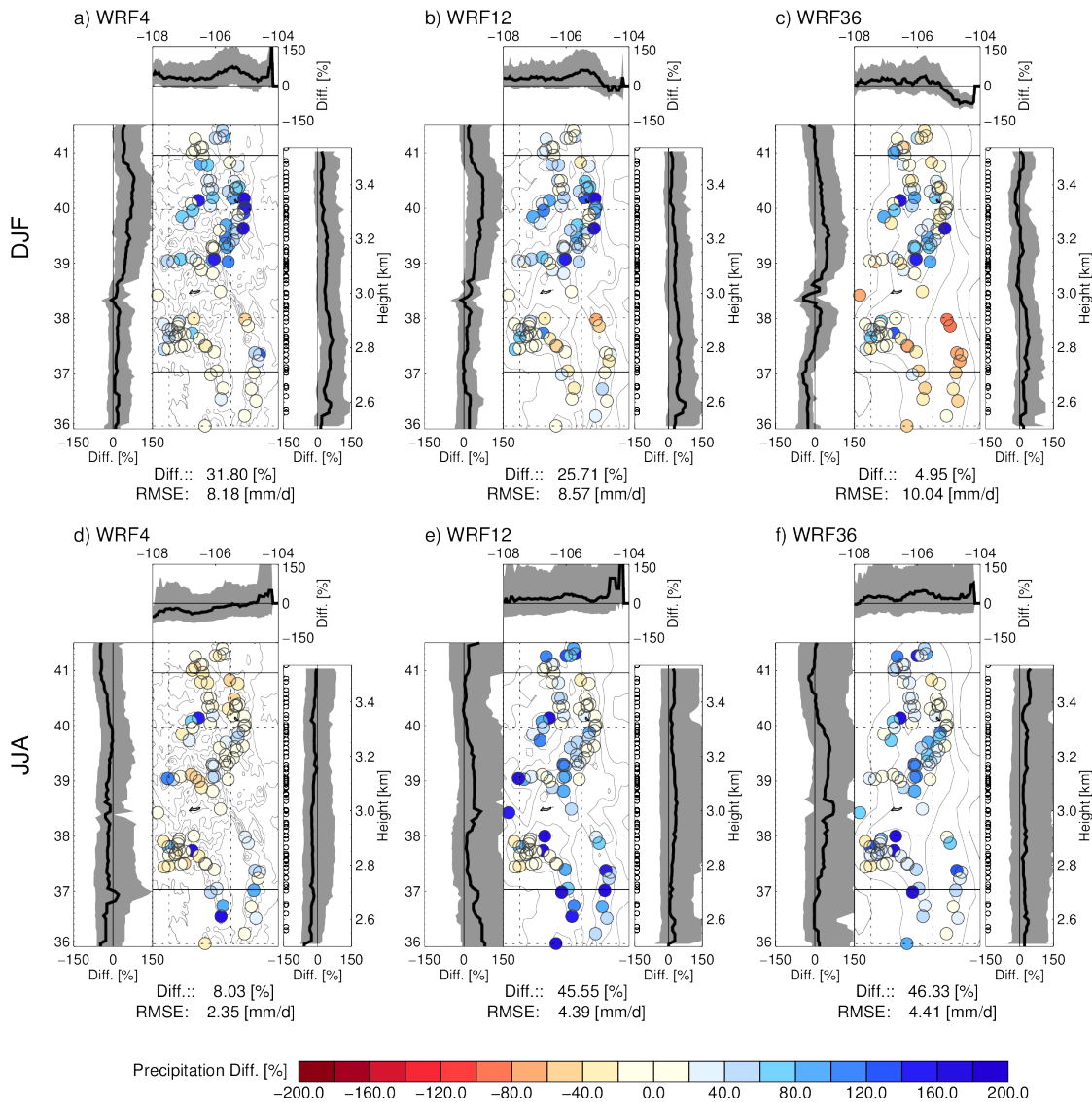


Fig. 4.17 Spatial distribution of relative differences (simulation minus observation) between simulations and SNOTEL for the average heavy precipitation events (events above the 97.5th percentile) in DJF (upper panels) and JJA (lower panels). WRF4, WRF12, and WRF36 are shown from left to right. The map in the middle panel shows the spatial distribution of the differences over the Colorado Headwaters. The left sub-panel attached to each map shows the meridional difference along the latitude (moving average for all stations within $\pm 0.4^\circ$), the upper sub-panel the zonal difference along the longitude, and the right sub-panel those for elevation (± 200 m). The SNOTEL site elevations are shown as black circles in the right (elevation) sub-panels above the approximately 150% marker. Solid black lines show the average differences. The gray shaded areas depict the 25 to 75 quantile spread of differences from single events. The average difference and RMSE difference for the entire domain are written below each panel.

4.2.2.4 Scale Dependent Analysis

In this subsection the spatial Pearson correlation coefficients (CCs), normalized standard deviations (NSDs), and RMSEs of the simulated, CPC, and NARR data are evaluated for a range of horizontal scales as described in Subsection 3.2.2.2.

In DJF the highest median CCs can be found for the 4 km simulation on its original grid (Figure 4.18 a). At their resolved scales the 12 km and 4 km simulations have very similar CCs whereas, the 36 km run has slightly lower CCs and larger sample variabilities. The CPC data have higher CCs than the simulations below approximately 90 km while the NARR dataset has lower values on all scales. Similar results can be found for the NSDs (Fig 5b). The 4 km simulation has closest values to one at scales below 12 km and very similar values to the 12 km run afterwards. The 36 km run has generally higher median NSDs, while the CPC and NARR data show lower values. The smallest RMSEs in the 4 km simulation show robustness especially at scales larger than 50 km (Figure 4.18 c). All simulations are improving the RMSEs of the NARR driving data.

The median CCs in JJA are generally smaller and the sample spread larger compared to DJF (Figure 4.18 d). This is probably due to the stochastic nature (non-linear interactions between land-atmosphere, cloud-cloud and/or cloud-radiation that can grow upscale, particularly under generally weak synoptic forcing in JJA) of convective precipitation. At scales from 12 km to 60 km, the 12 km run has higher CCs than the 4 km simulation. CPC and NARR have higher CCs below approximately 120 km. The 4 km simulation has high NSD below 12 km and similar to the 12 km simulation and CPC afterwards (Figure 4.18 e). Below 100 km, the 36 km run clearly has higher variability than the finer grid datasets. The sample spread of NSDs is smallest for the 12 km simulation above 20 km. The best RMSEs and smallest sample variability below approximately 100 km are achieved with the 4 km model (Figure 4.18 f). Smallest RMSEs can be found in the CPC dataset whereas the NARR RMSEs are similar to the simulations.

4.2.2.5 Spatial Similarities and Dissimilarities

Figure 4.19 shows median correlograms and variograms from the WRF simulations, CPC, NARR, and SNOTEL observations. For details about the method see Subsection 3.2.2.2.

All simulations show median CCs that are larger than SNOTEL at scales below approximately 70 km in DJF (Figure 4.19 a). Some of these differences may be due to measurement errors at the SNOTEL sites. Below 70 km the 4 km run is most similar to the SNOTEL sites. At scales larger than approximately 70 km the correlations of the 4 km and 12 km simulations start to match the SNOTEL observations; whereas the 36 km run has too high correlations until approximately 120 km. The correlation between pairs of stations becomes anticorrelated at approximately 190 km which is the typical scale of a

mountain range in the Colorado Headwaters (see also the peak in Figure 4.16). The CCs of NARR and CPC are similar to those of the WRF12 simulation. The DJF variogram (Figure 4.19b) shows weaker variability in all simulations at scales below approximately 70 km than SNOTEL. The 4 km simulation shows the most realistic spatial variability at all scales while the NARR and CPC data have the lowest variability.

In JJA (Figure 4.19c), CCs at small scales are generally lower than in DJF because of the higher spatial variability and smaller size of convective precipitation cells (anticorrelation starts at approximately 110 km). All simulations have higher CCs than SNOTEL at scales below approximately 100 km. The 4 km simulation performs best at these scales while above approximately 100 km all simulations begin to match the SNOTEL observed CCs. For scales above approximately 260 km all simulations except the 4 km model generate stronger anti-correlations than SNOTEL. The CPC CCs are similar to those of the WRF12 simulation while the NARR fit more to those of the WRF36 run. Variability in all simulations is lower than those of SNOTEL in JJA (Figure 4.19d). At scales below approximately 110 km the 4 km simulation has the closest correspondence with observations, and at larger spatial scales the 36 km run matches the 4 km simulations. As in JJA variances are lowest in the CPC and NARR dataset.

4.2.2.6 Analyses of MAM and SON Heavy Precipitation

In the transition seasons MAM and SON heavy precipitation can arise from a mixture of DJF (large-scale frontal system) and JJA (air-mass thunderstorm) types of storms. The mean precipitation of the SON and MAM heavy precipitation sample (12.3 mm d^{-1} in MAM and 14.8 mm d^{-1} in SON) is higher than the mean in JJA but lower than those in DJF. Also the convective part of the total precipitation in the WRF12 and WRF36 runs is with approximately 12% in MAM and approximately 33% in SON between the percentage in DJF and JJA (see Subsection 4.2.2.1). The highest observed precipitation values in MAM are in the north-eastern part of the domain (similar to JJA) and in SON in the south-western part (similar to DJF). In both seasons the domain total heavy precipitation is increasing with decreasing grid-spacing (similar to DJF). The lowest RMSEs are found in the WRF4 simulation followed by the WRF12 and WRF36 runs. In MAM and on small scales in SON the WRF4 simulation has higher CCs than the coarser simulations. The correlogram and variogram analyses lead to similar conclusions as those in JJA and DJF. The WRF4 simulation resembles correlations from SNOTEL observations best at scales below approximately 100 km and has most realistic variances on larger scales.

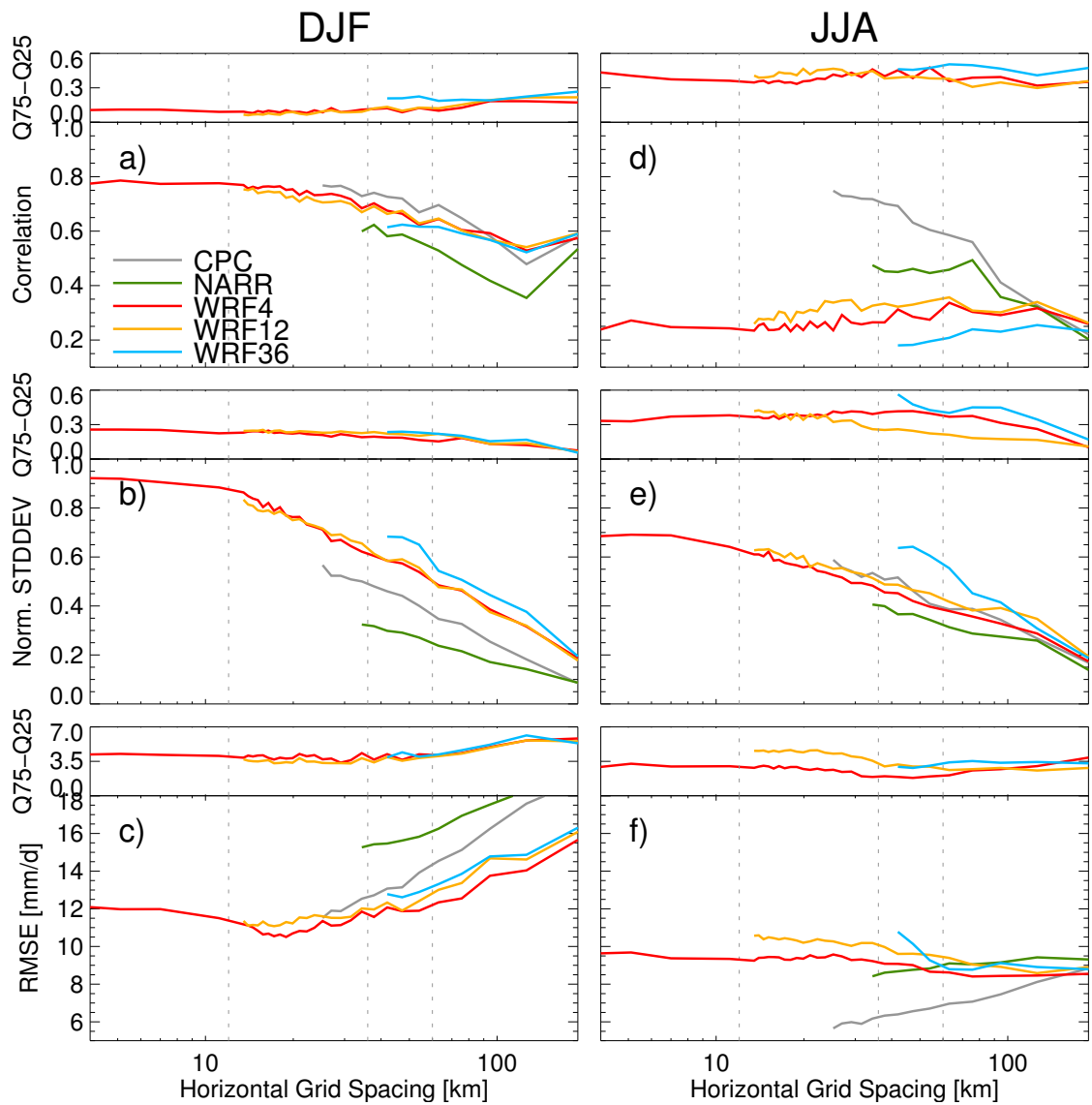


Fig. 4.18 Heavy precipitation (events above the 97.5th percentile) median correlation coefficients (top), normalized standard deviations (middle), and root-mean-squared-errors (bottom) for different horizontal grid-spacings of the WRF simulations together with CPC and NARR for DJF (left panels) and JJA (right panels) evaluated against SNOTEL data. The inter-quartile differences between the 75th and 25th percentiles (Q75–Q25) of the heavy precipitation event sample are depicted above each panel. Values on the x-axis are logarithmically scaled.

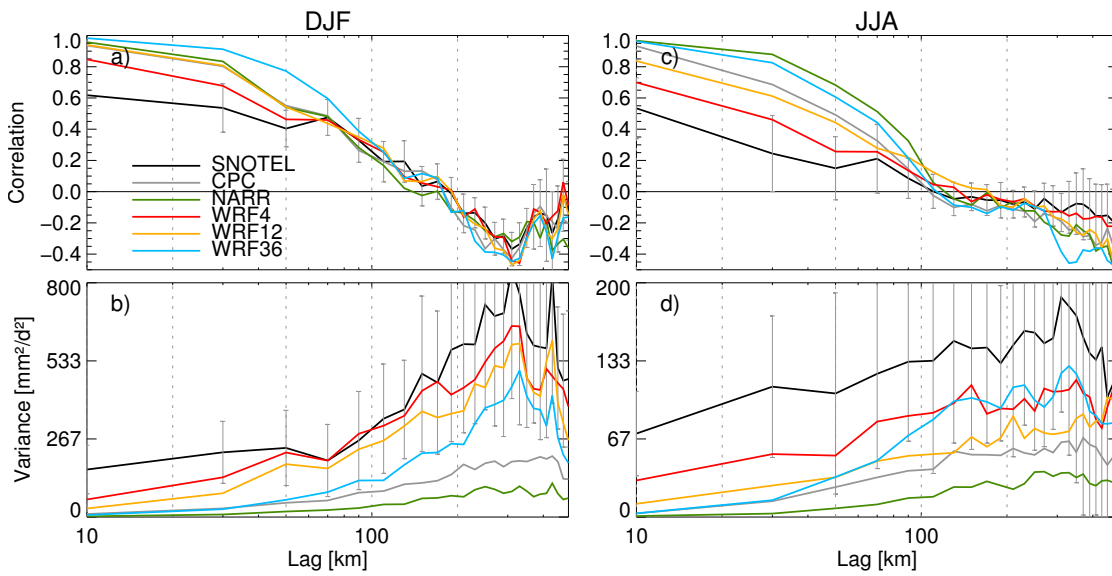


Fig. 4.19 (Top) Heavy precipitation (events above the 97.5th percentile) median correlograms, and (bottom) variograms for DJF (left panels) and JJA (right panels). The gray error bars depict the one fold standard deviation of the SNOTEL events. Values on the x-axis are logarithmically scaled.

5

Summary and Conclusion

THE basic research question of this thesis is if and where added value in convection permitting climate simulations (CPCSs) compared to coarser gridded simulations can be found.

Answering this question demands for the definition of statistical metrics which enable a comparison of simulations with different grid-spacings and which account for the special problems of evaluating highly resolved datasets. Finding such metrics was a central part of this thesis which is reflected in the numerous introduced (Section 3.2) and applied (Chapter 4) methods which can be regarded as a best practice example for searching and detecting added value in CPCSs.

Two main studies have been performed in this thesis. The first one focuses on the robustness of added value in an ensemble of three non-hydrostatic regional climate models (RCMs). The second one builds up on the findings of the first study and investigates scale dependent differences in the simulation of heavy precipitation events.

In the first study (Section 4.1) two seasons (June, July, and August (JJA) 2007 and December, January, and February (DJF) 2007 to 2008) are simulated with three different RCMs. Five simulations are conducted with a horizontal grid-spacing of approximately 10 km and five with approximately 3 km (CPCSs without deep convection parameterization) over the Eastern European Alpine region. Four atmospheric parameters (air temperature two meters above surface, precipitation amount at surface, relative humidity two meters above surface, and global radiation at surface) are evaluated which enables a holistic view on the RCM performance.

The second study (Section 4.2) focuses on the representation of heavy precipitation events in a CPCS and two coarser gridded simulations. It extends the first study by the length of the simulation period which is January 2001 to December 2008. This enables a statistically robust evaluation of heavy precipitation events. The Weather Research and Forecasting Model (WRF) was used to perform simulations with grid-spacings of 36 km, 12 km, and 4 km. In the last one deep convection is assumed to be explicitly resolved. The focus region of this study is the headwaters of the Colorado River.

The largest changes between simulations with and without convection parameterizations can be found in the representation of precipitation. Typically, the average amount of precipitation (but also averages of temperature, relative humidity, and global radiation) in a region is not improved in CPCS (cf., Figure 4.2) even though in some cases improvements can be found (e.g., JJA heavy precipitation events in the Colorado Headwaters; Figure 4.17 d–f). This is because most variance and spatial information in precipitation fields can be found in the large-scale patterns (cf., Figure 4.16). Thereby, precipitation patterns of CPCSs tend to converge towards patterns of coarser gridded simulations on scales larger than approximately 100 km (cf., Figures 4.16 and 4.19 a and c) meaning that typically most of the improvements in CPCSs get averaged out on large-scales.

Added value is therefore easier to find on small scales. In particular, CPCSs outperform coarser resolution simulations by producing spatially more independent and variable heavy precipitation fields at scales below approximately 100 km which agree well with observations. Similar to spatial averaging also temporal averaging tends to reduce the visibility of added value of CPCSs. According to the findings above, added value in CPCSs can typically be found at small scales (smaller than approximately 100 km) and on sub-daily (e.g., hourly) basis. One exception for this are the error ranges of air temperature two meters above surface which are strongly related to the better resolved orography in mountainous regions (Figure 4.2 a).

A very robust added value of CPCSs is the improved timing in the onset and peak of convective induced afternoon precipitation in mountainous regions during JJA (see Figure 4.3). This is in line with findings of Hohenegger et al. (2008) and Kendon et al. (2012). In addition to those temporal aspects the intensity of the most intense precipitation extreme events is improved (see Figure 4.12). The fractions skill score (FSS) analysis shows that added value is more apparent at medium to higher, than in low intensities (cf., Figure 4.6) and Structure-Amplitude-Location (SAL) evaluations reveal that most CPCSs represent spatial patterns of precipitation objects more realistically (smaller and more peaked; see Figures 4.8 and 4.9). It could be demonstrated that these improvements are caused by explicitly resolved deep convection and the better represented atmospheric dynamics, rather than by the better resolved orography (see Figures 4.11 and 4.12). In general, orography has a weaker influence on convective precipitation patterns than on large-scale patterns (cf., Figure 4.16). For DJF grid-spacings of at least

12 km are needed to simulate spatial patterns of heavy precipitation which are comparable to those in the CPCS and observations in the Colorado Headwaters (see Figures 4.17 and 4.19 b). In the European Alps this might be different because of the typically steeper slopes and narrower valleys compared to the U.S. Rocky Mountains.

Larger differences between CPCSs compared to their forcing simulations (which are not necessarily improvements), are found in the surface energy balance. This is caused by a general increase of global radiation at surface in all CPCSs (on average 11.5 % in JJA and 3.5 % in DJF; see Figure 4.2 g and h) which can be mainly attributed to an increase of areas with low integrated cloud liquid water content and/or a decrease of the cloud area fractions (in the case of COSMO model in CLimate Mode). The RCMs react very differently to this additional energy input and partly large changes in the sensible or latent heat fluxes occur.

Concluding, CPCSs show promising results to improve state-of-the-art climate simulations especially by explicitly resolving deep convection in the atmosphere. Nevertheless, they are computationally very demanding and therefore the choice of horizontal grid-spacing for RCMs depends on the underlying question.

If the main interest is the accurate representation of climate average, large-scale fields (e.g., on the scale of the European Alps or the Colorado Headwaters), even 36 km grid-spacing can be sufficient in SON, DJF, and MAM. This is not true for JJA when deep convective processes are predominant in northern hemisphere mid-latitudes. Improvements like the more realistic diurnal cycle of precipitation or the more accurate representation of heavy precipitation events cannot be achieved with convection parameterizations. Furthermore, in JJA also feedback processes can be sensitive to the accurate representation of deep convection like shown for the soil moisture-precipitation feedback by Hohenegger et al. (2009).

If the model output is used for impact studies which focus, for example, on meso-scale river catchments, ecology in mountain lakes and rivers, or economic losses from extreme events CPCSs can have large benefits by improving especially meso-scale structures which can be essential for these applications. Additionally, the more realistic late season runoff in CPCSs due to their accurate simulation of high snowpack values at high elevations, which typically melt two months earlier in coarser resolved simulations, is important for water supply and flood protection management (Rasmussen et al. 2011).

Further work is in progress to study the representation of atmospheric processes in models with parameterized and explicitly resolved convection, potentially including the use of large eddy simulations. Furthermore, there is great potential in applying convection permitting simulations in climate studies to analyze possible changes in extreme events. This would have the advantage that errors from convective parameterization schemes can be avoided and uncertainties are reduced. One interesting topic which was not addressed in this thesis is the influence of better resolved meso-scale features (like

mountains) in CPCSs on the synoptic-scale flow in the model. One example for such an influence is the generation of lee cyclones which tend to occur at the lee side of mid-latitude mountains like the European Alps, the Rocky Mountains, and the Andes, or shielding effects.

However, CPCSs are still far from being established tools for climate projections, partly due to the lack of comprehensive reference data with resolutions appropriate for the evaluation of CPCSs. Therefore, the detection of errors and the further development of CPCSs will remain challenging.

List of Figures

2.1	CO ₂ concentration and near surface temperature in Antarctica reconstructed from ice core measurements.	21
2.2	Comparisons of observation with atmosphere-ocean general circulation models (AOGCMs) simulations with and without anthropogenic forcings.	22
2.3	Richardson's forecast-factory.	26
2.4	ENIAC 24 hour forecast of height of the 500 hPa surface.	27
2.5	Development of forecast quality from 1955 to 1988.	28
2.6	The GCM family tree.	30
2.7	Development of GCM resolution.	31
2.8	Development of GCM components.	32
2.9	Temporal and spatial scales of atmospheric processes and variations.	34
2.10	Illustration of the concept of dynamical downscaling with an RCM.	36
2.11	Processes in the modeling of clouds with major uncertainties in the mathematical formulations.	44
2.12	Interaction of various processes in the climate system.	44
2.13	Differences between a highly resolved IFS model forecast with and without a non-hydrostatic core.	47
2.14	Mountain lee waves at Amsterdam Island.	48
3.1	A grid-box in the CCLM displaying the staggering of the dependent variables.	57
3.2	Impact of orographic smoothing on the spatial precipitation distribution over the European Alps in the COSMO model.	60
3.3	Hydrological cycle in the standard CCLM cloud and precipitation scheme.	63
3.4	Hydrological cycle in the graupel scheme of CCLM.	64
3.5	Geometrical relationship in the Taylor diagram.	74
3.6	An idealized example to illustrate the algorithm used in the displacement and amplitude score.	88
4.1	Computational domains of the 10 km and 3 km simulations including the evaluation domains.	91

4.2	Spatial box-whisker plots of the seasonal mean bias fields of domain the eastern part of the European Alps (D3) for T2M, PR, RH, and GL. . . .	98
4.3	Diurnal cycles of the spatially averaged simulations in domain D3, and in the sub-regions D4a, and D4b.	101
4.4	Taylor plots of hourly values on grid-point basis.	103
4.5	Simulated minus observed quantile differences and density distributions of INCA for JJA and DJF for T2M, PR, RH, and GL on D3.	105
4.6	Hourly median FSS of the JJA precipitation fields in D3.	108
4.7	Same as in Figure 4.6 but for DJF.	109
4.8	Structure-Amplitude-Location evaluation diagrams for JJA in domain D3.	111
4.9	Same as in Figure 4.8 but for DJF.	112
4.10	Spatial differences of seasonally averaged T2M fields for three selected MM5 simulations depicted as box-whisker plots.	114
4.11	Average JJA PR diurnal cycle in domain D3.	115
4.12	Simulated minus observed quantile deviations for PR in JJA and DJF on D3.	116
4.13	Quantile-quantile plot of cloud liquid water from the 10 km (x-axis) and 3 km simulations on D3 for hourly grid point values between 06:00 am and 06:00 pm in JJA.	119
4.14	The shading shows the orography in the model domain. The Colorado Headwaters are highlighted in the black dashed rectangle. White dots show the location of Snowpack Telemetry (SNOTEL) stations.	122
4.15	Average heavy precipitation (events above the 97.5 th percentile) in the Colorado Headwaters in DJF and JJA.	124
4.16	Variance spectra from the discrete cosine transformation (DCT) of the median heavy precipitation events (events above the 97.5 th percentile) in DJF and JJA.	126
4.17	Spatial distribution of relative differences (simulation minus observation) between simulations and SNOTEL for the average heavy precipitation events (events above the 97.5 th percentile) in DJF and JJA.	127
4.18	Heavy precipitation (events above the 97.5 th percentile) median correlation coefficients, normalized standard deviations, and root-mean-squared-errors for different horizontal grid-spacings of the WRF simulations together with CPC and NARR for DJF and JJA evaluated against SNOTEL data.	130
4.19	Heavy precipitation (events above the 97.5 th percentile) median correlograms, and variograms for DJF and JJA.	131

List of Tables

2.1	Classification of atmospheric scales after Orlanski (1975)	34
3.1	Constant external parameters for the surface (Schättler 2012).	68
3.2	Constant external parameters for the sub-grid-scale orography scheme (SSO) scheme (Schättler 2012).	68
3.3	Constant external parameters for lakes (Schättler 2012).	68
3.4	Other constant external parameters (Schättler 2012).	69
3.5	Plant characteristics (Schättler 2012).	69
3.6	Ozone contents (Schättler 2012).	69
3.7	Aerosol characteristics (Schättler 2012).	70
3.8	Necessary surface variables (Schättler 2012).	70
3.9	Necessary soil variables (for multi-layer soil model) (Schättler 2012).	70
3.10	Necessary atmospheric variables (Schättler 2012).	71
3.11	Optional plant characteristics boundary conditions (Schättler 2012).	71
3.12	Attributes measured by the traditional and new spatial precipitation verification methods (after Brown et al. 2009).	89
4.1	Listing of all simulations with their acronyms and key settings. For CPCs only differences to their corresponding 10 km simulations are mentioned.	95

Acronyms

Symbols

- D three-dimensional wind divergence. 54
- E' pattern root-mean-squared-error. 73, 74
- E^2 root-mean-squared-error. 74
- E_h kinetic energy of horizontal motion. 54
- Fr friction. 23, 24
- H evaporation/condensation heat release/loss. 23, 24
- I_o observed binary fields. 76
- I_x simulated binary fields. 76
- M_u source terms due to turbulent mixing in u . 54
- M_v source terms due to turbulent mixing in v . 54
- M_w source terms due to turbulent mixing in w . 54
- M_{qv} source terms due to turbulent mixing in q^v . 54
- $M_{q^{l,f}}$ source terms due to turbulent mixing in $q^{l,f}$. 54
- N number of pairs. 81
- $O_n(i, j)$ field of observed fractions. 77
- P pressure. 23–25, 27, 56
- $P_{l,f}$ absolute values of the gravitational diffusion fluxes of water and ice. 54, 56, 60
- Q_T diabatic heating term. 54, 56, 60
- Q_v gain or loss of water vapor through phase changes. 23, 24
- R_v gas constant for water vapor. 54
- R_d gas constant for dry air. 54
- S^l cloud microphysical sources/sinks per unit mass of moist air. 54, 56, 60
- T temperature. 23, 25, 54, 56, 64
- T_0 constant reference temperature. 54

- V_a vertical component of absolute vorticity. 54
- $X_n(i, j)$ field of simulated fractions. 77
- Z_{mn} real spectral coefficient. 81
- Δt time step. 94
- Γ variation of reference pressure. 54
- α_b attenuation function. 57
- \bar{E}^2 squared average bias. 74
- $\dot{\zeta}$ nonnormalized contravariant vertical velocity. 54
- γ temperature lapse rate. 23
- γ_d dry adiabatic lapse rate. 23
- λ longitude. 54, 57
- ω rotational frequency of the earth. 23
- ϕ latitude. 23, 54, 57
- ρ density. 23, 25, 54, 56
- ρ_0 constant reference density. 54
- σ standard deviation. 73
- $\sigma^2(m, n)$ spectral variances. 81
- σ_c fractional cloud cover. 65
- cov** _{x_o} covariance. 73
- ζ terrain following vertical coordinate. 54, 56, 57
- a radius of the earth. 23, 54
- c_p specific heat of air at constant pressure. 23
- c_{pd} specific heat capacities of dry air at constant pressure. 54
- c_{vd} specific heat capacities of dry air at constant volume. 54
- d lag tolerance. 81
- f Coriolis parameter. 27
- g acceleration of gravity. 23, 54
- h lag vector. 81, 82
- i longitude index. 56, 57, 73
- j latitude index. 56, 57, 73
- k altitude index. 56, 57

- n time step counter. 58
- p' pressure perturbation from p_0 . 54, 56
- p_0 constant reference pressure. 54
- q specific humidity. 64
- q precipitation threshold. 76
- q^c cloud water. 62, 65
- q^f mass fraction of ice. 54, 56
- q^g graupel. 62
- q^i cloud ice. 62
- q^l mass fraction of water. 54, 56
- q^r rain water. 62
- q^s snow. 62
- q^v mass fraction of water vapor. 54, 56, 62
- q_v specific humidity. 23, 25
- q_{sat} saturation vapor pressure. 64
- q_{spec} specific water content. 62
- r_{xo} correlation coefficient. 73, 74
- s dry static energy. 64
- t time. 23, 58, 73
- u zonal wind velocity. 54, 56
- $u_{\mathbf{g}}$ u component of the geostrophic wind. 27
- v meridional wind velocity. 54, 56
- $v_{\mathbf{g}}$ v component of the geostrophic wind. 27
- w vertical velocity. 54, 56, 64
- z_{ij} two dimensional matrix. 80, 81
- 2nd LF** 2^{nd} order leapfrog scheme. 94
- 3rd RK** 3^{rd} order two time-level Runge-Kutta split-explicit scheme. 94

A

- AMS** American Meteorological Society. 43
- AOGCM** atmosphere-ocean general circulation model. 21, 29, 136
- AR4** fourth assessment report. 29

AR5 fifth assessment report. 29

AWV atmospheric water vapor. 117, 118

B

BTU Brandenburg University of Technology Cottbus. 92

C

CAF cloud area fraction. 118

CC Pearson correlation coefficient. 83, 128, 129

CCLM COSMO model in CLimate Mode. v, vi, 14, 24, 50, 53, 55–59, 61–63, 65–71, 92, 93, 96, 97, 99, 102, 110, 117, 118, 134, 136

CLW cloud liquid water. 117, 118, 137

CMIP3 Coupled Model Intercomparison Project Phase 3. 21

CMIP5 Coupled Model Intercomparison Project Phase 5. 29, 33

CO₂ carbon dioxide. 19, 20, 136

CORINE Coordination of Information on the Environment. 71

COSMO COnsortium for Small scale MOdeling. 24, 49, 60, 92, 136

CPC Climate Prediction Center. 122, 125, 128, 129, 137

CPCS convection permitting climate simulation. i, 14, 15, 17, 46, 48–52, 71, 72, 75, 90, 93, 94, 96, 97, 99, 100, 102–107, 110, 113–118, 120, 121, 132–135, 138

CPS convection permitting simulation. 45, 48, 49, 51, 71, 75

D

D3 the eastern part of the European Alps. 91, 96, 98–100, 104, 105, 107, 110, 114, 116, 118, 136, 137

D4a south-eastern Styria. 91, 96, 99, 100, 103, 104, 120, 137

D4b the Hohe Tauern National Park. 91, 96, 99, 100, 103, 104, 120, 137

D89 Dudhia 1989 short wave radiation scheme. 117, 118

DCT discrete cosine transformation. 80, 125, 137

DJF December, January, and February. 15, 92, 93, 96–100, 102–105, 107, 110, 113–116, 120, 123, 125, 126, 128, 129, 132–134, 137

DSMW Digital Soil Map of the World. 71

DWD Deutscher Wetterdienst. 49, 71

E

ECMWF European Centre for Medium-Range Weather Forecasts. vi, 93, 94

ENIAC Electronic Numerical Integrator And Computer. 25–28, 35, 136

ENSO El Niño–Southern Oscillation. 33

ERA-40 European Centre for Medium-Range Weather Forecasts 40 Year Re-analysis.
42

ESM earth system model. 29

EULAG Eulerian/semi-Lagrangian fluid solver. 46

F

FAR first assessment report. 29

FSS fractions skill score. 14, 15, 49, 76, 77, 100, 106, 107, 116, 133, 137

FWF Austrian Science Fund. vi

G

GCM general circulation model. 28, 29, 31–33, 35–38, 40–43, 45, 136

GL global radiation at surface. 94, 97–99, 102, 105, 117, 118, 132, 134, 136, 137

GLCC Global Land Cover Characteristics. 71

I

IDPS intermittent divergence in phase space. 39, 40

IFS Integrated Forecast System. 46, 93, 96, 99, 100, 102, 103, 106, 107, 110

INCA Integrated Nowcasting through Comprehensive Analysis. 94, 99, 100, 103–105,
107, 110, 113, 115, 116, 137

IPCC Intergovernmental Panel on Climate Change. 29, 31

J

JJA June, July, and August. i, 15, 92, 93, 96–100, 102–107, 110, 113–118, 120, 123, 125,
126, 128, 129, 132–134, 137

K

KF Kain-Fritsch. 94

L

LBC lateral boundary condition. 36–42, 57, 58, 93, 94, 120, 121

M

MAM March, April, and May. 120, 129, 134

MJO Madden–Julian oscillation. 33

MM5 Fifth-Generation NCAR/Penn State Mesoscale Model. 49, 92, 93, 96, 97, 99, 102, 104, 106, 107, 110, 113, 114, 117, 118, 137

MSE mean squared error. 77, 79, 83

N

NARR North American Regional Reanalysis. 121, 122, 125, 128, 129, 137

NCAR National Center for Atmospheric Research. vi, 121

NSD normalized standard deviation. 128

NWP numerical weather prediction. 14, 23, 25, 28, 45, 49, 51, 76, 94

O

OFHS One-point feedback with heavy smoothing. 94

P

PBL planetary boundary layer. 44, 48, 50, 64, 66

PEP PrEProcessor. 71

PR precipitation amount at surface. 94, 96, 98–100, 102, 104–107, 110, 114–116, 132, 136, 137

R

RCA3 Rossby Centre version 3. 51

RCM regional climate model. 13, 15, 17, 24, 35–43, 45, 49–51, 53, 80, 81, 90–94, 96–100, 102, 103, 107, 110, 113, 120, 132, 134, 136

ReLoClim Regional and Local Climate Modeling and Analysis Research Group. v

RG92 Ritter and Geleyn (1992) radiative transfer scheme. 65, 66, 94, 117

RH relative humidity two meters above surface. 94, 97–100, 102, 104, 105, 132, 136, 137

RMSE root-mean-square-error. 75, 83, 125, 126, 128, 129

S

SAL Structure-Amplitude-Location. 15, 83–85, 100, 107, 110, 116, 133, 137

SAR second assessment report. 29

SBC surface boundary condition. 93

SLEVE smooth level vertical. 56

SNOTEL Snowpack Telemetry. 122, 123, 126, 128, 129, 137

SON September, October, and November. 120, 129, 134

SSO sub-grid-scale orography scheme. 66, 68, 138

T

T2M air temperature two meters above surface. i, 94, 96–100, 102, 103, 105, 106, 113, 114, 120, 132, 133, 136, 137

TAR third assessment report. 29

TKE turbulent kinetic energy. 61, 94

TS threat score. 78

TWC two-way coupling. 94

U

UM Unified Model. 49, 51

W

WEGC Wegener Center of the University of Graz. 92

WICE Wegener Center Integrated Climate Model Evaluation. v

WRF Weather Research and Forecasting Model. 15, 48, 50, 52, 92, 93, 96, 97, 99, 102, 104, 107, 110, 117, 118, 121, 125, 128, 132, 137

Z

ZAMG Austrian Central Institute for Meteorology and Geodynamics. 94

Bibliography

- Åberg, S., F. Lindgren, A. Malmberg, J. Holst, and U. Holst (2005). “An image warping approach to spatio-temporal modelling.” In: *Environmetrics* 16.8, 833–848 (cit. on p. 86).
- Alexander, G. D., J. A. Weinman, V. M. Karyampudi, W. S. Olson, and A. C. L. Lee (1999). “The effect of assimilating rain rates derived from satellites and lightning on forecasts of the 1993 superstorm.” In: *Mon. Weather Rev.* 127.7, 1433–1457 (cit. on p. 86).
- Alexandru, A., R. de Elia, R. Laprise, L. Separovic, and S. Biner (2009). “Sensitivity study of regional climate model simulations to large-scale nudging parameters.” In: *Mon. Wea. Rev.* 137, 1666–1686 (cit. on p. 37).
- Ament, F., T. Böhrer, T. Weusthoff, M. Buzzi, Damrath, F. Schubiger, and M. Arpagaus (2008). *Results of fuzzy verification methods with COSMO over Swizerland and Germany*. URL: http://www.aemet.es/documentos/es/divulgacion/conferencias/prediccion/Ewglam/VER_MArpagaus.pdf (cit. on p. 76).
- Antic, S., R. Laprise, B. Denis, and R. de Elía (2004). “Testing the downscaling ability of a one-way nested regional climate model in regions of complex topography.” In: *Clim. Dyn.* 23, 473–493 (cit. on pp. 37, 41).
- Arakawa, A. (1975). “Modelling clouds and cloud processes for use in climate model.” In: *The Physical Basis of Climate and Climate Modelling*. GARP Publication Series 16. GARP Publication Series, WMO, pp. 183–197 (cit. on p. 44).
- (2004). “The Cumulus Parameterization Problem: Past, Present, and Future.” In: *J. Climate* 17, pp. 2493–2525 (cit. on pp. 44, 45).
- Arrhenius, S. (1896). “On the Influence of Carbonic Acid in the Air upon the Temperature of the Ground.” In: *London, Edinburgh, and Dublin Philosophical Magazine and Journal of Science* 41, 237–275 (cit. on pp. 20, 23).
- Aspray, W. (1990). *John Von Neumann and the Origins of Modern Computing*. MIT Press (cit. on p. 26).

- Atger, F. (2001). “Verification of intense precipitation forecasts from single models and ensemble prediction systems.” In: *Nonlinear Proc. in Geoph.* 8.6, pp. 401–417 (cit. on p. 76).
- Baldauf, M. (2008). “Stability analysis for linear discretisations of the advection equation with Runge-Kutta time integration.” In: *J. Comput. Phys.* 227, pp. 6638–6659 (cit. on p. 58).
- Baldauf, M., A. Seifert, J. Förstner, D. Majewski, M. Raschendorfer, and T. Reinhardt (2011). “Operational Convective-Scale Numerical Weather Prediction with the COSMO Model: Description and Sensitivities.” In: *Mon. Wea. Rev.* 139, pp. 3887–3095 (cit. on pp. 48, 49).
- Barry, R. G. (2008). *Mountain Weather and Climate*. 3rd ed. Cambridge University Press (cit. on p. 92).
- Bechtold, P., J. P. Chaboureau, A. Beljaars, A. K. Betts, M. Köhler, M. Miller, and J. L. Redelsperger (2004). “The simulation of the diurnal cycle of convective precipitation over land in a global model.” In: *Quart. J. Roy. Meteor. Soc.* 130, pp. 3119–3137 (cit. on p. 45).
- Betts, A. K. and M. J. Miller (1986). “A new convective adjustment scheme. Part II: Single column tests using GATE wave, BOMEX, ATEX and arctic air-mass data sets.” In: *Quart. J. Roy. Meteor. Soc.* 112, pp. 693–709 (cit. on p. 122).
- Betts, A. K., J. H. Ball, A. C. M. Beljaars, M. J. Miller, and P. A. Viterbo (1996). “The land surface–atmosphere interaction: A review based on observational and global modeling perspectives.” In: *J. Geophys. Res.* 101, pp. 7209–7225 (cit. on p. 50).
- Bielli, S. and R. Laprise (2006). “A methodology for regional-scale-decomposed atmospheric water budget: application to a simulation of the Canadian RCM nested by NCEP-NCAR reanalyses over North America.” In: *Mon. Weather Rev.* 134, pp. 854–873 (cit. on p. 43).
- Bjerknes, V. (1904). “Das Problem der Wettervorhersage, betrachtet vom Standpunkte der Mechanik und der Physik.” In: *Met. Zeit.* 21, 1–7 (cit. on p. 23).
- Böhm, U., M. Kücken, W. Ahrens, A. Block, D. Hauffe, K. Keuler, B. Rockel, and A. Will (2006). *CLM—The climate version of LM: Brief description and long-term applications*. Tech. rep. COSMO Newsletter, pp. 225–235 (cit. on p. 92).
- Bradley, R. (1999). *Paleoclimatology*. Academic Press, Harcourt Brace and Company (cit. on p. 18).
- Brockhaus, P., D. Lüthi, and C. Schär (2008). “Aspects of the diurnal cycle in a regional climate model.” In: *Meteorol. Z.* 17, 433–443 (cit. on pp. 15, 45).

- Broecker, W., D. L. Thurber, J. Goddard, T. L. Ku, R. K. Matthews, and K. J. Mesolella (1968). "Milankovitch Hypothesis Supported by Precise Dating of Coral Reef and Deep-Sea Sediments." In: *Science* 159, 297–300 (cit. on p. 18).
- Brooks, H. E., M. Kay, and J. A. Hart (1998). *Objective limits on forecasting skill of rare events* (cit. on p. 76).
- Brown, B., R. Bullock, J. H. Gotway, D. Ahijevych, E. Gilleland, B. Ebert, and B. Casati (2009). *Spatial Verification Methods* (cit. on p. 89).
- Businger, J. A., J. C. Wyngaard, Y. Izumi, and E. F. Bradley (1971). "Flux profile relationships in the atmospheric surface layer." In: *J. Atmos. Sci.* 28, pp. 181–189 (cit. on p. 61).
- COMET (May 2013). The COMET Program. URL: http://www.meted.ucar.edu/tropical/textbook_2nd_edition/navmenu.php?tab=2&page=8.1.0 (cit. on p. 34).
- Callendar, G. S. (1938). "The artificial production of carbon dioxide and its influence on temperature." In: *Quart. J. Roy. Meteor. Soc.* 64 (275), 223–240 (cit. on p. 20).
- Casati, B., G. Ross, and D. B. Stephenson (2004). "A new intensity-scale approach for the verification of spatial precipitation forecasts." In: *Meteorol. Appl.* 11.2, 141–154 (cit. on pp. 76, 78, 83).
- Castro, C. L., S. R. A. Pielke, and G. Leoncini (2005). "Dynamical downscaling: assessment of value retained and added using the Regional Atmospheric Modeling System (RAMS)." In: *J. Geophys. Res.* 110 (cit. on p. 42).
- Cebon, P., U. Dahinden, H. Davies, D. Imboden, and C. C. Jaeger, eds. (1998). *Views from the Alps: Regional Perspectives on Climate Change (Politics, Science, and the Environment)*. The MIT Press, p. 531 (cit. on p. 15).
- Charney, J. G., R. Fjørtoft, and J. von Neumann (1950). "Numerical Integration of the Barotropic Vorticity Equation." In: *Tellus* 2 (4), 237–245 (cit. on pp. 26, 27).
- Christensen, J. H. and O. B. Christensen (2001). "Regional climate scenarios—A study on precipitation." In: *Climate Change Research, Danish Contributions*. ISBN 8712-03775-3. Gads Forlag Danish Meteorological Institute, pp. 151–166 (cit. on p. 42).
- (2007). "A summary of the PRUDENCE model projection of changes in European climate by the end of this century." In: *Mon. Weather Rev.* 81, pp. 7–30 (cit. on pp. 13, 43).
- Croll, J. (1875). *Climate and time in their geological relations. A theory of secular changes of the Earth's climate*. New York: Appleton (cit. on p. 18).
- DKRZ and BTU Cottbus (May 2013). URL: www.clm-community.eu (cit. on p. 36).
- Dai, A. G., F. Giorgi, and K. E. Trenberth (1999). "Observed and model-simulated diurnal cycles of precipitation over the contiguous United States." In: *J. Geophys. Res.* 104, 6377–6402 (cit. on pp. 15, 45).

- Dai, A. and K. E. Trenberth (2004). “The diurnal cycle and its depiction in the community climate system model.” In: *J. Climate* 5, pp. 930–951 (cit. on p. 45).
- Damrath, U. (2004). *Verification against precipitation observations of a high density network, what did we learn?* (Cit. on p. 76).
- Dansgaard, W., H. B. Clausen, N. Gundestrup, C. U. Hammer, S. F. Johnsen, P. M. Kristinsdottir, and N. Reeh (1982). “A new greenland deep ice core.” In: *Science* 218 (4579), 1273–1277 (cit. on p. 20).
- Davies, H. C. (1976). “A lateral boundary formulation for multi-level prediction models.” In: *Quart. J. R. Met. Soc.* 102, pp. 405–418 (cit. on p. 58).
- (1983). “Limitations of some common lateral boundary schemes used in regional NWP models.” In: *Mon. Wea. Rev.* 111, pp. 1002–1012 (cit. on p. 58).
- Davies, L. A. and A. R. Brown (2001). “Assessment of which scales of orography can be credibly resolved in a numerical model.” In: *Quart. J. Roy. Meteor. Soc.* 127, pp. 1225–1237 (cit. on p. 59).
- Davis, C., B. Brown, and R. Bullock (2006). “Object-based verification of precipitation forecasts. Part I: Methodology and application to mesoscale rain areas.” In: *Mon. Weather Rev.* 134.7, 1772–1784 (cit. on p. 83).
- Denis, B., R. Laprise, D. Caya, and J. Co^o (2002[a]). “Downscaling ability of one-way nested regional climate models: The Big-Brother experiment.” In: *Clim. Dyn.* 18, 627–646 (cit. on pp. 41, 80, 81, 125).
- Denis, B., J. Cote, and R. Laprise (2002[b]). “Spectral decomposition of two-dimensional atmospheric fields on limited-area domains using the discrete cosine transform (DCT).” In: *Mon. Weather Rev.* 130.7, 1812–1829 (cit. on pp. 37, 41).
- Denis, B., R. Laprise, and D. Caya (2003). “Sensitivity of a regional climate model to the spatial resolution and temporal updating frequency of the lateral boundary conditions.” In: *Clim. Dyn.* 20, 107–126 (cit. on pp. 37, 41).
- Déqué, M., D. Rowell, D. Lüthi, F. Giorgi, J. Christensen, B. Rockel, D. Jacob, E. Kjellström, M. de Castro, and B. van den Hurk (2007). “An intercomparison of regional climate simulations for Europe: assessing uncertainties in model projections.” In: *Clim. Change* 81, pp. 53–70 (cit. on pp. 14, 39, 43).
- Diaconescu, E. P., R. Laprise, and L. Sushama (2007). “The impact of lateral boundary data errors on the simulated climate of a nested regional climate model.” In: *J. Climate* 4, pp. 333–350 (cit. on p. 42).
- Dickenson, R. E., R. M. Errico, F. Giorgi, and G. T. Bates (1989). “A regional climate model for western United States.” In: *Climatic Change* 15, pp. 383–422 (cit. on p. 13).

- Dickinson, R. E., R. M. Errico, F. Giorgi, and G. T. Bates (1989). “A regional climate model for western United States.” In: *Clim. Change* 15.3, 383–422 (cit. on p. 35).
- Dickinson, S. and R. A. Brown (1996). “A study of near-surface winds in marine cyclones using multiple satellite sensors.” In: *J. Appl. Meteorol.* 35.6, 769–781 (cit. on p. 86).
- Dimitrijevic, M. and R. Laprise (2005). “Validation of the nesting technique in a RCM and sensitivity tests to the resolution of the lateral boundary conditions during summer.” In: *Clim. Dyn.* 25, 555–580 (cit. on pp. 37, 41).
- Doms, G. (2011). *A Description of the Nonhydrostatic Regional COSMO-Model; Part I: Dynamics and Numerics*. Tech. rep. Deutscher Wetterdienst. URL: <http://www.cosmo-model.org/content/model/documentation/core/#p1> (cit. on pp. 54, 56–60, 66).
- Doms, G. and J. Förstner (2004). *Development of a kilometer-scale NWP-system: LMK*. Tech. rep. COSMO Newsletter, pp. 159–167 (cit. on p. 92).
- Doms, G., J. Förstner, E. Heise, H.-J. Herzog, D. Mironov, M. Raschendorfer, T. Reinhardt, B. Ritter, R. Schrodin, J.-P. Schulz, and G. Vogel (2011). *A Description of the Nonhydrostatic Regional COSMO-Model; Part II: Physical Parameterization*. Tech. rep. Deutscher Wetterdienst. URL: <http://www.cosmo-model.org/content/model/documentation/core/#p2> (cit. on pp. 61–63, 65–67, 71).
- Dudhia, J. (1989). “Numerical study of convection observed during the Winter Monsoon Experiment using a mesoscale two-dimensional model.” In: *J. Atmos. Sci.* 46, pp. 3077–3107 (cit. on pp. 95, 117).
- (1993). “A nonhydrostatic version of the Penn State/NCAR Mesoscale Model: Validation tests and simulation of an Atlantic cyclone and cold front.” In: *Mon. Wea. Rev.* 121, pp. 1493–1513 (cit. on p. 92).
- Dutton, J. A. (1976). *The Ceaseless Wind*. McGraw-Hill, New York, USA (cit. on pp. 24, 46).
- Ebert, E. E. (2008). “Fuzzy verification of high-resolution gridded forecasts: a review and proposed framework.” In: *Meteorol. Appl.* 15.1, 51–64 (cit. on p. 76).
- Ebert, E. E. and J. L. McBride (2000). “Verification of precipitation in weather systems: determination of systematic errors.” In: *J. Hydrol.* 239.1–4, 179–202 (cit. on p. 83).
- Edwards, P. N. (2010). *A vast machine: computer models, climate data, and the politics of global warming*. The MIT Press (cit. on pp. 17, 25, 28, 30, 32).
- Elía, R. de, R. Laprise, and B. Denis (2002). “Forecasting skill limits of nested limited-area models: a perfect-model approach.” In: *Mon. Weather* 130, 2206–2023 (cit. on p. 39).

- Eltahir, E. A. B. (1998). “A soil moisture–rainfall feedback mechanism 1. Theory and observations.” In: *Water Resour. Res.* 34, pp. 765–776 (cit. on p. 50).
- Emiliani, C. (1955). “Pleistocene Temperatures.” In: *J. Geology* 63, 538–578 (cit. on p. 18).
- Evans, E. P. (1887). “The Authorship of the Glacial Theory.” In: *North American review* 145 (368), 94–104 (cit. on p. 18).
- Feser, F. (2006). “Enhanced detectability of added value in limited-area model results separated into different spatial scales.” In: *Mon. Wea. Rev.* 134, pp. 2180–2190 (cit. on pp. 42, 43).
- Feser, F. and H. Von Storch (2005). “A spatial two-dimensional discrete filter for limited area model evaluation purposes.” In: *Mon. Wea. Rev.* 133, pp. 1774–1786 (cit. on p. 43).
- Findell, K. L. and E. A. B. Eltahir (2003). “Atmospheric controls on soil moisture–boundary layer interactions. Part I: Framework development.” In: *J. Hydrometeorol.* 4, pp. 552–569 (cit. on p. 50).
- Finger, D., G. Heinrich, A. Gobiet, and A. Bauder (2012). “Projections of future water resources and their uncertainty in a glacialized catchment in the Swiss Alps and the subsequent effects on hydropower production during the 21st century.” In: *Water Resour. Res.* (Cit. on p. 13).
- Fleming, J. R. (2007). *The Callendar Effect. The Life and Work of Guy Stewart Callendar (1898-1964)*. American Meteorological Society (cit. on p. 20).
- Fourier, J. J. (1827). “Mémoire sur les Températures du Globe Terrestre et des Espaces Planétaires.” In: *Mémoires d’Académie Royale des Sciences de l’Institut de France* 7, 570–604 (cit. on p. 19).
- Gassmann, A. (2002). *3D-transport of precipitation*. Tech. rep. COSMO Newsletter, pp. 113–117 (cit. on p. 59).
- Gebhardt, C., S. E. Theisa, M. Paulata, and Z. B. Bouallèguea (2011). “Uncertainties in COSMO-DE precipitation forecasts introduced by model perturbations and variation of lateral boundaries.” In: *Atmos Res.* 100 (2–3), pp. 168–177 (cit. on pp. 14, 49).
- Gebremichael, M. and W. F. Krajewski (Aug. 2004). “Assessment of the statistical characterization of small-scale rainfall variability from radar: Analysis of TRMM ground validation datasets.” In: *J. Appl. Meteorol.* 43.8, 1180–1199 (cit. on p. 81).
- Geleyn, J. F. and A. Hollingsworth (1979). “An Economical Analytic Method for the Computing of the Interaction Between Scattering and Line Absorption of Radiation.” In: *Beitr. Phys. Atm.* 52, pp. 1–16 (cit. on pp. 66, 117).

- Georgievski, G., K. Keuler, A. Will, and K. Radtke (2011). *Evaluation of Central European and Eastern Alpine seasonal climate simulated with CCLM: double nesting vs. direct forcing techniques*. Tech. rep. COSMO Newsletter, pp. 133–143 (cit. on p. 92).
- Germann, U. and J. Joss (2001). “Variograms of radar reflectivity to describe the spatial continuity of Alpine precipitation.” In: *J. Appl. Meteorol.* 40.6, 1042–1059 (cit. on p. 81).
- Germann, U. and I. Zawadzki (2004). “Scale dependence of the predictability of precipitation from continental radar images. Part II: Probability forecasts.” In: *J. Appl. Meteorol.* 43.1, 74–89 (cit. on p. 76).
- Gilleland, E., J. Lindstrom, and F. Lindgren (2010). “Analyzing the Image Warp Forecast Verification Method on Precipitation Fields from the ICP.” In: *Weather Forecast.* 25.4, 1249–1262 (cit. on p. 86).
- Giorgi, F. and G. T. Bates (1989). “The climatological skill of a regional model over complex terrain.” In: *Mon. Weather Rev.* 117.11, 2325–2347 (cit. on pp. 13, 35).
- Gobiet, A. and D. Jacob (2012). *EURO-CORDEX Community (2012) A new generation of regional climate simulations for Europe: The EURO-CORDEX Initiative*. Geophysical Research Abstracts Vol. 14, EGU2012-8211, 2012, EGU General Assembly 2012 (cit. on pp. 13, 43).
- Grell, G. A., J. Dudhia, and D. R. Stauffer (1995). *A Description of the Fifth-Generation Penn State/NCAR Mesoscale Model (MM5)*. Tech. rep. NCAR/TN-398+STR. URL: <http://www.mmm.ucar.edu/mm5/mm5-home.html> (cit. on p. 95).
- Grell, G. A., L. Schade, R. Knoche, A. Pfeiffer, and J. Egger (2000). “Nonhydrostatic climate simulations of precipitation over complex terrain.” In: *J. Geophys. Res.* 105, pp. 595–608 (cit. on pp. 14, 50).
- Grotch, S. L. and M. C. MacCracken (1991). “The use of general circulation models to predict regional climatic change.” In: *J. Climate* 4, 286–303 (cit. on p. 33).
- Haiden, T., A. Kann, G. Pistotnik, K. Stadlbacher, and C. Wittmann (2010). *Integrated Nowcasting through Comprehensive Analysis (INCA) System description*. Tech. rep. Central Institute for Meteorology and Geodynamics, Vienna, Austria. URL: http://www.zamg.ac.at/fix/INCA_system.doc (cit. on p. 94).
- Hann, J. von (1903). *Handbook of Climatology*. Macmillan (cit. on p. 19).
- Harper, K. (2008). *Weather by the Numbers: The Genesis of Modern Meteorology*. MIT Press (cit. on p. 25).
- Harris, D., E. Foufoula-Georgiou, K. K. Droegemeier, and J. J. Levit (2001). “Multiscale statistical properties of a high-resolution precipitation forecast.” In: *J. Hydrometeorol.* 2.4, 406–418 (cit. on p. 81).

- Heinrich, G. and A. Gobiet (2011). “The future of dry and wet spells in Europe: A comprehensive study based on the ENSEMBLES regional climate models.” In: *Int. J. Climatol.* 32 (13) (cit. on p. 13).
- Herzog, H.-J., G. Vogel, and U. Schubert (2002a). “LLM - a nonhydrostatic model applied to high-resolving simulations of turbulent fluxes over heterogeneous terrain.” In: *Theor. Appl. Climatol.* 73, pp. 67–86 (cit. on p. 61).
- Herzog, H.-J., U. Schubert, G. Vogel, A. Fiedler, and R. Kirchner (2002b). *LLM - the high-resolving nonhydrostatic simulation model in the DWD-project LITFASS. Part I: Modelling technique and simulation method.* COSMO Technical Report 4. Deutscher Wetterdienst (cit. on p. 61).
- Hewitson, B. C. and R. G. Crane (1996). “Climate downscaling: techniques and application.” In: *Climate Research* 7, 85–95 (cit. on p. 35).
- Higgins, R. W., W. Shi, E. Yarosh, and J. R. (2000). *Improved United States Precipitation Quality Control System and Analysis.* Tech. rep. NCEP/Climate Prediction Center Atlas 7. URL: <http://www.esrl.noaa.gov/psd/data/gridded/data.unified.html> (cit. on p. 123).
- Hohenegger, C., P. Brockhaus, and C. Schär (2008). “Towards climate simulations at cloud-resolving scales.” In: *Meteorol. Z.* 17 (4), 383–394 (cit. on pp. 14, 50, 51, 133).
- Hohenegger, C., P. Brockhaus, C. S. Bretherton, and C. Schär (2009). “The Soil Moisture–Precipitation Feedback in Simulations with Explicit and Parameterized Convection.” In: *J. Climate* 22, 5003–5020 (cit. on pp. 50, 134).
- Holton, J. R. (2004). *An Introduction to Dynamic Meteorology.* Elsevier (cit. on pp. 24, 46).
- Ikeda, K., R. M. Rasmussen, C. Liu, D. Gochis, D. Yates, F. Chen, M. Tewari, M. Barlage, J. Dudhia, K. Miller, K. Arsenault, V. Grubišič, G. Thompson, and E. Guttman (2010). “Simulation of seasonal snowfall over Colorado.” In: *Atmos. Res.* 97 (4), 462–477 (cit. on pp. 51, 122, 125).
- Inatsu, M. and M. Kimoto (2009). “A scale interaction study on East Asian cyclogenesis using a General Circulation Model coupled with an interactively nested regional model.” In: *Mon. Wea. Rev.* 9, p. 137 (cit. on p. 40).
- Isaaks, E. H. and S. M. Srivastava (1989). *An Introduction to Applied Geostatistics.* Vol. 1. Oxford University Press, p. 592 (cit. on p. 81).
- Jacobsen, I. and E. Heise (1982). “A new economic method for the computation of the surface temperature in numerical models.” In: *Contr. Atmos. Phys.* 55, pp. 128–141 (cit. on p. 67).

- Janjić, Z. I. (1994). “The step-mountain Eta coordinate model: Further developments of the convection, viscous sublayer, and turbulence closure schemes.” In: *Mon. Wea. Rev.* 122, pp. 927–945 (cit. on p. 122).
- Jones, R. G., J. M. Murphy, and M. Noguer (1995). “Simulation of climate change over Europe using a nested regional climate model. I: assessment of control climate, including sensitivity to location of lateral boundaries.” In: *Quart. J. R. Met. Soc.* 121, 1413–1449 (cit. on p. 37).
- Kain, J. S. (2003). “The Kain-Fritsch convection parameterization: an update.” In: *J. Appl. Meteor.* 43, pp. 170–181 (cit. on p. 95).
- Kain, J. S. and J. Fritsch (1993). “Convective parameterization for mesoscale models: The Kain Fritsch scheme. In The Representation of Cumulus Convection in Numerical Models.” In: *Meteor. Monogr.* 24, pp. 165–170 (cit. on pp. 64, 95).
- Kain, J. S., S. J. Weiss, J. J. Levit, M. E. Baldwin, and D. R. Bright (2006). “Examination of Convection-Allowing Configurations of the WRF Model for the Prediction of Severe Convective Weather: The SPC/NSSL Spring Program 2004.” In: *Wea. Forecasting*. 21 (2), pp. 167–181 (cit. on pp. 14, 49).
- Kallberg, P. (1977). *A lateral boundary formulation for multi-level prediction models*. Tech. rep. 3. ECMWF Research Department. URL: <http://www.cosmo-model.org/content/model/documentation/core/#p1> (cit. on p. 58).
- Kann, A., T. Haiden, K. von der Emde, C. Gruber, T. Kabas, A. Leuprecht, and G. Kirchengast (2011). “Verification of Operational Analyses Using an Extremely High-Density Surface Station Network.” In: *Wea. Forecasting* 26 (4), pp. 572–578 (cit. on p. 94).
- Kapper, K. L. (2009). *Scale Sensitive Analysis of Regional Climate Models*. Wegener Center Verlag Graz, p. 114 (cit. on p. 81).
- Keil, C. and G. C. Craig (2007). “A displacement-based error measure applied in a regional ensemble forecasting system.” In: *Mon. Weather Rev.* 135.9, 3248–3259 (cit. on pp. 86, 87).
- (2009). “A Displacement and Amplitude Score Employing an Optical Flow Technique.” In: *Weather Forecast.* 24.5, 1297–1308 (cit. on pp. 86, 88).
- Kendon, E. J., N. M. Roberts, C. A. Senior, and M. J. Roberts (2012). “Realism of Rainfall in a Very High-Resolution Regional Climate Model.” In: *J. Climate* 25, pp. 5791–5806 (cit. on pp. 51, 133).
- Kerr, R. A. (2011). “Predicting Climate Change Vital Details of Global Warming Are Eluding Forecasters.” In: *Science* 334 (6053), 173–174 (cit. on p. 40).
- Kessler, E. (1969). *On the Distribution and Continuity of Water Substance in Atmospheric Circulation*. Vol. 32. Meteor. Monogr., AMS, USA, p. 84 (cit. on p. 62).

- Kida, H., T. Koide, H. Sasaki, and M. Chiba (1991). “A new approach for coupling a limited area model to a GCM for regional climate simulations.” In: *J. Meteorol. Soc. Japan* 69, 723–728 (cit. on p. 37).
- Kiehl, J. T. (2007). “Twentieth Century Climate Model Response and Climate Sensitivity.” In: *Geophys. Res. Lett.* 34, L22710 (cit. on p. 33).
- Klemp, J. and R. Wilhelmson (1978). “The simulation of three-dimensional convective storm dynamics.” In: *J. Atmos. Sci.* 35, pp. 1070–1096 (cit. on pp. 58, 95).
- Lacis, A. A. and J. E. Hansen (1974). “A parameterization for the absorption of solar radiation in the earth’s atmosphere.” In: *J. Atmos. Sci.* 31, pp. 118–133 (cit. on p. 117).
- Langhans, W., J. Schmidli, and C. Schär (2012). “Bulk convergence of cloud-resolving simulations of moist convection over complex terrain.” In: *J. Atmos. Sci.* 69, pp. 2207–2228 (cit. on pp. 14, 45, 122).
- Laprise, R. (2003). “Resolved scales and nonlinear interactions in limited-area models.” In: *J. Atmos. Sci.* 60 (5), pp. 768–779 (cit. on p. 43).
- (2008). “Regional climate modelling.” In: *J. Comput. Phys.* 227 (7), pp. 3641–3666 (cit. on pp. 38–41, 43).
- Leduc, M. and R. Laprise (2009). “Regional climate model sensitivity to domain size.” In: *Clim. Dyn.* 32, 833–854 (cit. on p. 37).
- Lee, M.-I., S. D. Schubert, M. J. Suarez, I. M. Held, A. Kumar, T. L. Bell, J. K. E. Schemm, N. C. LAU, J. J. PLothay, H. K. Kim, and S. H. Yoo (2007). “Sensitivity to horizontal resolution in the AGCM simulations of warm season diurnal cycle of precipitation over the United States and northern Mexico.” In: *J. Climate* 20, pp. 1862–1881 (cit. on p. 45).
- Linden, P. van der and J. F. B. Mitchell (2009). *ENSEMBLES: Climate Change and its Impacts: Summary of research and results from the ENSEMBLES project*. Tech. rep. Met Office Hadley Centre, p. 160 (cit. on pp. 13, 43).
- Liu, C. H., K. Ikeda, G. Thompson, R. M. Rasmussen, and J. Dudhia (2011). “High-Resolution Simulations of Wintertime Precipitation in the Colorado Headwaters Region: Sensitivity to Physics Parameterizations.” In: *Mon. Wea. Rev.* 139 (11), pp. 3533–3553 (cit. on pp. 48, 122).
- Loibl, W., H. Formayer, W. Schöner, H. Truhetz, I. Anders, A. Gobiet, G. Heinrich, M. Köstl, I. Nadeem, J. Peters-Anders, I. Schicker, M. Suklitsch, and H üger (2011). *reclip:century 1, Research for Climate Protection: Century Climate Simulations: Models, Data and GHG-Scenarios, Simulations*. Tech. rep. ACRP final report reclip:century part A, Vienna, AUT (cit. on pp. 13, 43).

- Lorenz, P. and D. Jacob (2005). “Influence of regional scale information on the global circulation: A two-way nesting climate simulation.” In: *Geophys. Res. Lett.* 32, p. L18706 (cit. on p. 40).
- Lott, F. and M. Miller (1997). “A new subgrid-scale orographic drag parametrization: Its formulation and testing.” In: *Q. J. R. Meteor. Soc.* 123, pp. 101–127 (cit. on p. 66).
- Louse, J.-F. (1979). “A parametric model of vertical eddy fluxes in the atmosphere.” In: *Bound. Layer Meteor.* 17, pp. 187–202 (cit. on p. 61).
- Mallat, S. (1999). *A Wavelet Tour of Signal Processing, Second Edition (Wavelet Analysis & Its Applications)*. 2nd ed. Academic Press. ISBN: 012466606X (cit. on p. 79).
- Manabe, S. and R. T. Wetherald (1967). “Thermal Equilibrium of the Atmosphere with a Given Distribution of Relative Humidity.” In: *J. Atmos. Sci.* 24 (3), 241–259 (cit. on p. 20).
- Marbaix, P., H. Gallé, O. Brasseur, and J.-P. van Ypersele (2003). “Lateral boundary conditions in regional climate models: a detailed study of the relaxation procedure.” In: *Mon. Wea. Rev.* 131, 461–479 (cit. on p. 38).
- Marzban, C. and S. Sandgathe (2006). “Cluster analysis for verification of precipitation fields.” In: *Weather Forecast.* 21.5, 824–838 (cit. on p. 83).
- (2009). “Verification with Variograms.” In: *Weather Forecast.* 24.4, 1102–1120 (cit. on p. 81).
- Mass, C. F., D. Ovens, K. Westrick, and B. A. Colle (2002). “Does Increasing Horizontal Resolution Produce More Skillful Forecasts?” In: *Bull. Amer. Meteor. Soc.* 83.3, 407–430 (cit. on pp. 14, 49, 75).
- Mearns, L. O., W. J. Gutowski, R. Jones, L.-Y. Leung, S. McGinnis, A. M. B. Nunes, and Y. Qian (2009). “A regional climate change assessment program for North America.” In: *EOS*. 90, pp. 311–312 (cit. on pp. 13, 43).
- Mellor, G. and T. Yamada (1974). “A hierarchy of turbulence closure models for planetary boundary layers.” In: *J. Atm. Sc.* 31, pp. 1791–1806 (cit. on p. 61).
- (1982). “Development of a turbulence closure model for geophysical fluid problems.” In: *Rev. Geophys. and Space Phys.* 20, pp. 851–875 (cit. on p. 61).
- Mesinger, F., G. Dimego, E. K. Alnay, K. Mitchell, P. C. Shafran, W. Ebisuzaki, D. A. Jović, J. Woollen, E. Rogers, E. H. Berbery, M. B. Ek, Y. Fan, R. Grumbine, W. Higgins, H. Li, Y. Lin, G. Manikin, D. Parrish, and W. Shi (2006). “North American Regional Reanalysis.” In: *Bull. Amer. Meteor. Soc.* 87, pp. 343–360 (cit. on p. 122).

- Micheas, A. C., N. I. Fox, S. A. Lack, and C. K. Wikle (2007). “Cell identification and verification of QPF ensembles using shape analysis techniques.” In: *J. Hydrol.* 343.3–4, 105–116 (cit. on p. 84).
- Molinari, J. and M. Dudek (1992). “Parameterization of convective precipitation in mesoscale numerical models - a critical review.” In: *Mon. Wea. Rev.* 120, 326–344 (cit. on pp. 15, 45).
- Moore, G. E. (1965). “Cramming more components onto integrated circuits.” In: *Electronics Magazine* 38 (8), 114–117 (cit. on p. 29).
- Morrison, H., G. Thompson, and V. Tatarskii (2009). “Impact of cloud microphysics on the development of trailing stratiform precipitation in a simulated squall line: Comparison of one- and two-moment schemes.” In: *Mon. Wea. Rev.* 137, pp. 991–1007 (cit. on p. 48).
- Muller, R. A. and J. MacDonald (2000). *Ice Ages and Astronomical Causes: Data, spectral analysis and mechanisms*. Springer Praxis Books (cit. on p. 18).
- NASA (May 2013). URL: http://upload.wikimedia.org/wikipedia/commons/thumb/b/b1/Wave_cloud.jpg/180px-Wave_cloud.jpg (cit. on p. 48).
- Neumann, J. (1985). “Climatic Change as a Topic in the Classical Greek and Roman Literature.” In: *Climatic Change* 7, 441–454 (cit. on p. 19).
- Nievergelt, Y. (1999). *Wavelets Made Easy*. 2nd ed. Birkhauser. ISBN: 0817640614 (cit. on p. 79).
- Oreskes, N., D. A. Stainforth, and L. A. Smith (2010). “Adaptation to Global Warming: Do Climate Models Tell Us What We Need to Know?” In: *Philosophy of Science* 77, (cit. on p. 40).
- Orlanski, I. (1975). “A rational subdivision of scales for atmospheric processes.” In: *Bull. Amer. Meteor. Soc.* 50 (5), pp. 527–530 (cit. on p. 34).
- Pal, J. S. and E. A. B. Eltahir (2001). “Pathways relating soil moisture conditions to future summer rainfall within a model of the land–atmosphere system.” In: *J. Climate* 14, pp. 1227–1242 (cit. on p. 50).
- Peixoto, J. P. and A. H. Oort (1992). *Physics of climate*. American Institute of Physics, p. 520 (cit. on p. 80).
- Petch, J. C., A. R. Brown, and M. E. B. Gray (2002). “The impact of horizontal resolution on the simulations of convective development over land.” In: *Quart. J. Roy. Meteor. Soc.* 128, pp. 2031–2044 (cit. on p. 45).
- Petersen, W. A., L. D. Carey, S. A. Rutledge, J. C. Knievel, R. H. Johnson, N. J. Doesken, T. B. McKee, T. V. Haar, and J. F. Weaver (1999). “Mesoscale and Radar Observations of the Fort Collins Flash Flood of 28 July 1997.” In: *Bull. Amer. Meteor. Soc.* 80, pp. 191–216 (cit. on p. 15).

- Phillips, N. A. (1956). “The General Circulation of the Atmosphere: A Numerical Experiment.” In: *Quart. J. Roy. Meteor. Soc.* 82, 123–164 (cit. on p. 28).
- Pielke, R. A. S. and R. L. Wilby (2012). “Regional climate downscaling: What’s the point?” In: *Eos, Transactions American Geophysical Union* 93 (5), 52–53 (cit. on p. 40).
- Platzman, G. W. (1979). “The ENIAC Computations of 1950 – Gateway to Numerical Weather Prediction.” In: *Bull. Amer. Met. Soc.* 60, 302–312 (cit. on p. 27).
- Prein, A. F. and A. Gobiet (2011). *Defining and Detecting Added Value in Cloud Resolving Climate Simulations*. Tech. rep. Wegener Center Report, 39, Wegener Center Verlag, Graz, Austria (cit. on p. 72).
- Prein, A. F., A. Gobiet, M. Suklitsch, H. Truhetz, N. K. Awan, K. Keuler, and G. Georgievski (2013[a]). “Added Value of Convection Permitting Seasonal Simulations.” In: *Clim. Dyn.* DOI:10.1007/s00382-013-1744-6 (cit. on pp. 15, 45).
- Prein, A. F., G. J. Holland, R. M. Rasmussen, J. Done, K. Ikeda, M. P. Clark, and C. H. Liu (2013[b]). “Importance of Regional Climate Model Grid Spacing for the Simulation of Precipitation Extremes.” In: *J. Climate* DOI:10.1175/JCLI-D-12-00727.1 (cit. on pp. 33, 81, 82).
- Prusa, J. M., P. K. Smolarkiewicz, and A. A. Wyszogrodzki (2008). “EULAG, a computational model for multiscale flows.” In: *Comput. Fluids* 37, pp. 1193–1207 (cit. on p. 46).
- Pryor, S. C., G. Nikulin, and C. Jones (2012). “Influence of spatial resolution on regional climate model derived wind climates.” In: *J. Geophys. Res.* 117 (D3), pp. 2156–2202 (cit. on p. 51).
- Radu, R., M. Déqué, and S. Somot (2008). “Spectral nudging in a spectral regional climate model.” In: *Tellus A* 60, 898–910 (cit. on p. 37).
- Randall, D. A., R. A. Wood, S. Bony, R. Colman, T. Fichefet, J. Fyfe, V. Kattsov, A. Pitman, J. Shukla, J. Srinivasan, R. J. Stouffer, A. Sumi, and K. E. Taylor (2007). *Climate Models and Their Evaluation. In: Climate Change 2007: The Physical Science Basis. Contribution of Working Group I to the Fourth Assessment Report of the Intergovernmental Panel on Climate Change*. Ed. by S. Solomon, D. Qin, M. Manning, Z. Chen, M. Marquis, K. Averyt, M. Tignor, and H. L. Miller. Cambridge University Press, Cambridge, United Kingdom and New York, NY, USA (cit. on pp. 14, 20, 22, 33, 43).
- Rasmussen, R. M., K. Ikeda, C. Liu, D. J. Gochis, J. Dudhia, G. Thompson, F. Chen, M. Tewari, E. D. Gutmann, V. Grubisic, and K. R. Arsenault (2011). “Acceleration of the Water Cycle over the Colorado Headwaters Region from Eight Year Cloud Resolving Simulations of the WRF Climate Model.” In: Abstract A31K-07 presented at 2011 Fall Meeting, AGU, San Francisco, Calif., 5-9 Dec. (cit. on p. 122).

- Rasmussen, R. M., C. Liu, K. Ikeda, D. Gochis, D. Yates, F. Chen, M. Tewari, M. Barlage, J. Dudhia, W. Yu, K. Miller, K. Arsenault, V. Grubišić, G. Thompson, and E. Gutmann (2011). “High-Resolution Coupled Climate Runoff Simulations of Seasonal Snowfall over Colorado: A Process Study of Current and Warmer Climate.” In: *J. Climate* 24, 3015–3048 (cit. on pp. 50, 51, 122, 125, 134).
- Rasmussen, R. M., B. Baker, J. Kochendorfer, T. Meyers, S. Landolt, A. P. Fischer, J. Black, J. M. Thèriault, P. Kucera, D. Gochis, C. Smith, R. Nitu, M. Hall, K. Ikeda, and E. Gutmann (2012). “How Well Are We Measuring Snow: The NOAA/FAA/N-CAR Winter Precipitation Test Bed.” In: *Bull. Amer. Meteor. Soc.* 93, pp. 811–829 (cit. on p. 123).
- Raymond, W. H. (1988). “High-order low-pass implicit tangent filters for use in finite area calculations.” In: *Mon. Wea. Rev.* 116, pp. 2132–2141 (cit. on p. 60).
- Reinhardt, T. and A. Seifert (2006). *A Three-Category Ice Scheme For LMK*. Tech. rep. COSMO Newsletter, pp. 115–121 (cit. on p. 64).
- Revelle, R. and H. E. Suess (1957). “Carbon Dioxide Exchange between Atmosphere and Ocean and the Question of an Increase of Atmospheric CO₂ During the Past Decades.” In: *Tellus* 9, 18–27 (cit. on p. 20).
- Rezacova, D., Z. Sokol, and P. Pesice (2007). “A radar-based verification of precipitation forecast for local convective storms.” In: *Atmos. Res.* 83.2-4, 211–224 (cit. on p. 76).
- Richards, L. A. (1931). “Capillary conduction of liquids through porous mediums.” In: *Physics* 1 (5), pp. 318–333 (cit. on p. 67).
- Richardson, L. F. (1922). *Weather Prediction by Numerical Process*. Cambridge University Press, Cambridge, UK (cit. on p. 25).
- Ritter, B. and J. F. Geleyn (1992). “A comprehensive radiation scheme for numerical weather prediction models with potential applications in climate simulations.” In: *Mon. Wea. Rev.* 120, pp. 303–325 (cit. on pp. 66, 95).
- Roberts, N. M. and H. W. Lean (2008). “Scale-selective verification of rainfall accumulations from high-resolution forecasts of convective events.” In: *Mon. Weather Rev.* 136.1, 78–97 (cit. on pp. 14, 49, 76, 116).
- Rockel, B., C. L. Castro, R. A. P. Sr., H. Von Storch, and G. Leoncini (2008a). “Dynamical Downscaling: Assessment of Model System Dependent Retained and Added Variability for Two Different Regional Climate Models.” In: *J. Geophys. Res.* 113 (cit. on p. 42).
- Rockel, B., A. Will, and A. Hense (2008b). “Special Issue on Regional Climate Modelling With COSMO-CLM (CCLM).” In: *Meteorol. Z.* 17 (4), pp. 477–485 (cit. on p. 92).

- Rogers, E., T. Black, B. Ferrier, Y. Lin, D. Parrish, and G. D. Mego (2001). *Changes to NCEP meso ETA analysis and forecast system: increase in resolution, new cloud microphysics, modified precipitation assimilation, modified 3DVAR analysis*. Tech. rep. NWS technical procedures bulletin. NOAA, USA (cit. on p. 95).
- Rojas, M. (2006). “Multiply nested regional climate simulation for Southern America: Sensitivity to model resolution.” In: *Mon. Wea. Rev.* 134, 2208–2223 (cit. on p. 38).
- Rojas, M. and A. Seth (2003). “Simulation and sensitivity in a nested modeling system for South America. Part II: GCM boundary forcing.” In: *J. Climate* 16, 2454–2471 (cit. on p. 38).
- Rummukainen, M. (2010). “State-of-the-art with regional climate models.” In: *WIREs Climate Change* 1, 82–96 (cit. on pp. 13, 38).
- Sasaki, H., H. Kida, V. Koide, and M. Chiba (1995). “The performance of long-term integrations of a limited area model with the spectral boundary coupling method.” In: *J. Meteorol. Soc. Japan* 73, 165–181 (cit. on p. 37).
- Schär, C., D. Lüthi, U. Beyerle, and E. Heise (1999). “The soil-precipitation feedback: A process study with a regional climate model.” In: *J. Climate* 12, pp. 722–741 (cit. on p. 50).
- Schär, C., D. Leuenberger, O. Fuhrer, D. Lüthi, and C. Girard (2002). “A new terrain-following vertical coordinate formulation for atmospheric prediction models.” In: *Mon. Wea. Rev.* 130, pp. 2459–2480 (cit. on p. 56).
- Schättler, U. (2012). *A Description of the Nonhydrostatic Regional COSMO-Model; Part V: Preprocessing: Initial and Boundary Data for the COSMO-Model*. Tech. rep. Deutscher Wetterdienst. URL: <http://www.cosmo-model.org/content/model/documentation/core/#p5> (cit. on pp. 67–71).
- Schmidt, F. (1977). “Variable fine mesh in spectral global model.” In: *Beitr. Phys. Atmos.* 50, 211–217 (cit. on p. 35).
- Schuiten, F. (May 2013). URL: http://www.maths.tcd.ie/~plynch/Publications/Woolly_art_figs/View_Figs.html (cit. on p. 26).
- Schwartz, C. S., J. S. Kain, J. S. Weiss, M. Xue, D. R. Bright, F. Kong, K. W. Thomas, J. J. Levit, and M. C. Coniglio (2009). “Next-Day Convection-Allowing WRF Model Guidance: A Second Look at 2-km versus 4-km Grid Spacing.” In: *Mon. Wea. Rev.* 137, pp. 3351–3372 (cit. on pp. 14, 49).
- Schwartz, S. E., R. J. Charlson, and H. Rodhe (2007). “Quantifying climate change – too rosy a picture?” In: *Nature Reports Climate Change*, (cit. on p. 33).
- Seneviratne, S. I., D. Luethi, M. Litschi, and C. Schär (2006). “Land-atmosphere coupling and climate change in Europe.” In: *Nature* 443, pp. 205–209 (cit. on pp. 39, 94).

- Serreze, M. C., M. P. Clark, R. L. Armstrong, D. A. McGinnis, and R. S. Pulwarty (1999). “Characteristics of the western United States snowpack from snowpack telemetry (SNOTEL) data.” In: *Water Resources Research*, 35.7, pp. 2145–2160 (cit. on p. 123).
- Serreze, M. C., M. P. Clark, R. L. Armstrong, D. A. McGinnis, and R. S. Pulwarty (2001). “Characteristics of large snowfall events in the mountain western United States as examined using snowpack telemetry (SNOTEL) data.” In: *Water Resources Research*, 37, pp. 675–688 (cit. on p. 15).
- Shakun, J. (May 2013). Harvard University. URL: <http://simpleclimate.wordpress.com/category/glaciers/> (cit. on p. 21).
- Shuman, F. G. (1989). “History of Numerical Weather Prediction at the National Meteorological Center.” In: *Wea. Forecasting* 4, 286–296 (cit. on p. 28).
- Skamarock, W. C. (2004). “Evaluating Mesoscale NWP Models Using Kinetic Energy Spectra.” In: *Mon. Wea. Rev.* 132 (12), pp. 3019–3032 (cit. on pp. 33, 125).
- Skamarock, W. C., J. B. Klemp, J. Dudhia, D. O. Gill, D. M. Barker, W. Wang, and J. G. Powers. (2005). *A Description of the Advanced Research WRF Version 2*. Tech. rep., 88 pp. (Cit. on p. 93).
- Skamarock, W. C., J. Klemp, J. Dudhia, D. Gill, D. Barker, W. Wang, and J. Powers (2008). *A Description of the Advanced Research WRF Version 3. NCAR Technical Note 475*. Tech. rep. NCAR Technical Note 475. 113 pp. (cit. on p. 121).
- Smiatek, G., B. Rockel, and U. Schättler (2008). “Time invariant data preprocessor for the climate version of the COSMO model (COSMO-CLM).” In: *Meteorol. Z.* 17, pp. 395–405 (cit. on p. 71).
- Solomon, S., D. Qin, M. Manning, Z. Chen, M. Marquis, K. B. Averyt, M. Tignor, and H. L. Millerq (2007). “Climate Change 2007: The Physical Science Basis. Contribution of Working Group I to the Fourth Assessment Report of the Intergovernmental Panel on Climate Change.” In: Cambridge University Press, Cambridge, United Kingdom and New York, NY, USA. Chap. Summary for Policymakers (cit. on p. 43).
- Staniforth, A. and H. Mitchell (1978). “A variable resolution finite element technique for regional forecasting with primitive equations.” In: *Mon. Weather Rev.* 106, 439–447 (cit. on p. 35).
- Stehr, N., H. V. Storch, and M. Flügel (1995). *Ice Ages and Astronomical Causes: Data, spectral analysis and mechanisms: Analogies for Present Debate?* Max-Planck-Institut für Meteorologie, 22 (cit. on p. 19).
- Stephens, G. L. (1978). “Radiation profiles in extended water clouds Part II: Parameterization schemes.” In: *J. Atmos. Sci.* 35, pp. 2123–2131 (cit. on p. 119).

- Steppeler, J., G. Doms, U. Schättler, H. W. Bitzer, A. Gassmann, U. Damrath, and G. Gregoric (2003). “Meso-gamma scale forecasts using the nonhydrostatic model LM.” In: *Meteor. Atmos. Phys.* 82, pp. 75–96 (cit. on p. 92).
- Suklitsch, M., A. Gobiet, A. Leuprecht, and C. Frei (2008). “High Resolution Sensitivity Studies with the Regional Climate Model CCLM in the Alpine Region.” In: *Meteorol Z.* 17 (4), pp. 467–476 (cit. on p. 83).
- Suklitsch, M., H. Truhetz, A. F. Prein, and A. Gobiet (2011). *NHCM-1: Non-hydrostatic climate modelling. Part II: Current state of selected cloud-resolving regional climate models and their error characteristics*. Tech. rep. Wegener Center Report 40 Wegener Center Verlag (cit. on p. 93).
- Taylor, K. E. (2001). “Summarizing multiple aspects of model performance in a single diagram.” In: *J. Geophys. Res.-Atmos.* 106.D7, 7183–7192 (cit. on p. 74).
- Tegen, I., P. Hollrig, M. Chin, I. Fung, D. Jacob, and J. Penner (1997). “Contribution of different aerosol species to the global aerosol extinction optical thickness: Estimates from model results.” In: *J. Geophys. Res.* 102, pp. 23895–23915 (cit. on p. 70).
- Theis, S. E., A. Hense, and U. Damrath (2005). “Probabilistic precipitation forecasts from a deterministic model: a pragmatic approach.” In: *Meteorol. Appl.* 12.3, 257–268 (cit. on p. 76).
- Thompson, G., P. R. Field, R. M. Rasmussen, and W. D. Hall (2008). “Explicit forecasts of winter precipitation using an improved bulk microphysics scheme. Part II: Implementation of a new snow parameterization.” In: *Mon. Wea. Rev.* 136, pp. 5095–5115 (cit. on p. 48).
- Tiedtke, M. (1989). “A comprehensive mass flux scheme for cumulus parameterization in large-scale models.” In: *Mon. Wea. Rev.* 117, pp. 1779–1799 (cit. on pp. 64, 95).
- Tyndall, J. (1872). *Contributions to Molecular Physics in the Domain of Radiant Heat*. Longmans, Green, and co. (cit. on p. 19).
- Vannitsem, S. and F. Chomé (2005). “One-way nested regional climate simulations and domain size.” In: *J. Climate* 18, 229–233 (cit. on p. 38).
- Venugopal, V., S. Basu, and E. Foufoula-Georgiou (2005). “A new metric for comparing precipitation patterns with an application to ensemble forecasts.” In: *J. Geophys. Res.-Atmos.* 110.D8 (cit. on p. 86).
- Von Storch, H. (2005). *Conceptual basis and applications of Regional Climate Modelling*. Barring L, Laprise R, eds. Extended Abstracts of a WMO/WCRP-sponsored Regional-Scale Climate Modelling Workshop High-resolution Climate Modelling: Assessment, Added Value and Applications. Lund, Sweden, 29 March—2 April 2004. Lund eRep Phys Geogr No. 5. (cit. on p. 40).

- Von Storch, H., H. Langenberg, and F. Feser (2000). “A spectral nudging technique for dynamical downscaling purposes.” In: *Mon. Wea. Rev.* 128, 3664–3673 (cit. on p. 37).
- Waldron, K. M., J. Paegle, and J. D. Horel (1996). “Sensitivity of a spectrally filtered and nudged limited-area model to outer model options.” In: *Mon. Wea. Rev.* 124, 529–547 (cit. on p. 37).
- Wang, Y. Q., L. R. Leung, J. L. McGregor, D. K. Lee, W. C. Wang, Y. H. Ding, and F. Kimura (2004). “Regional climate modeling: Progress, challenges, and prospects.” In: *J. Meteor. Soc. Japan* 82 (6), pp. 1599–1628 (cit. on p. 13).
- Warner, T. T. (2011). *Numerical Weather and Climate Prediction*. Cambridge University Press, New York, USA (cit. on pp. 25, 46, 53).
- Warner, T. T., R. A. Peterson, and R. E. Treadon (1997). “A tutorial on lateral conditions as a basic and potentially serious limitation to regional numerical weather prediction.” In: *Bull. Am. Meteor. Soc.* 78 (11), pp. 2599–2617 (cit. on p. 39).
- Washington, W. M. and C. C. L. Parkinson (2005). *An Intro to 3-Dimensional Climate Modeling*. Vol. 2. University Science Books, USA, p. 355 (cit. on p. 53).
- Weart, S. (2003). *The Discovery of Global Warming*. San Diego, California, USA: Center for History of Physics, American Institute of Physics (cit. on pp. 17–19).
- Weaver, J. F., E. Grunfest, and G. M. Levy (2000). “Two Floods in Fort Collins, Colorado: Learning from a Natural Disaster.” In: *Bull. Amer. Meteor. Soc.* 81, pp. 2359–2366 (cit. on p. 15).
- Wedi, N. P. and S. Malardel (2010). *Non-hydrostatic modelling at ECMWF*. Tech. rep. ECMWF Newsletter, pp. 17–21 (cit. on pp. 47, 48).
- Wegener, A. (1929). *Die Entstehung der Kontinente und Ozeane*. Ed. by W. Westphal. Braunschweig Druck und Verlag von Friedr. Vieweg & Sohn Akt.-Ges. (cit. on p. 18).
- Weisman, M. L., W. C. Skamarock, and J. B. Klemp (1997). “The Resolution Dependence of Explicitly Modeled Convective Systems.” In: *Mon. Wea. Rev.* 125.4, pp. 527–548 (cit. on pp. 14, 45, 63, 122).
- Wernli, H. and M. Sprenger (2007). “Identification and ERA-15 climatology of potential vorticity streamers and cutoffs near the extratropical tropopause.” In: *J. Atmos. Sci.* 64.5, 1569–1586 (cit. on p. 84).
- Wernli, H., M. Paulat, M. Hagen, and C. Frei (2008). “SAL-A Novel Quality Measure for the Verification of Quantitative Precipitation Forecasts.” In: *Mon. Weather Rev.* 136.11, 4470–4487 (cit. on pp. 75, 83, 84, 117).

- Weusthoff, T., F. Ament, M. Arpagaus, and M. W. Rotach (2010). “Assessing the Benefits of Convection-Permitting Models by Neighborhood Verification: Examples from MAP D-PHASE.” In: *Mon. Wea. Rev.* 138, pp. 3418–3433 (cit. on pp. 14, 49, 116).
- Wicker, L. and W. C. Skamarock (2002). “Time-splitting methods for elastic models using forward time schemes.” In: *Mon. Wea. Rev.* 130, pp. 2088–2097 (cit. on pp. 58, 95).
- Wiin-Nielsen, A. (1991). “The Birth of Numerical Weather Prediction.” In: *Tellus* 43AB (4), 36–52 (cit. on p. 28).
- Wilks, D. S. (Dec. 2005). *Statistical Methods in the Atmospheric Sciences*. 2nd ed. Academic Press. ISBN: 0127519661 (cit. on p. 78).
- Willet, H. C. (1951). *The Forecast Problem*. Ed. by T. F. Malone. American Meteorological Society (cit. on p. 28).
- Winterfeldt, J. and R. Weisse (2009). “Assessment of value added for surface marine wind speed obtained from two Regional Climate Models (RCM).” In: *Mon. Wea. Rev.* 137 (9), 2955–2965 (cit. on pp. 37, 42).
- Yang, D., B. E. Goodison, J. R. Metcalfe, V. S. Golubev, R. Bates, T. Pangburn, and C. L. Hanson (1998). “Accuracy of NWS 8" Standard Nonrecording Precipitation Gauge: Results and Application of WMO Intercomparison.” In: *J Atmos Sol-Terr Phy* 15, 54–68 (cit. on p. 123).
- Yang, G.-Y. and J. Slingo (2001). “The diurnal cycle in the tropics.” In: *Month. Wea. Rev.* 129, pp. 784–801 (cit. on p. 45).
- Zepeda-Arce, J., E. Foufoula-Georgiou, and K. K. Droegemeier (Apr. 2000). “Space-time rainfall organization and its role in validating quantitative precipitation forecasts.” In: *J. Geophys. Res.-Atmos.* 105.D8, 10129–10146 (cit. on pp. 14, 49, 76, 78, 81).
- Zinner, T., H. Mannstein, and A. Tafferfer (2008). “Cb-TRAM: Tracking and monitoring severe convection from onset over rapid development to mature phase using multi-channel Meteosat-8 SEVIRI data.” In: *Meteorol. Atmos. Phys.* 101.3–4, 191–210 (cit. on p. 87).

Abstract:

Convection permitting climate simulations (CPCSs) are able to omit error prone deep convection parameterizations by resolving deep convection explicitly. Furthermore, they are resolving orography and surface fields more accurately which is an advantage especially in mountainous or coastal regions compared to traditional climate simulation with parameterized deep convection. In this thesis it is investigated if these advantages lead to added value in CPCSs compared to coarser gridded simulations.

The main improvements of CPCSs are found in the representation of precipitation. Especially sub-daily scales and spatial patterns smaller than approximately 100 km are improved. At large (e.g., meso- α ; 200 km to 2000 km) scales, precipitation patterns of CPCSs tend to converge towards the patterns of coarser gridded simulations. However, two exceptions are found: (1) improved large-scale average heavy precipitation totals in summer in the Colorado Headwaters, and (2) more accurate spatial patterns of two meter temperature which is strongly related to the improved orography in mountainous regions.

The key added value which can be consistently found in an ensemble of CPCSs are: (1) improved timing of the summer convective precipitation diurnal cycle in mountainous regions, (2) more accurate intensities of most extreme precipitation, (3) more realistic size and shape of precipitation objects, and (4) better spatial distribution of precipitation patterns. These improvements are not caused by the higher resolved orography but by the explicit treatment of deep convection and the more realistic model dynamics. In contrast, improvements in summer temperature fields can be fully attributed to the higher resolved orography.

Zum Inhalt:

Konvektionsauflösende Klimasimulationen (CPCSs) ermöglichen eine explizite Simulation der atmosphärischen Tiefenkonvektion wodurch fehleranfällige Parametrisierungen vermieden werden können. Desweiteren wird im Vergleich zu gewöhnlichen Klimasimulationen die Orographie und Landoberfläche detaillierter dargestellt was vor allem in Berg- und Küstenregionen vorteilhaft ist.

In dieser Arbeit wird der Mehrwert von CPCSs im Vergleich zu gröber aufgelösten Simulationen untersucht. Der größte Mehrwert findet sich in der Simulation des Niederschlages. Besonders Prozesse auf der Subtagesskala und räumliche Muster, die kleiner als ungefähr 100 km sind, werden verbessert. Auf größeren Skalen (z.B. der meso- α Skala) konvergieren Niederschlagsmuster von CPCSs mit jenen von grobskaligeren Simulationen. Allerdings werden zwei Ausnahmen gezeigt: (1) verbesserte sommerliche Starkniederschlagsmengen im Quellgebiet des Colorado Flusses und (2) realitätsnähere räumliche Muster der bodennahen Lufttemperatur, die stark mit der verbesserten Orographie zusammenhängen.

Ein Mehrwert, der konsistent in einem Ensemble von CPCSs auftritt, wurde in folgenden Bereichen gefunden: (1) verbesserte zeitliche Abläufe des Tagesgangs von konvektiven Niederschlägen im Sommer, (2) verbesserte Intensitäten von Extremniederschlägen, (3) realistischere Größen und Formen von Niederschlagsobjekten und (4) verbesserte räumliche Niederschlagsmuster. Diese Verbesserungen sind nicht durch die höher aufgelöste Orographie bedingt, sondern durch die explizite Auflösung der Tiefenkonvektion und der realistischeren Modelldynamik. Im Gegensatz dazu können Verbesserungen der bodennahen Temperatur im Sommer der höher aufgelösten Orographie zugeschrieben werden.